

*Donahue*

AFCRL-72-0376

THE MEASUREMENT OF SPATIAL AND TEMPORAL DISTRIBUTION  
OF RADIATION, USING A TALBOT SPECTROMETER

by

Adolf W. Lohmann

Donald E. Silva

Department of Applied Physics and Information Science

University of California, San Diego

La Jolla, California 92037

Contract No. F19628-69-C-0268

Project No. 8692

FINAL REPORT

1 July 1971 - 30 June 1972

30 June 1972

DTIC QUALITY INSPECTED 2

Contract Monitor: Thomas P. Condron

Optical Physics Laboratory

Approved for public release; distribution unlimited.

Supported by

Defense Advanced Research Projects Agency

ARPA Order No. 1366

Monitored by

AIR FORCE CAMBRIDGE RESEARCH LABORATORIES

AIR FORCE SYSTEMS COMMAND

UNITED STATES AIR FORCE

BEDFORD, MASSACHUSETTS 01730

16y  
WCRC-74 19/65

DISTRIBUTION STATEMENT A

Approved for public release  
Distribution Unlimited

ARPA Order No. 1366

Contract No. F19628-69-C-0268

Program Code No. 1E50

Principal Investigator and Phone No.  
Prof. Adolf W. Lohmann/  
714 453-2000 ext. 2747

University of California, San Diego

AFCRL Project Scientist and Phone No.  
Thomas P. Condron/617 861-4852

Effective Date of Contract -  
29 May 1969

Contract Expiration Date -  
29 May 1972

Qualified requestors may obtain additional copies from  
the Defense Documentation Center. All others should  
apply to the National Technical Information Service.

THE MEASUREMENT OF SPATIAL AND TEMPORAL DISTRIBUTION  
OF RADIATION, USING A TALBOT SPECTROMETER

by

Adolf W. Lohmann

Donald E. Silva

Department of Applied Physics and Information Science  
University of California, San Diego  
La Jolla, California 92037

Contract No. F19628-69-C-0268

Project No. 8692

FINAL REPORT

1 July 1971 - 30 June 1972

30 June 1972

Contract Monitor: Thomas P. Condron  
Optical Physics Laboratory

Approved for public release; distribution unlimited.

Supported by  
Defense Advanced Research Projects Agency  
ARPA Order No. 1366

Monitored by

AIR FORCE CAMBRIDGE RESEARCH LABORATORIES  
AIR FORCE SYSTEMS COMMAND  
UNITED STATES AIR FORCE  
BEDFORD, MASSACHUSETTS 01730

## ABSTRACT

Our goal was to measure the distribution of radiation  $S$  as a function of its angular coordinates  $\alpha$ ,  $\beta$  and its wavelength  $\lambda$ . We first measured  $S(\alpha)$ , i.e. the distribution of radiation as a function of one angular coordinate. From this we learned how critical the various parameters of our instrument, such as collimation and the gratings' substrate flatness, were to its successful operation. These investigations led to the design of new interferometric test instruments which include an autocollimator, and a lateral and radial shearing interferometer. Finally a theoretical study of an instrument to measure  $S(\alpha, \beta, \lambda)$  was accomplished.



## TABLE OF CONTENTS

	Foreword . . . . .	vi
I.	Introduction . . . . .	1
	References for Chapter I . . . . .	6
II.	Review of the Talbot Effect . . . . .	7
	Introduction . . . . .	7
	Theory . . . . .	7
	References for Chapter II . . . . .	10
III.	The Talbot Shearing Interferometer . . . . .	11
	Introduction . . . . .	11
	A Qualitative Ray Explanation . . . . .	13
	The Lateral Shearing Interferometer . . . . .	16
	Discussion . . . . .	16
	Theory . . . . .	16
	Tilted Ronchi Rulings . . . . .	19
	Filtering . . . . .	22
	a. Zero Order Filtering . . . . .	23
	b. First Order Filtering . . . . .	25
	Experiments . . . . .	26
	Constant Radial Shearing Interferometer . . . . .	30

Discussion . . . . .	30
Definition of a Circular Grating . . . . .	31
A Qualitative Explanation of Self- Imaging with Circular Gratings . . . . .	31
Theory . . . . .	34
a. General . . . . .	34
b. Analysis . . . . .	38
Shifted Circular Gratings . . . . .	47
Filtering . . . . .	50
a. Zeroth-Order Filtering . . . . .	50
b. First-Order Filtering . . . . .	53
Experiments . . . . .	55
a. No Filtering . . . . .	56
b. Shifted Gratings . . . . .	56
c. Filtering . . . . .	57
References for Chapter III . . . . .	61
IV. The Talbot Spectrometric Imager . . . . .	62
Introduction . . . . .	62
Theory . . . . .	65
Point Spread Response . . . . .	67
Demodulation of the Response . . . . .	69
The Talbot Spectrometer Review . . . . .	69
The Talbot Fourier Analyzer . . . . .	71
The Talbot Image Scanner . . . . .	72
Theory . . . . .	72
Special Cases . . . . .	75
The Talbot Spectrometric Imager . . . . .	77

	References for Chapter IV . . . . .	79
V.	Conclusions . . . . .	80
	Summary of Results . . . . .	80
	Suggestions for Further Study . . . . .	82
	References for Chapter V . . . . .	84
	Paper 1 . . . . .	85
	References . . . . .	87
	Paper 2 . . . . .	88
	References . . . . .	90
	Paper 3 . . . . .	90
	References . . . . .	92
	Appendix 1, Source Size . . . . .	93
	Appendix 2, Approximations Leading to the Second Derivative . . . . .	94
	Appendix 3, Theoretical Considerations for First Order Filtering . . . . .	96
	Appendix 4, Tolerances for Spatial Filtering a Test Object with Multiple Focal Lengths . . . . .	97
	Document Control Data - R & D . . . . .	101

## FOREWARD

In 1836 H. F. Talbot discovered that images of a grating illuminated with a point source of light were formed without the aid of any optical devices. Although theoretical studies have been made of this phenomenon and of the intermediate images that are formed ("Fresnel images") it has not been fully exploited for the design of high-quality, low-cost optical instruments. This report is concerned with the proper modifications of this effect. Two new shearing interferometers, an autocollimator, a Fourier analyzer and a spectrometric imager using this effect are developed in this report.

Following an introduction and a brief review of the pertinent details of the Talbot phenomenon theory, the Talbot shearing interferometers are discussed. The theory and experimental evidence are presented. Multiple-shearing interferences are obtained that can be reduced to triple-shearing or double-shearing interferences by the addition of simple spatial filtering. When the shear is less than the width of the details in the object, these interferences become either the second or first derivative of the object under test, respectively. Either lateral or constant radial shear can be introduced by choosing Ronchi rulings or circular gratings. Thus both lateral and radial derivatives are easily obtained. If white light is used as a source, color fringes or high contrast are observed.

The spectrometric imager follows and is an instrument that encodes the brightness distribution of a scene  $S$  as a function of wavelength and angular position coordinates  $(\alpha, \beta)$  by a single detector which responds to the light intensity as two gratings are displaced. The situation for

encoding only the wavelength information  $S(\lambda)$  conceived by Lohmann with spectra by Klages is briefly reviewed. A Fourier analyzer is discussed. The function to be analyzed is cut out of an opaque material and is incoherently and uniformly illuminated. The detected signal is its cosine transformation as a function of grating separation. This is followed by the theory for an instrument that encodes only  $S(\alpha, \beta)$ . The encoding for a restricted region of  $(\alpha, \beta)$  is a cosine transformation, and therefore another cosine transformation recovers the information. Since only one point in the two dimensional Fourier cosine transformation space can be encoded at any given time, the Fourier space must be sampled. Three different scanning systems are explored. Limitations of our instrument in encoding  $S(\alpha, \beta, \lambda)$  are discussed. The additional modification required to encode this most general situation and the attendant loss of light energy at the detector are also discussed.

A separate chapter concludes the body of the report by summarizing the work and offering remarks for future projects. Three papers are included in the report. Two of them are our early results on the shearing interferometers and contain interferograms of good quality. The third paper is about an autocollimator which is a special case of the Talbot interferometer. Here both grating rulings are aligned in the same direction, and moiré fringes are observed in the image plane whenever the two grating periods are unequal. These fringes indicate that a spherical wave is at the first grating. By adjusting the collimating lens, this spherical wave can be made plane through observing the moiré fringes at the second grating. A uniformly bright (or dark) field indicates that the system is aligned within the accuracy limitations of the interferometer.

## CHAPTER I

### INTRODUCTION

A rather remarkable optical phenomenon was reported by H. F. Talbot<sup>1</sup> over one hundred and thirty years ago. It is the goal of this report to use this effect for several new metrological purposes.

Briefly stated, this phenomenon that we call the "Talbot effect" concerns the formation of images when a certain class of structures like a grating are illuminated by spatially coherent light. In other words, the Talbot effect is a method for forming images of these structures without any lenses or mirrors, simply by illuminating them with spatially coherent light. The first object was a grating of equidistant lines, and subsequent research has enlarged the class of objects to include a number of periodic structures<sup>2</sup>. Montgomery<sup>3</sup> determined the total class of objects, and showed that the two dimensional Fourier transform of these self-imaging objects could exist only on a set of concentric circles. The self-images repeat themselves at intervals deduced by Lord Rayleigh<sup>4</sup> as  $2d^2/\lambda$  (where  $d$  is the grating period,  $\lambda$  is the wavelength of the light) for plane wave illumination. Therefore, longer wavelength illumination produces closer spaced self-images than shorter wavelengths. Therefore, when white light is used as a source, color images of high contrast are observed.

The wavelength dependency of the intervals between self-images was used to develop a spectrometer by A. Lohmann<sup>5</sup>. The recorded interferogram is a cosine transformation of the spectrum and is the first grating spectrometer that records all wavelengths in the spectrum

simultaneously<sup>6</sup>. The Talbot effect has been employed in connection with masks for integrated circuits that contain hundreds of identical shapes in a periodic array<sup>7</sup>. When a section of the mask is damaged through mishandling or wear, the original pattern can be reconstructed by illuminating the damaged mask with a plane monochromatic wave. In a distant self-image plane the restored image appears. Thus far only simple geometries have been successfully tested. The high contrast color self-images can be used artistically. By placing a second grating in the field and slightly tilting it, moire fringes are formed between the self-images and the grating. The location of the grating selects the color combination. A third grating adds more fringe patterns and additional colors. A similar setup was used by E. Lau in the design of table cloths<sup>8</sup>.

The useful aspects of the Talbot effect in the design of new instruments follow. Poor quality gratings can be used because the self-images emphasize the periodic structure of the grating, and therefore local defects in it are minimized. Furthermore the location of the self-images are at intervals that are a function of the grating period, and misalignment of the grating reduces the effective grating period by a cosine factor. In addition the self-images occur over distances that are easily managed by the experimenter. The self-image interval for  $d = 0.1\text{mm}$  and  $\lambda = 2/3 \times 10^{-3}\text{mm}$  is 30 mm. Consequently positioning of components can be done without the aid of micropositioners.

Although some work has been done using the Talbot effect, it has not been fully exploited in the design of rugged, high quality, low cost instruments. This report is concerned with the proper modification

of this effect in the design of such instruments. Two new shearing interferometers, an autocollimator, a Fourier analyzer, an image scanner and a spectrometric imager are developed. These instruments are discussed within these pages. Each chapter has appropriate introductory remarks. Chapter II is a review of the Talbot effect. Only relevant aspects of the theory are covered. Both the lateral and constant radial shearing interferometers are discussed in Chapter III. Ronchi rulings give a lateral shear, and circular gratings produce a constant radial shear. Therefore either one dimensional or axially symmetric optical systems can be tested. With simple spatial filters either double or triple shearing interferences are obtained that become the first or second derivative respectively when the shear is less than the width of the tiniest details in the test object. The theory with experimental evidence is presented. In Paper 1 and Paper 2 are reprints of our preliminary work with these interferometers and contain interferograms of high quality. Chapter IV contains theoretical studies of the Fourier analyzer, the image scanner and the spectrometric imager. The brightness distribution  $S$  as a function of its angular coordinates  $\alpha, \beta$  and its wavelength  $\lambda$  is encoded onto a single detector by the spectrometric imager. The image scanner encodes only  $S(\alpha, \beta)$ , and the Fourier analyzer is a special case of the image scanner. Chapter V concerns our conclusions about these instruments and remarks about future work. The autocollimator is covered in Paper 3.

These instruments based on the Talbot effect have a lot in common and yet differ in ways that allow special measurements to be made. All of the instruments use two gratings,  $G_1$  and  $G_2$ , where self-images of



the first grating are detected by a second. But they differ in the way that the optical light signal is processed. Both the shearing interferometers and autocollimator use an area detector like the eye or photographic film, and their gratings are kept at a fixed distance, whereas the remaining instruments use a combination of grating motions to modulate the light intensity onto a single detector. The motions used are moving G2 laterally and longitudinally and rotating both gratings in unison. The latter motion is required when two dimensional spatial information is desired. The lateral motion makes it possible to select either one of two terms in the point spread response that contains the wavelength or spatial information. A compilation of the physical aspects of our Talbot instruments follow with a summary in Table I. The spectrometer is added to complete the list, and diagrams of the instruments can be found in the appropriate chapters.

Shearing interferometer: Collimated light impinges upon G1 to form the self-images. A second grating is situated in one of the self-image planes. Placing a test object between the two gratings distorts the self-images at G2. The moiré fringes formed by the distorted self-images and G2 are observed by an area detector.

Autocollimator: This instrument is identical to the above; the test object is the curvature of the wavefront at G1 caused by defocusing the collimator lens. The moiré fringes measure the wavefront curvature which is related to the amount of defocusing.

Spectrometer: The source to be measured is collimated and self-images of G1 are formed. G2 moves laterally and the instrument's response is filtered for the  $(\alpha \pm \lambda/d)$  dependent term with  $\alpha = 0$ . The

light is collected onto a single detector which records the light intensity as G2 is moved longitudinally.

Fourier Analyzer: A function mask is cut out of opaque material, incoherently illuminated and placed in the front focal plane of the collimating lens. G2 is moved laterally so that the  $\alpha$ -dependent term of the response is selected. The light is collected onto a single detector, and the intensity is recorded as G2 moves longitudinally.

Image scanner: The source to be measured is collimated and waves emitted from the collimator impinge upon G1. G2 is moved laterally so that the  $\alpha$ -dependent term can be selected from the point spread response. The light is collected, and the intensity is recorded as a function of the grating separation. In addition both gratings are rotated so that the two dimensional scene can be scanned.

Spectrometric imager: This instrument has the same setup as the image scanner except that the  $(\alpha \pm \lambda/d)$  term is selected.

The foregoing has been summarized in Table I. The terms  $x(t)$ ,  $z(t)$  and  $\phi(t)$  refer to the grating motions: G2 lateral, G2 longitudinal and both gratings rotational. The  $\alpha$  and  $(\alpha \pm \lambda/d)$  columns stand for the selected term of the point spread response. The type of detector used is indicated by the area and single columns.

TABLE I. A Comparison of the Talbot Instruments

Instruments	area	single	x(t)	z(t)	$\phi(t)$	$\alpha$	$\alpha \pm \lambda/d$
Autocollimator	xx	--	--	--	--	--	--
Shearing Interferometer	xx	--	--	--	--	--	--
Spectrometer	--	xx	xx	xx	--	--	xx
Fourier Analyzer	--	xx	xx	xx	--	xx	--
Image Scanner	--	xx	xx	xx	xx	xx	--
Spectrometric Imager	--	xx	xx	xx	xx	--	xx

xx marks the features found in the instrument.

#### References for Chapter I

1. H. F. Talbot, Phil. Mag. 9, 401 (1836).
2. J. Cowley and A. Moodie, Proc. Phys Soc. (London) B70, 486, 497, 505 (1957); B76, 378 (1960).
3. W. D. Montgomery, J. Opt. Soc. Amer. 57, 772 (1967).
4. Lord Rayleigh, Phil. Mag. 11, 196 (1881).
5. A. Lohmann, Proc. ICO Conf. Opt. Instr., ed K. J. Habbell (London, 1961) p. 58.
6. P. Felgett, J. De Phys. Colloq C2, 169 (1967).
7. H. Dammann, G. Groh and M. Kock, Appl. Opt. 10, 1454 (1971).
8. E. Lau, Wiss. Ann. 1, 43 (1952).

## CHAPTER II

### REVIEW OF THE TALBOT EFFECT

#### INTRODUCTION

In 1836 H. F. Talbot, observing with a powerful lens the region behind a grating placed ten to twenty feet from a radiant point of intense solar light, discovered a series of images of the grating. In other words, the diffracted light formed images of the grating without the use of any optical components. We call these images "Talbot images," which are also known in the literature as "self images" and "Fourier images."<sup>2,3,4</sup>

Lord Rayleigh,<sup>5</sup> in 1881, deduced that for a grating of period  $d$ , illuminated by a monochromatic plane wave of wavelength  $\lambda$ , a series of Talbot images are formed at intervals given by  $z_T = \lambda / (1 - \sqrt{1 - \lambda^2/d^2}) \approx 2d^2/\lambda$  when  $\lambda/d \ll 1$ . Recently, a theoretical treatment with experimental evidence of Talbot images for structures other than a linear grating was reported by Cowley and Moodie.<sup>2</sup> The existence of many other images which occur in the region of Fresnel diffraction was also discussed. These "Fresnel images" have been theoretically explained by Winthrop and Worthington.<sup>3</sup> The complete set of objects that self-image in a plane when illuminated by a plane monochromatic wave was derived by Montgomery.<sup>4</sup> Only those aspects of the theory that are required to understand this dissertation will be presented in the following section.

#### Theory

Let a monochromatic plane wave be incident upon a grating as shown in figure 1. We chose the mathematically simple grating transmission function  $g(x) = 1 + \cos(2\pi x/d)$ , so that the relevant parts of the theory

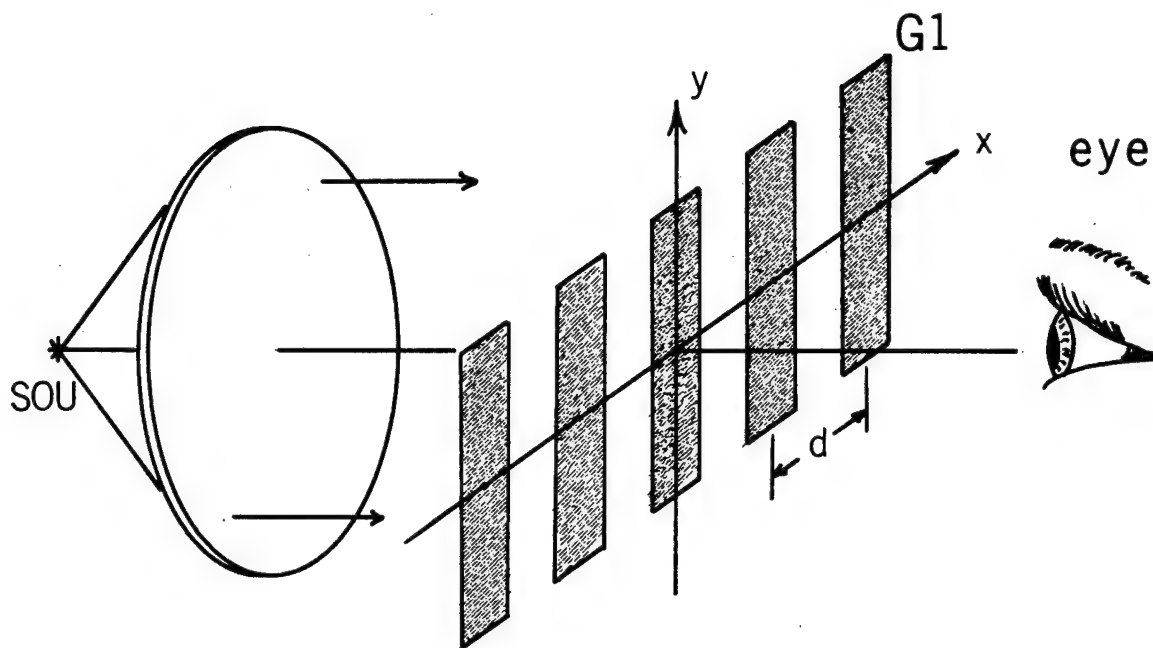


Figure 1. A grating illuminated with a plane wave. The observer sees the "Talbot image".

will be enhanced. The complex wavefield just behind the grating is given by the product of the grating transmission function and the wavefield just prior to the grating. The complex wavefield behind the grating can be described by the Raleigh-Sommerfield-Debye formulation for diffraction of plane waves. We have

$$u(x, y, z) = \iint \tilde{u}(v, \mu; 0^+) \exp \left\{ 2\pi i \left[ \frac{z}{\lambda} \sqrt{1 - \lambda^2 (v^2 + \mu^2)} + vx + \mu y \right] \right\} dv d\mu$$

where

$$\tilde{u}(v, \mu; 0^+) = \iint u(x, y, 0^+) \exp \{-2\pi i (vx + \mu y)\} dx dy,$$

and the integrations are over the interval  $(-\infty, +\infty)$  in this chapter.

Performing the Fourier integration yields

$$\tilde{u}(v, \mu; 0^+) = \delta(v, \mu) + 1/2 \delta(v - 1/2, \mu) + 1/2 \delta(v + 1/2, \mu),$$

and placing this into our diffraction formula yields

$$u(x, y, z) = \exp\{ikz\} + \cos(2\pi x/d) \exp\{ikz \sqrt{1 - \lambda^2/d^2}\} \quad (1)$$

This equation can be interpreted as the sum of two interfering waves traveling in the +z direction. The first wave is an ordinary plane wave with wavelength  $\lambda$  and phase velocity  $c$ , and the latter wave has a wavelength  $\lambda_m = \lambda/\sqrt{1-\lambda^2/d^2}$  and phase velocity  $v_m = c/\sqrt{1-\lambda^2/d^2}$ . We can understand the Talbot effect as the interference between an ordinary plane wave and a modulated plane wave. Since their phase velocities are different, they must travel a distance  $z_T$  before they are again in phase.

We can rewrite equation (1) in a way that will best illustrate this explanation:

$$u(x,y,z) = \exp\{ikz\} [1 + \cos(2\pi x/d) \exp\{ikz(1 - \sqrt{1-\lambda^2/d^2})\}]$$

The overall phase factor  $\exp\{ikz\}$  can be eliminated from further consideration since the final observed quantity is intensity. Images of the grating will occur whenever the exponential factor of the modulated wave is 1; and this occurs at multiples of the distance

$$z_T = \lambda/(1 - \sqrt{1-\lambda^2/d^2}) \approx 2d^2/\lambda \text{ for } \lambda/d \ll 1.$$

A typical example for  $z_T$  is:  $d = 0.1 \text{ mm}$ ,  $\lambda = 2/3 \times 10^{-3} \text{ mm}$ ;  $z_T = 30 \text{ mm}$ .

Since the distance for Talbot imaging is  $\lambda$  dependent, this effect can be used to make a spectrometer.<sup>6,7</sup>

In practice gratings are of limited size, and the diffracted orders "walk-off" the zeroth order as shown in figure 2. The Talbot effect occurs within the region where the diffracted orders interfere. These waves overlap in the shaded region of figure 2, which forms a wedge whose width decreases to zero at  $z_{MAX} = Bd/2\lambda$ , where  $B$  is the grating width, and  $z_{MAX}$  is the maximum distance from the grating over which the Talbot effect occurs.

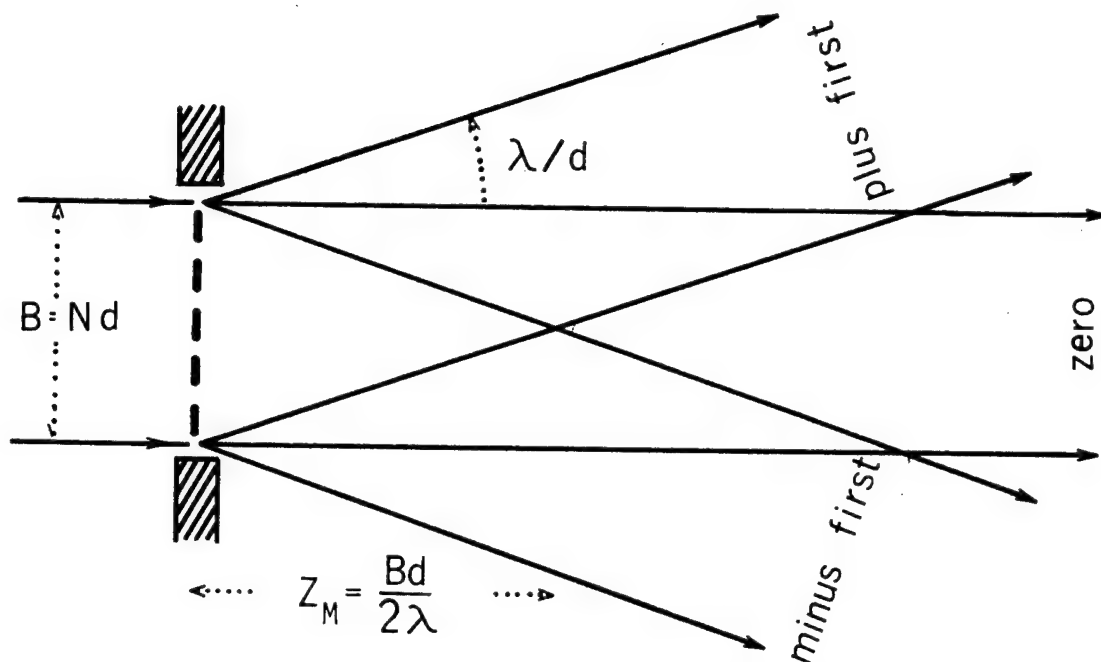


Figure 2. The first diffracted orders "walkoff" the zeroth order with increasing  $z$ . The maximum distance for the Talbot effect is marked  $z_M$ .

#### References for Chapter II

1. H. F. Talbot, *Phil. Mag.* 9, 401 (1836).
2. J. Cowley and A. Moodie, *Proc. Phys. Sec.* B70, 486 (1957).
3. J. Winthrop and C. Worthington, *J. Opt. Soc. Amer.* 55, 373, (1965).
4. W. D. Montgomery, *J. Opt. Soc. Amer.* 57, 772 (1967).
5. Lord Rayleigh, *Phil Mag.* 11, 196 (1881).
6. A. Lohmann, *Proc. Conf. Opt. Instruments and Techniques*, 1961 London, Chapman and Hall, 1962, p. 58.
7. H. Klages, *J. De Phys. Colloq.* C2, 2 (1967).

# CHAPTER III

## THE TALBOT SHEARING INTERFEROMETERS

### INTRODUCTION

Shearing interferometry has been used to test optical instruments and components, to study physico-chemical phenomena in liquids, and to evaluate optical transfer functions, i.e. the contrast of an image plotted against its spatial frequency.<sup>1</sup> In this type of interferometry the wavefront under test is duplicated and displaced. They are then made to interfere with each other, yielding a comparison of the wavefront with a sheared image of itself. These interferometers typically use a single beam-dividing element that affords a simplicity over other interferometers. There are two ways of observing the sheared wavefronts. The first method is to have the shear sufficiently large that each of the wavefronts interferes with the uniform background of the other. This is called "total shear" and the fringes observed are lines of equal optical paths. In the second method the shear is kept smaller than the width of the details that we wish to observe, and the fringes are proportional to the gradient of the wavefront in the direction of the shear. This method is known as "differential shear." The earliest shearing interferometer introduced a lateral displacement between the waves,<sup>2</sup> and the most recent class of shearing interferometers cause a constant radial shift between the wavefronts.<sup>3</sup> In the former case we obtain the lateral gradient of the wavefront, and in the latter the radial gradient is observed. It is desirable to have both types of interferometers since geometries that require testing are often either one-dimensional or circular.



Recently, a new shearing interferometer based on the Talbot effect was introduced.<sup>4</sup> The basic setup is shown in fig. 4. An image of the grating is formed at multiples of a distance  $z_T = 2d^2/\lambda$  (where  $d$  is the grating period) behind the grating that has been illuminated by a plane monochromatic wave. The space between the two gratings is empty. In other words, the Talbot effect is a method of forming images of a periodic object without any lenses or mirrors. When properly modified, the Talbot effect affords a unique method for quantitatively observing phase objects through the use of two gratings, one of which is self-imaged onto the second. Since the grating shears the wavefront in a direction perpendicular to its rulings, a Ronchi ruling laterally shears the wavefront and a circular grating gives a constant radial shear to the wavefront. Therefore, by a suitable choice of gratings, optical instruments with either one-dimensional or circular geometries can be tested simply.

In this paper the complete theory and experimental evidence for both types of shearing interferometers will be presented. A complete theory requires scalar diffraction theory to explain the self-imaging effect, the spatial filtering capability, and the high-contrast color fringes that are observed when white light is used as a source. However, a ray explanation like that of Nishijima and Oster<sup>5</sup> will be presented first to acquaint the reader with the operation of this instrument. The ray explanation is valid only for distances from the first grating that are about one-eighth of the Talbot distance  $z_T$ , which greatly limits the sensitivity by orders of magnitude.<sup>6</sup> Thus the ray explanation will be followed by the wave theory in order to understand the full capabilities of this instrument.

### A Qualitative Ray Explanation

A Ronchi ruling is illuminated with collimated light as shown in Figure 3. The diffracted waves are modulated and form "Fresnel Images." At integer multiples of the distance  $z_T \approx 2d^2/\lambda$ , where  $d$  is the grating period, an image of the Ronchi ruling is formed. If a second grating is placed at one of these image planes in anti-position to the image, no light will be transmitted beyond the second grating. Hence a ray that passes through a slit of the first grating is blocked by the second grating as shown in Figure 3. A prism of wedge angle  $\alpha$  is introduced at a distance  $z$  from the second grating and normal to the incident rays. The rays passing through the prism will be bent through an angle  $\epsilon$ . Thus the intensity of the light as seen by the observer varies with the angle  $\epsilon$ , with peak intensities given by  $\epsilon_m \approx \tan \epsilon_m = (m + 1/2) d/z$ , and dark fringes by  $\epsilon_m \approx \tan \epsilon_m = md/z$ . The angle  $\epsilon$  is related to the wedge angle  $\alpha$  under small angle approximation by  $\epsilon = (n - 1)\alpha$ . The wedge angle  $\alpha$  is for small angles determined by the ratio  $\alpha \approx \tan \alpha = \Delta t/\Delta x$ , where  $\Delta t$  = prism thickness,  $\Delta x$  = distance from apex. A phase object can be thought to be made up of prisms, a fact which is often used to explain the action of a lens, so that for any point  $(x,y)$  on the object, the prism angle  $\alpha$  is given by  $\alpha(x,y) \approx \partial t(x,y)/\partial x$ , which in turn is related to  $\epsilon$  by  $\epsilon(x,y) = (n-1) \partial t(x,y)/\partial x$ . The derivative  $\partial t(x,y)/\partial y$  is of no concern here since the grating bars are parallel to the  $y$ -axis.

Thus a dark fringe structure is obtained whenever  $\epsilon(x,y)$  meets the dark fringe conditions. These fringes indicate lines of equal  $\partial t/\partial x$ , which is the  $x$ -component of the surface gradient at point  $(x,y)$ . Where the lines are close together, the slope  $\partial t/\partial x$  changes rapidly. Hence

the fringe density or fringe frequency is proportional to the x-component of the curvature  $\partial^2 t / \partial x^2$ . The maximum detectable curvature is determined by the minimum detectable fringe separation. In a sense what is observed is the second derivative of the phase object.

There are two problems of fringe detection. The first occurs when the fringes become too fine for the eye to resolve them. This is only a practical limitation and a magnifying glass would extend the sensitivity. But the second problem is more fundamental. The field of view is finite, say  $B = Nd$ , where  $N$  is the number of lines in the grating. For an object whose curvature is at the minimum detectable sensitivity, its curvature must be large enough for at least one full (or maybe one-half) fringe across the field. Hence  $[(\partial t / \partial x)_{\max} - (\partial t / \partial x)_{\min}] (n-1) \geq d/2z$ . If  $(\partial t / \partial x)_{\max}$  is at  $x = +Nd/2$  and  $(\partial t / \partial x)_{\min}$  is at  $x = -Nd/2$ , then

$$\partial t(x+Nd/2, y) / \partial x - \partial t(x-Nd/2, y) / \partial x \approx \partial^2 t / \partial x^2 Nd.$$

Hence  $|d^2 t / \partial x^2| \geq \frac{d/2}{z(n-1)Nd} = \frac{1}{2Nz(n-1)}$ . The maximum Talbot distance is given by  $z_{\max} = Nd^2/2\lambda$ . Using this as  $z$  in the above equation yields

$$|\partial^2 t / \partial x^2| \geq \frac{\lambda}{(Nd)^2(n-1)} = \frac{\lambda}{B^2(n-1)}.$$

For example if  $\lambda = 5 \times 10^{-4}$  mm,  $n - 1 = 1/2$ ,  $B = 10^2$  mm, we obtain

$|\partial^2 t / \partial x^2| \geq 10^{-7} \text{ mm}^{-1} = 1/(10 \text{ km})$ . We note that  $z_{\max}$  can be increased with the addition of plane mirrors that are positioned tangent to the zeroth order beam which effectively increases the grating size due to reflection.

As an example of the system, a perfect thin lens is considered. The phase of this lens is given by  $\phi(x, y) = (-\pi/\lambda f) (x^2 + y^2)$ , where  $f$  is the focal length of the lens, and  $(x, y)$  its coordinates. The relative phase of any object is given by  $\phi(x, y) = (2\pi/\lambda) (n-1) t(x, y)$ , and there-

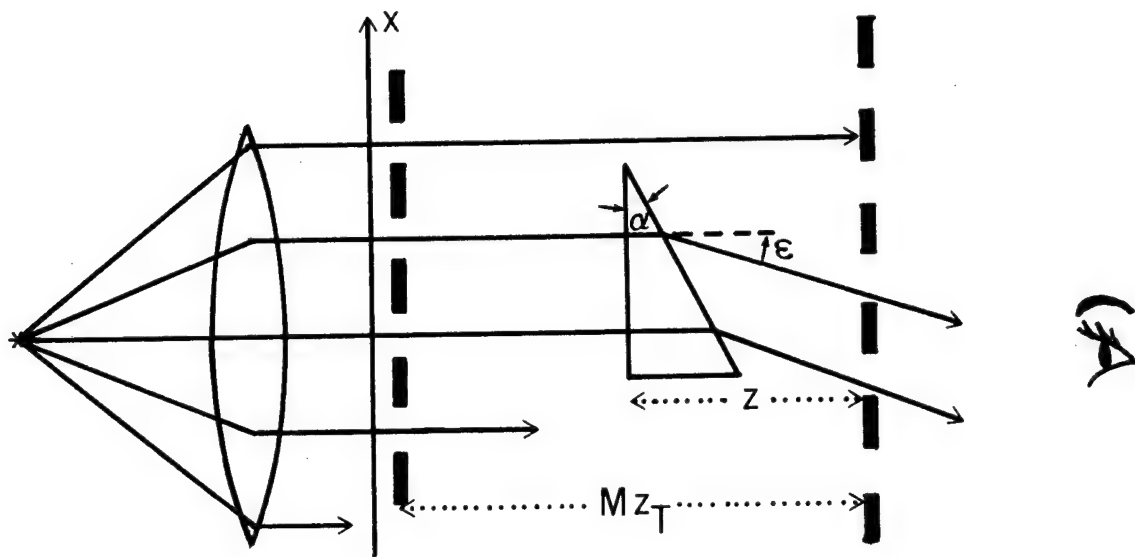


Figure 3. A ray diagram for the lateral shearing interferometer. The prism is a test object that bends the rays through the slits of G2.

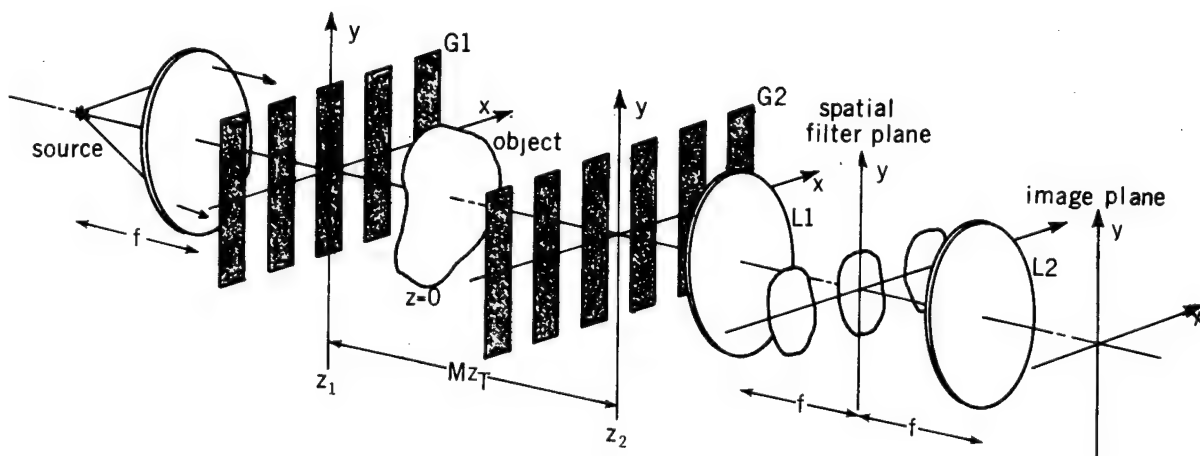


Figure 4. The setup for the Talbot lateral shearing interferometer

fore  $t(x,y) = -(x^2 + y^2)/[2f(n-1)]$ . Thus  $\partial t(x,y)/\partial x = -x[(n-1)f]$ , which when substituted into equation (1) gives  $\varepsilon(x,y) = -x/f$ . This is a straight line that, when compared with conditions for dark fringes, will yield equally spaced fringes of  $fd/z$ . An imperfect lens will not have straight equally spaced fringes, and thus its quality can be determined. It is worth noting that this system likewise tests the collimator objective and can serve as a good method for testing lenses.

### The Lateral Shearing Interferometer

#### Discussion

In this section a rigorous derivation based on scalar diffraction theory is presented. The result will be an interpretation of the image as two, three, or many shifted-object wavefronts, sometimes tilted. Accordingly we will use the terms "shearing interferometry," as is common when two shifted-object wavefronts interact. In generalization thereof we will introduce the terms "triple shearing interferometry" and "multiple shearing interferometry." In some instances these shearing interferences will represent the first or the second derivative of the object. The instrument is diagrammed in figure 4. The spatial coherence requirement is derived in Appendix 1.

#### Theory

Consider a monochromatic plane wave incident on grating G1 in the plane at  $-z_1$ . The field behind this grating is

$$u(x,y,-z_1) = e^{-ikz_1} \sum_{n=-\infty}^{\infty} C_n e^{2\pi i n x/d}$$

where the periodic grating is considered infinite in extent and of period

$d$ , and is expressed as a Fourier exponential series;  $k = 2\pi/\lambda$  where  $\lambda =$  wavelength of light. Following a line of reasoning like Edgar's,<sup>8</sup> the incident plane wave is by action of the grating replaced by a set of plane wavefronts whose  $x$ -direction cosines are  $n\lambda/d$  and whose field strength is proportional to  $C_n$ . The propagating field behind G1 is

$$u(x,y,z) = e^{-ikz_1} \sum_{(n)} C_n e^{\{ik[nx\lambda/d + (z_1+z) \sqrt{1-(n\lambda/d)^2}]\}}$$

which just prior to the object plane  $z = 0-$  reduces to

$$u(x,y,0-) = e^{-ikz_1} \sum_{(n)} C_n e^{\{ik[nx\lambda/d + z_1 \sqrt{1-(n\lambda/d)^2}]\}}$$

Applying the Kirchhoff boundary conditions to the field as it passes through the object, we have

$$u(x,y,0+) = e^{-ikz_1} \sum_{(n)} C_n u_0(x,y) e^{\{ik[nx\lambda/d + z_1 \sqrt{1-(n\lambda/d)^2}]\}} \quad (2)$$

where  $u_0(x,y)$  is the two-dimensional object transmittance function.

Each of the plane waves is diffracted as it passes through the object. At this point, the concept of the angular spectrum is very useful.<sup>9</sup> In this formulation the diffraction phenomenon is a multiplicative quadratic phase factor  $\exp[ikz\sqrt{1-\lambda^2(\nu^2+\mu^2)}]$  in the Fourier domain which increases with the propagation distance  $z$ . Let  $\tilde{u}(\nu,\mu; 0+)$  be the angular spectrum of equation (2) defined by

$$\tilde{u}(\nu,\mu; 0+) = \iint u(x,y, 0+) e^{-2\pi i(\nu x + \mu y)} dx dy$$

where the integration in this section will be over the interval  $(-\infty, \infty)$

when unspecified, and  $(\nu,\mu)$  are the Fourier spatial frequency components.

The angular spectrum for the plane just preceding G2 ( $z = z_2-$ ) is

$$\begin{aligned}
\tilde{u}(v, \mu; z -) &= \tilde{u}(v, \mu; 0+) \exp\{ikz_2\sqrt{1-\lambda^2(v^2+\mu^2)}\} \\
&= e^{-ikz_1} \sum_{(n)} C_n \tilde{u}_0(v-n/d, \mu) e^{\{ik[z_1\sqrt{1-(n\lambda/d)^2} + \\
&\quad z_2\sqrt{1-\lambda^2(v^2+\mu^2)}]\}}
\end{aligned}$$

where  $\tilde{u}_0(v, \mu)$  is the angular spectrum of the object. The Kirchhoff boundary conditions are applied to the second grating at  $z = z_2$

$$u(x, y, z_2+) = u(x, y, z_2-) \sum_{(m)} C_m e^{i\pi m} e^{2\pi i m x/d}$$

where the  $e^{i\pi m}$  factor accounts for the fact that the second grating is shifted by half a period with respect to G1. In the Fourier domain this becomes a convolution which results in

$$\begin{aligned}
\tilde{u}(v, \mu; z_2+) &= e^{-ikz_1} \sum_{(n)} \sum_{(m)} C_n C_m e^{i\pi m} \tilde{u}_0(v-(n+m)/d, \mu) \\
&\quad e^{\{ik[z_1\sqrt{1-(n\lambda/d)^2} + z_2\sqrt{1-\lambda^2[(v-m/d)^2+\mu^2]}\}} \quad (3)
\end{aligned}$$

The image plane is conjugate to the object plane  $z = 0$ . Therefore, we compute the field virtually back to the  $z = 0$  plane in order to find the resultant field in the plane of observation, and give the field a new symbol  $v(x, y)$  with  $\tilde{v}(v, \mu)$  as its Fourier spectrum

$$\tilde{v}(v, \mu) = \tilde{u}(v, \mu; z_2+) e^{\{-ikz_2\sqrt{1-\lambda^2(v^2+\mu^2)}\}}.$$

Substituting equation (3) into this and simplifying by using the first two terms in the Taylor series expansion of the square roots in the exponential terms yields

$$\begin{aligned}
\tilde{v}(v, \mu) &= \sum_{(n)} \sum_{(m)} C_n C_m e^{i\pi m} \tilde{u}_0(v-(n+m)/d, \mu) \\
&\quad e^{\{ik[z_2\lambda^2 v m/d - z_1(n\lambda/d)^2 + z_2(m\lambda/d)^2]\}}.
\end{aligned}$$

But as explained in the first section, the two gratings are separated by some multiple  $M$  of the Talbot distance  $z_T$ . Thus putting  $z_2 + z_1 = M z_T \approx 2Md^2/\lambda$  into the above equation reduces it to

$$\tilde{v}(v, \mu) = \sum_{(n)} \sum_{(m)} C_n C_m e^{i\pi m} \tilde{u}_0(v - (n+m)/d, \mu) e^{\{2\pi i[\lambda z_2 v m/d - z_2 \lambda (m^2 - n^2)/2d^2]\}}. \quad (4)$$

Taking the Fourier transform of this gives the resultant field in the image plane.

$$v(x, y) = \sum_{(n)} \sum_{(m)} C_n C_m u_0(x + m z_2 \lambda/d, y) e^{\{2\pi i[m/2 + (m+n)^2 z_2/z_T + (n+m)x/d]\}}. \quad (5)$$

#### Tilted Ronchi Rulings

Thus far our analysis indicates that the system cannot distinguish a positive from a negative lens, since it is insensitive to the sign of the phase derivative. By rotating the grating of G1, its self-images will correspondingly rotate, and moiré fringes between G2 and these self-images will be observed.<sup>10</sup> The frequency of the moiré fringes and their orientation relative to the gratings are dependent upon the angle  $\alpha$  between the grating's lines and upon each grating's frequency. Unequal grating frequencies cause rotation of the moiré fringes, a fact that was exploited in making a sensitive autocollimator (see Papers 3). In our autocollimator, a diverging wave at G1 causes the self-image to be magnified, which corresponds to a decrease in its frequency, whereas a converging wave increases the frequency. In both cases the Moiré fringes rotate, but in opposite directions. Thus, by the rotation of the fringes, the sign of the curvature of the wave at G1 could be deter-



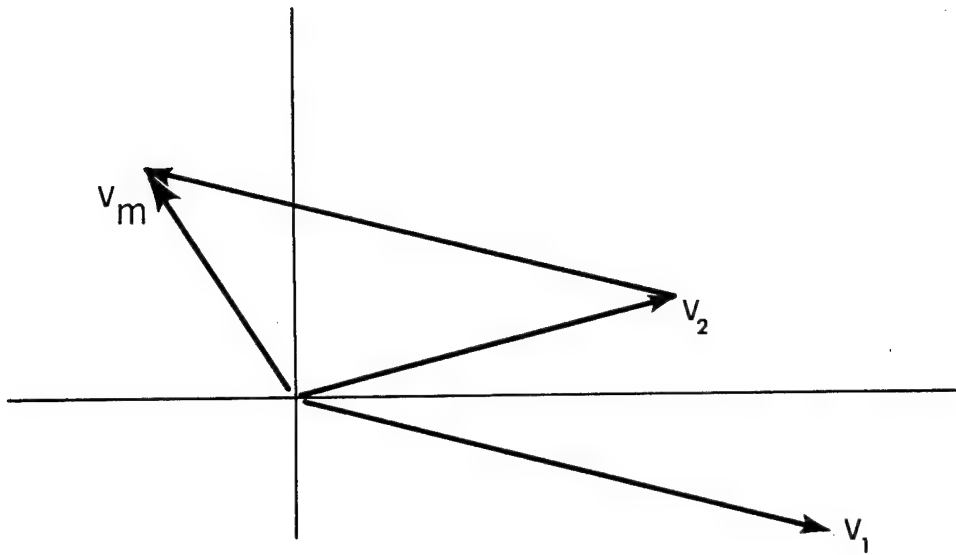


Figure 5(a). The reciprocal space for calculating the moiré effect when  $|v_1| > |v_2|$ .

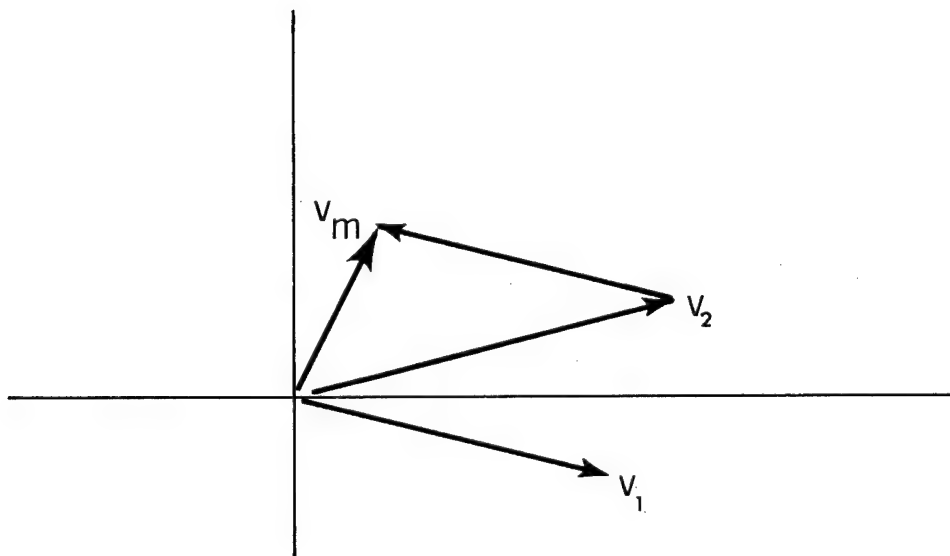


Figure 5(b). The reciprocal space for calculating the moiré effect when  $|v_1| < |v_2|$ .

mined. This phenomenon can be simply understood using a technique by Rogers.<sup>11</sup>

Rogers describes a reciprocal space that is like a Fourier space where vectors in the space describe the frequencies of a grating. Each vector is weighted by its associated Fourier coefficient. The length of the vector corresponds to the value of the grating frequency and its orientation is perpendicular to the grating lines. Our diagram contains vectors for the self-image of G1 and G2. We consider only the fundamental frequency of each grating, since they are the dominant ones in the Moire effect. The vector difference yields the Moire frequency vector.

We rotate G1 by  $-\phi/2$  and G2 by  $+\phi/2$ . Let  $v_1$  be the vector for the self-images and  $v_2$  for G2. For a plane wave  $v_1 = v_2$  and we have Moire fringes parallel to the x-axis. When the self-images are minified, as when G1 is illuminated with converging wave  $v_1 > v_2$ , we have the vector diagram of Fig. 5(a). The Moire vector  $v_M$  has rotated counter-clockwise from its vertical position for  $v_1 = v_2$ . On the other hand, with magnified self-images,  $v_1 < v_2$  and the vector diagram of Fig. 5(b) results. In this case,  $v_M$  has rotated clockwise. By choosing to rotate G1 by  $+\phi/2$  and G2 by  $-\phi/2$ , the above situations would be reversed with clockwise rotation of the Moire fringes, indicating a converging and counter-clockwise rotation indicating a diverging wavefront.

When test objects are placed in the field, the same results apply. Yokozeki and Suzuki<sup>12</sup> have an expression for the locus of these fringes for the Talbot interferometer

$$y = \frac{\cos \alpha - 1}{\sin \alpha} x + \frac{Z}{\sin \alpha} \frac{\partial g(x,y)}{\partial x} + \frac{d}{\sin \alpha} m$$

where  $\alpha$  is the angle between ruling lines defined as positive if G2 is oriented clockwise to G1, Z is the object to G2 distance,  $g(x,y)$  is the distortion of the zeroth order diffraction wave at G2 and  $m$  is an integer. This expression shows that the straight-line Moire fringes are altered in proportion to the first derivative of the distortion. The direction that the fringes rotate is given by the sign of our derivative. As an example, consider an ideal negative lens. The partial derivative is proportional to  $x$ , which would increase the value of the slope for the straight-line function resulting in a counter-clockwise rotation. A positive lens would decrease this slope, giving the fringes an opposite rotation.

#### Filtering

Thus multiple-shearing interferences are observed in the image plane. In ordinary shearing interference only two terms are present,  $u(x + \Delta x, y) - u(x, y)$ . In order to reduce the large number of terms of the double series, we will perform certain spatial filtering operations. The field expressed by equation (4) is found in the spatial plane located one focal length behind the first lens of the telecentric system. In order to filter just the  $n + m = 0$  or  $n + m = 1$  term, which we will show leads to special interferences, we must assume that the shifted spectrums  $\tilde{u}_0(v - (n+m)/d, \mu)$  do not overlap. This is so if the bandwidth restriction of the object  $|\Delta v| \leq 1/2d$ , i.e.  $\tilde{u}_0(v, \mu) = 0$  whenever  $|v| \geq 1/2d$ . It can also be shown that allowing both first orders to pass leads us to the auto-correlation of  $u_0(x, y)$ .

### a. Zero Order Filtering

The multiple shearing interferences can be simplified by spatial filtering. Our first consideration is the case of zero order filtering,  $n + m = 0$ . Thus eq. (5) reduces to

$$v(x,y) = \sum_{(m)} C_m C_{-m} e^{i\pi m} u_0(x+m\Delta, y),$$

where  $\Delta = z_2\lambda/d$  is the shear introduced by the grating to the wavefront under test. If we restrict ourselves to only considering either amplitude or phase modulated gratings that are symmetrical about the origin, then the  $C_m$ 's are real and  $C_m = C_{-m}$ . Thus we can rewrite the above equation as

$$v(x,y) = C_0^2 \left\{ u_0^2(x,y) + 2 \sum_{m \geq 1} (C_m/C_0) e^{i\pi m} [u_0(x+m\Delta, y) + u_0(x-m\Delta, y)] \right\}.$$

These multiple-shearing interferences can be simplified to triple-shearing interferences if  $(C_m/C_0)^2$  terms are all but for the  $m = 1$  term negligibly small. By using a special grating  $g(x) = 1 + \cos(2\pi x/d)$ , triple-shearing interferences would result since  $C_m = 0$  for all  $m > 1$ . We now consider the use of an inexpensive Ronchi ruling as a grating. The Fourier coefficients are  $C_m = (1/2) \text{sinc}(m/2)$ ; all even  $C_m = 0$ , where  $\text{sinc}(x) = \sin(\pi x)/\pi x$ . With this grating the multiple-shearing interferences appear as triple-shearing interferences since  $(C_m/C_0)^2 = 0$  for  $m > 1$ . Note that the highest term neglected,  $n = 3$ , is just one ninth of the smallest term that we kept,  $m = 1$ . Therefore, our equation reduces to

$$v(x,y) \approx C_0^2 \{u_0(x,y) - (C_1/C_0)^2 [u_0(x+\Delta,y) + u_0(x-\Delta,y)]\}$$

Here we have triple-shearing interferences in the image plane of the instrument due to zero order filtering. These triple-shearing interferences become the second derivative of the wavefront when the shear is made very small. To show this we expand  $u_0(x \pm \Delta, y)$  by its Taylor series, and substitute it into the above equation to yield

$$v(x,y) \approx u_0(x,y) [C_0^2 - 2C_1^2] - 2C_0^2 \sum_{p=2}^{\infty} u_0^{(p)}(x,y) \Delta^p / p! \quad (6)$$

where  $u_0^{(p)}(x,y) = \partial^p u_0(x,y) / \partial x^p$ . In order to eliminate the unshifted image from the field of view we must have  $C_0^2 = 2C_1^2$ . This can be done by choosing a grating whose mark-to-space ratio is 1.3. If one uses the Ronchi ruling, this term is still negligible as compared to the second term of eq. (6). This summation term can be shown to be approximately the second derivative by using a theorem by Bernstein<sup>13</sup> which states that the derivatives of a bandlimited function are bounded by the maximum value of the function in the interval. The actual manipulations are done in Appendix 2, the outcome of which states that the maximum shear  $\Delta$  must be less than one-sixth of the width of the smallest details in the object in the direction of shear. This in turn determines the distance  $z_2$  that the object must be placed before the second grating. For spatial filtering we require that  $\Delta v \leq 1/d$ , where the most stringent condition is the equality. This condition is necessary to keep the shifted spectrums in the Fourier domain of our telecentric system from overlapping. Since the shear  $\Delta = z_2 \lambda / d < \delta x / 6 = 1/6 \Delta v = d/6$ , we have  $z_2 < d^2 / 6\lambda = z_T / 12$ . For a Ronchi ruling of 10 lines/mm, this means that the object must be placed within 5 mm of the second grating. With such a placement

of the object and a ruling with mark-to-space ratio of unity, eq. (6) becomes

$$v(x,y) \approx (1/20) u_0(x,y) - (1/10)(z\lambda/d)^2 \partial^2 u(x,y)/\partial x^2,$$

and with a grating of mark-to-space ratio of 1.3, we obtain

$v(x,y) \sim \partial^2 u_0(x,y)/\partial x^2$ . Thus the result of zeroth order filtering is the second derivative of the wavefront under test.

#### b. First Order Filtering

The mathematics for this case follows simply from the previous section. Here we filter either the  $n + m = 1$  or  $n + m = -1$  term. The only difference is in the sign of a phase factor, which is unimportant when detecting the signal. For the  $n + m = +1$ , the field in the image plane becomes

$$v(x,y) = C_0 C_1 e^{2\pi i [x/d + z/z_T]} \{u_0(x,y) - u_0(x+z\lambda/d,y)\}.$$

This surprising result occurs since the even coefficients are zero.

Those terms which contribute under the  $n + m = 1$  condition are  $C_m C_n = C_m C_{m-1}$ , implying that for any  $m \neq 0$ , one coefficient will always be even and hence equal to zero. This is very much like ordinary shearing interferometry, and we will again show that under a certain condition this is approximately the derivative of the object. We ignore the phase since it is the intensity which is observed in the image plane, and deal with the bracketed terms. The last term is expanded in a Taylor series around  $z\lambda/d$ ; combined with  $u_0(x,y)$  it gives

$$\{...\} = \sum_{p \geq 1}^{\infty} u_0^{(p)}(x,y) (z\lambda/d)^p (1/p!) \approx u_0^{(1)}(x,y) (z\lambda/d).$$

Using the same kind of arguments as in the previous section, this approxi-

mation is valid if the shift  $z\lambda/d \lesssim 1/5\pi\Delta v \approx (1/15)\delta x$ . Under the strictest condition  $|\Delta v| = 1/d$ , this means that the object to G2 distance is  $z \leq z_T/10\pi$ . Therefore, the field in the image plane for first order filtering under these two conditions, whichever may apply, is given by

$$v(x,y) \approx (z\lambda/2d\pi) (\partial u_0(x,y)/\partial x),$$

which is essentially the first derivative of the object. We ignore the multiplicative phase factors since we detect intensity and note that the first order filtering gives us essentially the first derivatives of the object  $v(x,y) \sim \partial u_0(x,y)/\partial x$ .

## Experiments

The Talbot shearing interferometer was assembled on a laboratory bench using two Ronchi rulings of 10 lines per mm pitch as gratings. The second grating was mounted in a holder that could be rotated or shifted laterally, thereby allowing the gratings to be aligned as desired. Both a helium-neon laser and a tungsten lamp were used as light sources. Color fringes of high contrast were obtained with the tungsten lamp but will not be presented because of the cost of color printing. The output of a laser was collimated with a 6 micron pinhole and 250 mm focal length objective producing a 50 mm beam. The second grating was located in one of the self-image planes of the first. Objects to be tested were inserted between the gratings at a distance from the second grating that introduced the desired shear. The method of observing interference fringes was to project the object with its fringe structure onto a screen. Thus, the fringes overlap the corresponding regions of the object to which they apply.

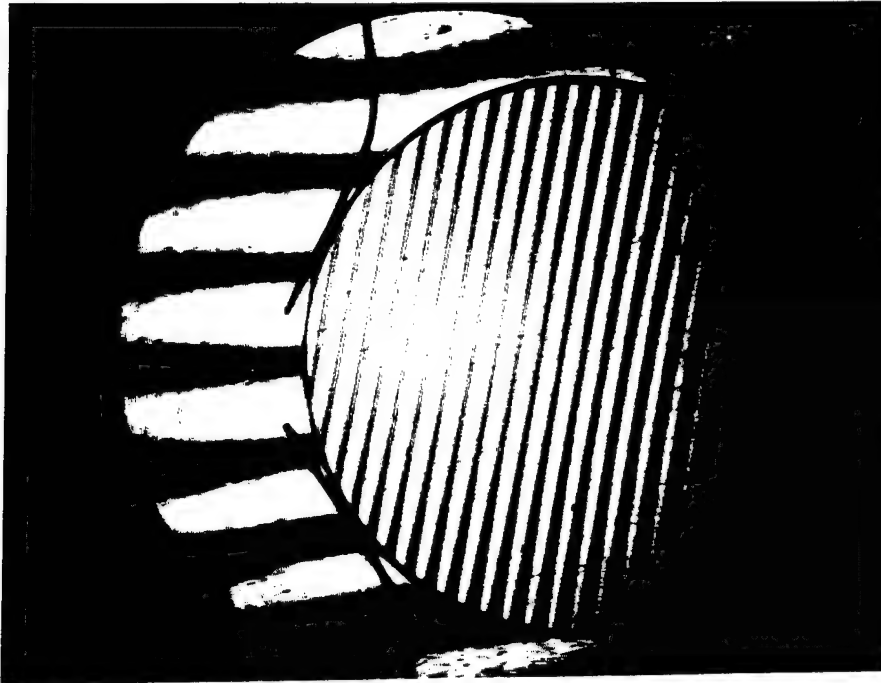


Figure 6. A lens tested in the lateral shearing interferometer showing fringes of equal phase derivative. Horizontal moiré fringes appear in the background.



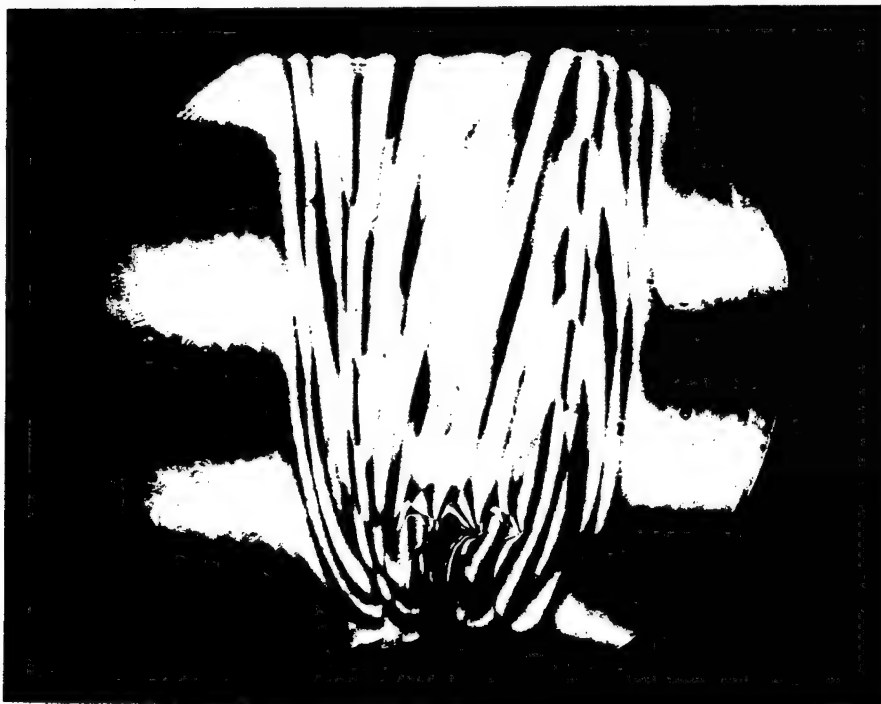


Figure 7(a). Zeroth order filtering of the wavefront that has passed through the medium heated by a candle flame. The three candle wicks verify that triple shearing interferences are observed.

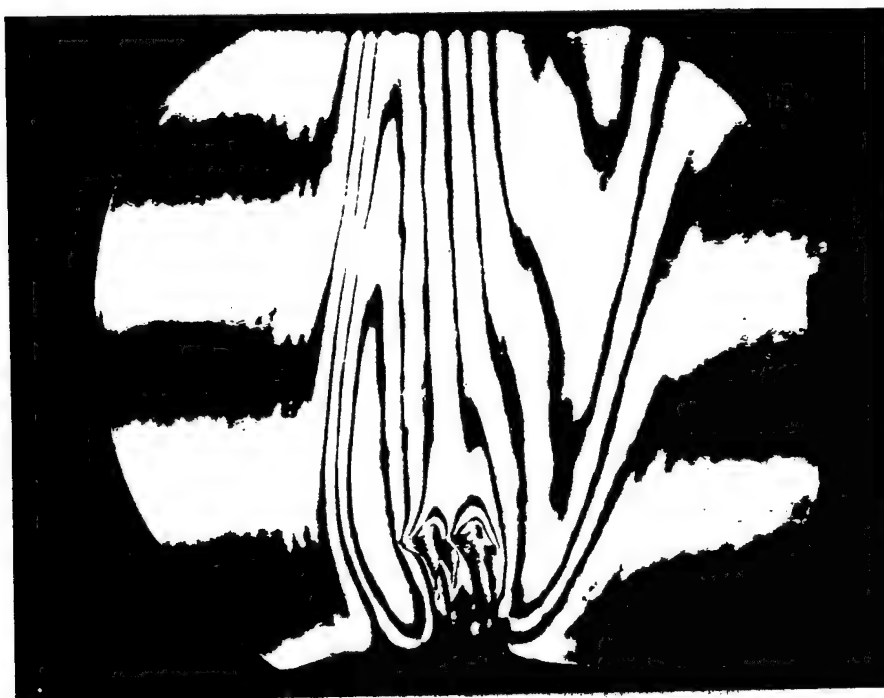


Figure 7(b). First order filtering of the same object as in (a). Double shearing interferences are observed.

The case of a lens was discussed in the opening section. Straight fringes were predicted for a lens with only quadratic phase terms; this is shown in Figure 6. One feature not discussed previously is the addition of the moiré fringes in the background. This is caused by a slight rotation of the second grating with respect to the self-image of the first. This in turn causes the fringes to rotate.

Heated gases can be studied by this technique since the gas will have a refractive gradient. A candle flame was placed before G1. We used both a uniform dark field and a Moire pattern for our background while observing the nimbus of the candle. These pictures have been published in our earlier publication in Paper I figs. 3(a) and 3(b). The addition of the Moire fringes enhances our ability to observe the fringe location and gives us the sign of the derivative.

As a demonstration of spatial filtering, this same candle flame was spatially filtered. The shear was made excessively large so that triple- and double-shearing interferences could be recognized by counting the replication of some unique section of the object such as the wick of the candle. In the experiment the candle flame was separated from the second grating by 90 cm, causing a shear of about 5.6 mm. Zeroth-order filtering is demonstrated in figure 7(a). Three wicks are clearly observable indicating triple-shearing interferences. The two sheared wicks are of lesser contrast than the unsheared ones, as predicted by the theory. In figure 7(b) we have first-order filtering which produces double-shearing interferences. These two candle wicks are of equal contrast as expected from our theory.

## Constant Radial Shearing Interferometer

### Discussion

In our previous instrument using Ronchi rulings, the derivative of a wavefront perpendicular to the ruling lines was displayed by a set of interference fringes. Imagine that we possess a "flexible" Ronchi ruling. Bending this flexible grating into a complete circle gives us a circular grating where the derivative is still perpendicular to the lines, but the lines are now concentric circles. Therefore, we expect that such a grating in a Talbot interferometer setup would give us the radial derivative.

In the succeeding sections we will learn that for experimental reasons the first four periods of a grating are ignored ( $r \leq 4a$ ) and that self-images of a circular grating exist outside of a region defined by a cone along the optical axis. The radius of this cone increases as we move farther from the grating ( $r = \lambda z/a$ ). Combining both restrictions gives us  $r \leq 4a + z/a$ . This region is excluded when evaluating the output of our new instrument.

As we will see, the constant radial shearing interferometer, like the lateral shearing interferometer, gives color fringes of high contrast when white light is used as a source, and yields double or triple shearing interferences with spatial filtering. These filtered interferences become the first and second radial derivative of the wavefront, respectively, when the shear is less than the width of the object details of interest. Experimental evidence will be presented.

### Definition of a Circular Grating

A circular grating consists of a number of concentric circular rings on a transparent surface.<sup>15</sup> Every other ring is opaque, and the ratio of opaque rings to transparent ones is chosen by the experimenter in a fashion that will be discussed under spatial filtering. The transmittance of the grating  $G(r)$  shown in Figure 8 is given by

$$G(r) = \begin{cases} \sum_{(m)} C_m e^{2\pi i m r/a}, & 4a < r \leq A \\ 0 & \text{otherwise} \end{cases} \quad (7)$$

where the grating is represented by its Fourier exponential series,  $C_m = \alpha \text{sinc } m\alpha$ ,  $r$  is the radial location of any point on the grating,  $a$  is the periodicity of the structure,  $\alpha a$  is the dimension of the transparent section, and  $2A$  is the diameter of the grating. Since in the manufacture of circular gratings the innermost part is not as perfect as the outermost parts, the first four periods of the grating have been ignored. This experimental necessity will turn out to simplify some theoretical considerations.

### A Qualitative Explanation of Self-Imaging with Circular Gratings

Linear gratings are known to self-image, and self-images of circular gratings have been observed. To intuitively understand why circular gratings can self-image, consider the outermost part in a sector of a circular grating. In this region the circular grating is approxi-

mately like a linear grating. Therefore, it is plausible that a circular grating, like a linear grating, will self-image.

Another way to answer this is to show that the circular grating belongs to the subset of radially symmetric objects that self-image. The complete set of self-imaging objects was derived by Montgomery.<sup>14</sup> He assumed that a plane monochromatic wave impinged upon the object. He then solved the wave equation in Cartesian coordinates while asking the following question: "What are the necessary and sufficient conditions that the object must satisfy in order that a faithful image of it be found in a parallel plane  $z = z_T > 0$ ?" The solution placed restrictions on the spatial frequency domain for the self-imaging objects. For objects whose spatial frequency is much less than  $\lambda^{-1}$  (Montgomery calls this "weak imaging") we have

$$v^2 + \mu^2 = 2n/\lambda z_T; \quad \rho_n = \sqrt{2n/\lambda z_T} \quad (8)$$

where  $v$  and  $\mu$  are the  $x$  and  $y$  components of the spatial frequency,  $n$  is an integer,  $\lambda$  is the wavelength, and  $z_T$  is the distance for self-imaging. Hence, the Fourier spectrum of a Talbot object can only exist on a set of concentric circles whose radii are given by  $\rho_n$ . Therefore, the Fourier spectrum for the subset of objects with radial symmetry that can self-image will also lie on these concentric circles. By changing Montgomery's solution to polar coordinates and using the fact that our objects have no angular dependence, the exact solution for this subset can be determined. We find that the Fourier spectrum, in addition to lying on the concentric circles, is also independent of the angular coordinate. If the circular grating belongs to the Talbot set of radially symmetric objects, then its Fourier spectrum must behave in the same manner. Since

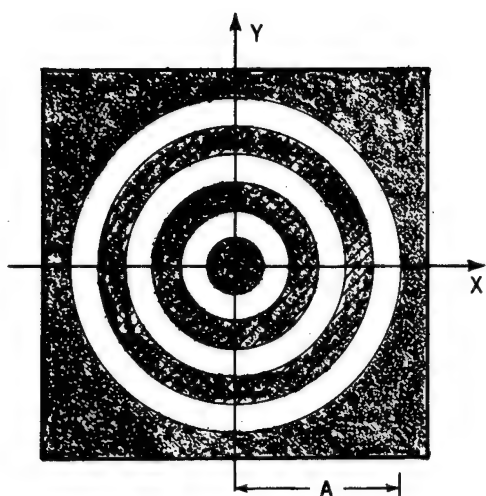


Figure 8(a). A schematic representation of a circular grating.

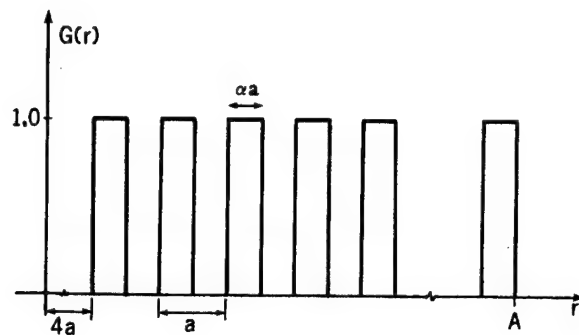


Figure 8(b). The transmittance function of the circular grating where the first four periods have been ignored.

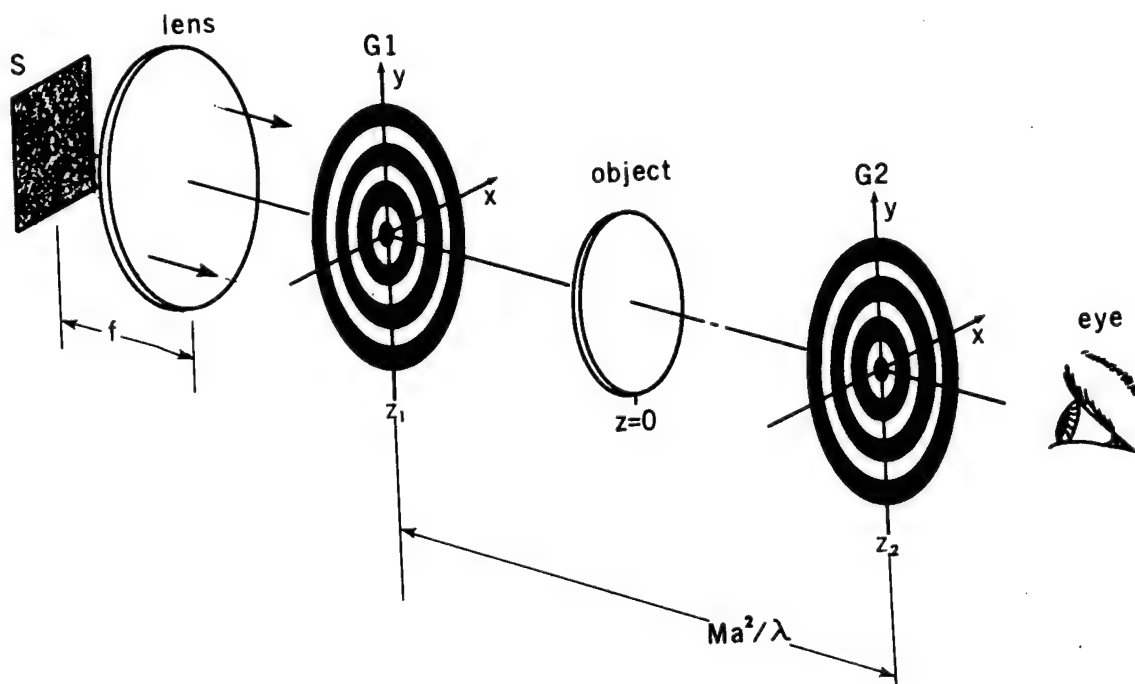


Figure 9. The basic Talbot constant radial shearing interferometer setup.

this grating can be expressed as a Fourier series (eq. (7)), we conclude that its Fourier spectrum is probably confined to equidistant rings given by  $\rho_m = m/a$ . These rings will belong also to the larger family of non-equidistant rings of eq. (8) if we select  $n = 0, 1, 4, 9 \dots m^2$  and  $a = \sqrt{\lambda z_T/2}$  or  $z_T = 2a^2/\lambda$ . This equation is the same as the original Talbot formula for linear gratings. Hence we have shown qualitatively that circular gratings are a subset of the self-imaging objects.

## Theory

### a. General

The Talbot interferometer consists of two identical circular gratings G1 and G2 separated by a distance such that G2 lies in one of the negative self-image planes of G1 (see Figure 9). For the position of G2 we choose a negative self-image, midway between self-image planes, so that *differences* (and not sums) in the object will be observed. Or we obtain these differences by replacing G2 with a negative of G1. The second grating is now placed in one of the self-image planes of the first. We also use a plane in which the self-image is sharp so that our fringes will have their highest contrast. The gratings are aligned with their centers coaxial to the beam direction. Therefore in the absence of an object under test a uniform dark field is observed behind G2. Between the two gratings at a distance  $z_2$  from G2, a transparent object is inserted. An observer focuses his eye on the object through the second grating so that the fringes overlap the regions to which they apply. Although a white light source may be used, we will limit our theoretical considerations to a monochromatic plane wave. The deriva-

tion of our formulas is contained in the next section.

A monochromatic plane wave impinges upon the circular grating G1 and is diffracted. The Huygens-Fresnel-Kirchhoff equation<sup>16</sup> describes the field behind G1 and can be solved by the method of stationary phase.<sup>17</sup> The solution is not valid in the inner cone of diffraction defined by  $r < \lambda z'/a$  (see Fig. 10), where we have assumed that for experimental reasons the first four periods of the grating are ignored. A phenomenological justification for excluding this region from further consideration in the instrument lies in the nature of the Talbot effect. We recognize that outwardly diffracted rays form divergent conical wavefronts and inwardly diffracted rays form convergent conical wavefronts. The interference between a plane wave, a divergent conical wave and a convergent conical wave is utilized for the circular Talbot effect. These three waves overlap in the shaded areas of Fig. 11, and form rings around the z-axis with a ring width decreasing to zero at  $z = aA/2\lambda$ . The inner cone (cross-hatched region) is one of the zones that does not belong to the ring domain. This region is to be ignored in evaluating the output of the instrument and is usually a small fraction of the usable field.

Ignoring the first four periods of the grating is not serious since it is only a small portion of the total grating area. We could actually block off this region,  $0 \leq r < 4a$ , thereby avoiding contributions from this mathematically unmanageable area. But we did not do so since we know that light from that small portion will be mostly only in the inner cone, which we will neglect when evaluating the output.

The result of our analysis in the next section gives the output of the instrument,  $v(r,\varphi)$ , as



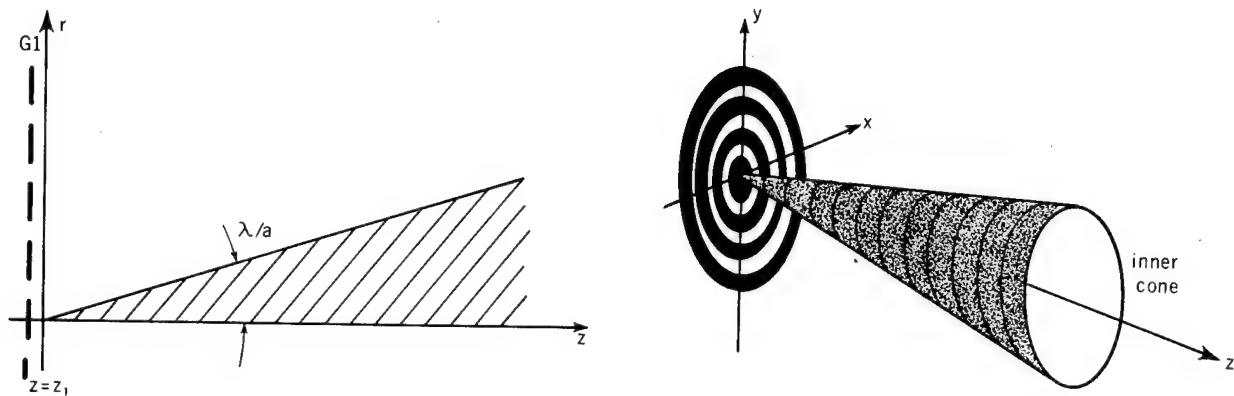


Figure 10. A diagram in two and three dimensions illustrating the inner cone.

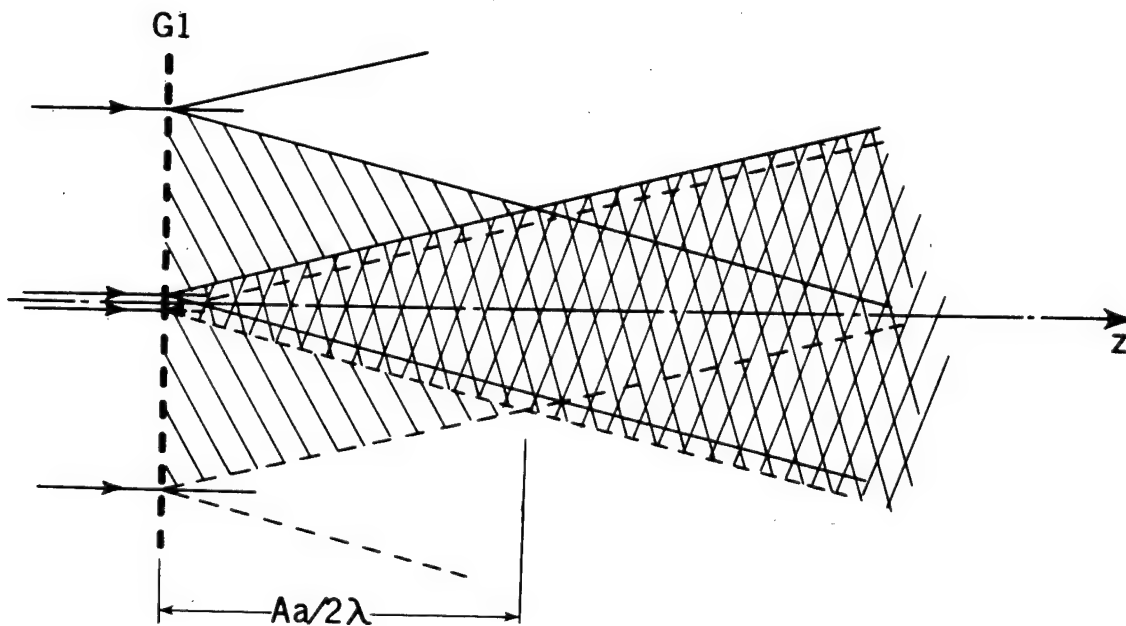


Figure 11. A two dimensional drawing of the propagation of the first diffracted orders. The Talbot effect occurs only within the cross-hatched regions.

$$v(r, \varphi) \sim \sum_{(m)} \sum_{(n)} C_m C_n e^{i\pi m} e^{2\pi i(m+n)r/a} u_0(r - m\Delta, \varphi), \quad (9)$$

where  $\Delta = \lambda z_2/a$ ,  $u_0(r)$  is the object's transmittance function, and  $e^{i\pi m}$  is a consequence of placing G2 in a negative Talbot image. This equation contains both exponential Fourier series of G1 and G2, and shows that the complex amplitude of the object is shifted radially by multiples of  $\Delta$ . The amount of shear depends upon the distance that the object is placed from the second grating ( $z_2$ ) as well as the angle of the diffracted orders ( $\lambda/a$ ).

It is argued in the next section that further simplification of this equation can be achieved by observing that our Fourier coefficients decrease by  $1/m$  and that terms associated with high frequencies are decreased by whatever observational method used. Furthermore  $C_2, C_4, \dots = 0$  if we use square grating grooves. The result of these approximations gives us

$$v(r, \varphi) \sim C_0^2 \{u_0(r, \varphi) - (C_1/C_0)^2 [u_0(r + \Delta, \varphi) + u_0(r - \Delta, \varphi)]\}.$$

As with the case of linear gratings the mark-to-space ratio is under the control of the experimenter, who can choose  $(C_1/C_0)^2 = 1/2$  (i.e. mark-to-space ratio of 1.3), so that  $v(r, \varphi)$  becomes

$$v(r, \varphi) \sim u_0(r, \varphi) - \frac{1}{2} [u_0(r + \Delta, \varphi) + u_0(r - \Delta, \varphi)].$$

When the radial shear is made smaller than the width of the object details this equation is essentially the second radial derivative of the object,

$$v(r, \varphi) \sim \partial^2 u_0(r, \varphi) / \partial r^2.$$

## b. Analysis

The Talbot interferometer with circular gratings is sketched in Figure 9, which shows all the appropriate dimensions and symbols. A plane monochromatic wave impinges on G1, and the complex amplitude of the wavefield immediately behind G1 is

$$u(r, z_1^+) = \exp(ikz_1) G(r),$$

where  $G(r)$  is the transmission function of the circular grating given earlier. We will ignore all constant multiplicative phase factors in this derivation since the final observed quantity will be intensity.

Beyond G1 we have Fresnel diffraction from our propagating wave field that is described by the Huygens-Fresnel-Kirchhoff integral,

$$u(r, \varphi, z) \sim \frac{1}{\lambda z'} \int_0^\infty \int_0^{2\pi} u(r', z_1^+) \exp\{i\pi[r^2 + r'^2 - 2rr'\cos(\varphi - \varphi')]/\lambda z'\} r' dr' d\varphi'$$

where  $(r, \varphi)$  and  $(r', \varphi')$  are polar coordinates in plane  $z$  and  $z_1^+$  respectively,  $z' = z - z_1$ , and the approximation sign is to remind us that we have used the Fresnel approximations and that the constant multiplicative phase factors have been dropped.

Integrating over  $\varphi'$ , substituting  $G(r)$  for  $u(r, z_1^+)$  into the remaining integral and then interchanging summation and integration order we have

$$u(r, z) \sim \frac{2\pi}{\lambda z'} \sum_{(m)} C_m \int_{4a}^A r' J_0(2\pi r r' / \lambda z') \exp\{i\pi[2rm/a + (r'^2 + r^2)/\lambda z']\} dr'.$$

The method of stationary phase that solves integrals of this type cannot be applied since the Bessel function oscillates too wildly

over the region of stationarity to be approximated by a constant. By using the trigonometric approximation for the Bessel function we can place the oscillating parts into the phase term, leaving us with a slowly varying function. The approximation is

$$J_0(x) \sim \sqrt{2/\pi x} \cos(x - \pi/4); \quad x > 25,$$

and therefore

$$r' J_0(2\pi r r' / \lambda z') \sim \sqrt{\lambda z' r' / r} \{ \exp i\pi[2\pi r r' / \lambda z' - 1/4] + \exp -i\pi[2\pi r r' / \lambda z' - 1/4] \}$$

if  $2\pi r r' / \lambda z' > 25$ , or  $r > 4\lambda z' / r'$ .

Recall that we were to ignore the first four periods of the grating for experimental convenience since the innermost parts of a circular grating are more difficult to manufacture than the outer parts. The additional value to this exclusion is that the factor  $\sqrt{\lambda z' r' / r}$  will be a slowly varying function for  $r' > 4a$  and that therefore the method of stationary phase is applicable. We conclude that the Bessel approximation is good if  $r > \lambda z' / a$ . This means that we exclude from our consideration in the instrument a region defined by a cone about the  $z$ -axis whose angle with the axis is equal to the angle of the first diffracted order  $\lambda/a$ . Using this approximation in our equation for the field at  $z$  we obtain

$$u(r, z) \sim \frac{1}{\lambda z'} \sum_{(m)} C_m \int_{4a}^A \sqrt{\lambda z' r' / r} \left\{ \exp i\pi \left[ \frac{(r' - r)^2}{\lambda z'} + \frac{1}{4} + \frac{2\pi r r'}{a} \right] + \exp i\pi \left[ \frac{(r' + r)^2}{\lambda z'} - \frac{1}{4} + \frac{2\pi r r'}{a} \right] \right\} dr'$$

This equation consists of two parts; the first part accounts for contributions to a point  $P$  in the plane  $z$  from the grating for  $r' < 0$

giving us a path difference of  $(r - r')$  while the second part consists of contributions for  $r' < 0$  that give a path difference  $(r + r')$ . Figure 12 shows these two contributions. The method of stationary phase is applied to the integral.

The point of stationarity for the first part is  $r_0' = r - m\lambda z'/a$ . We wish to know the complex wave field at P that lies in plane z at a distance r from the optical axis. But r must lie within the regions where self-imaging interferences occur (see Fig. 11). Therefore, not all diffracted orders m will contribute to the integral. In Figure 13 we have plotted the stationary point as it falls in the r - z plane for positive values of m. It is apparent from this drawing that orders  $m + 1$  and greater will fall within the shaded region in the plane  $\hat{z}$  where no self-imaging occurs. Therefore this diagram helps us to determine the positive diffracted orders  $\leq m$  that place  $r_0'$  within the interval of integration  $(4a, A)$ . In like manner we can determine the negative diffracted orders. The results of our computation give us

$$\hat{z} < [(A - 4a)a/\lambda](1 + |m|) = (N - 4)z_T/2(1 + |m|); \quad A = Na$$

where  $z_T = 2a^2/\lambda$  is the self-imaging distance and N is the number of lines in the grating.

When z is a small fraction of  $(N/2 - 2)z_T$  then many orders of m contribute. The strength of the various orders is proportional to the Fourier coefficients. As we have stated earlier, only the zeroth and two first orders are significant. In this case  $z < Nz_T/4 - z_T \approx Aa/2\lambda$ , as stated earlier. We will carry all the orders in our computation and take only those into account that lie within the instrument's operating range when evaluating the output.

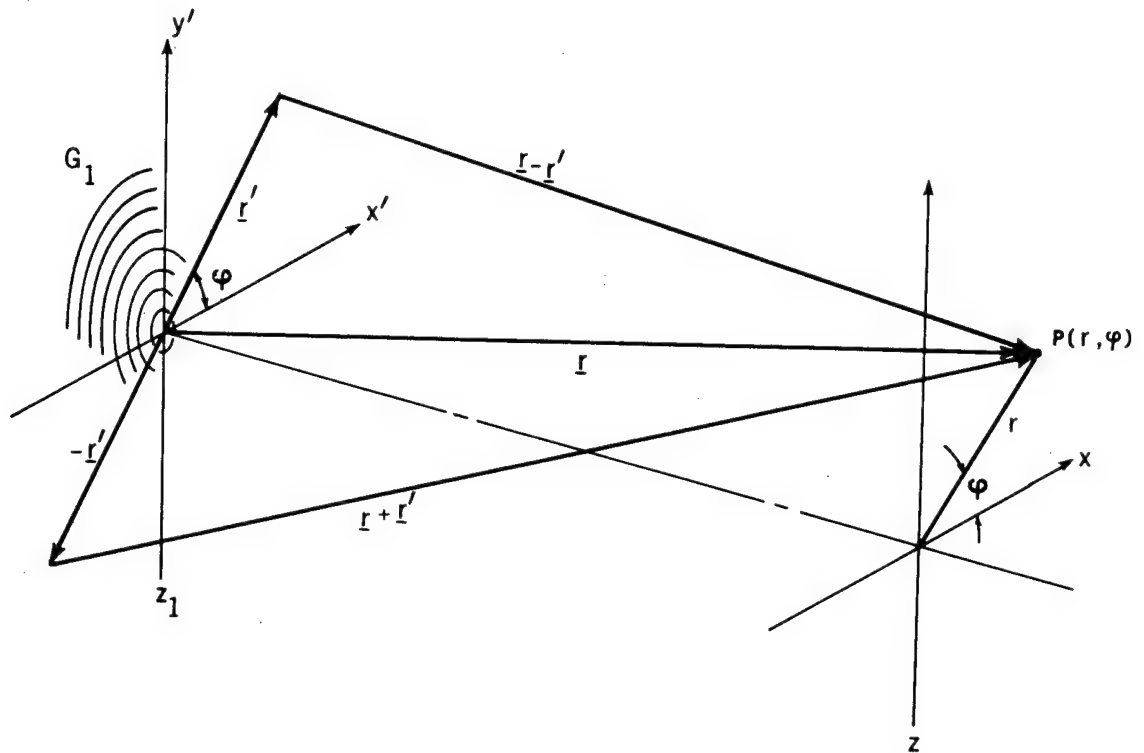


Figure 12. A diagram illustrating the contributions to the point  $P(r, \phi)$  from regions  $r < 0$  and  $r > 0$  in the grating.

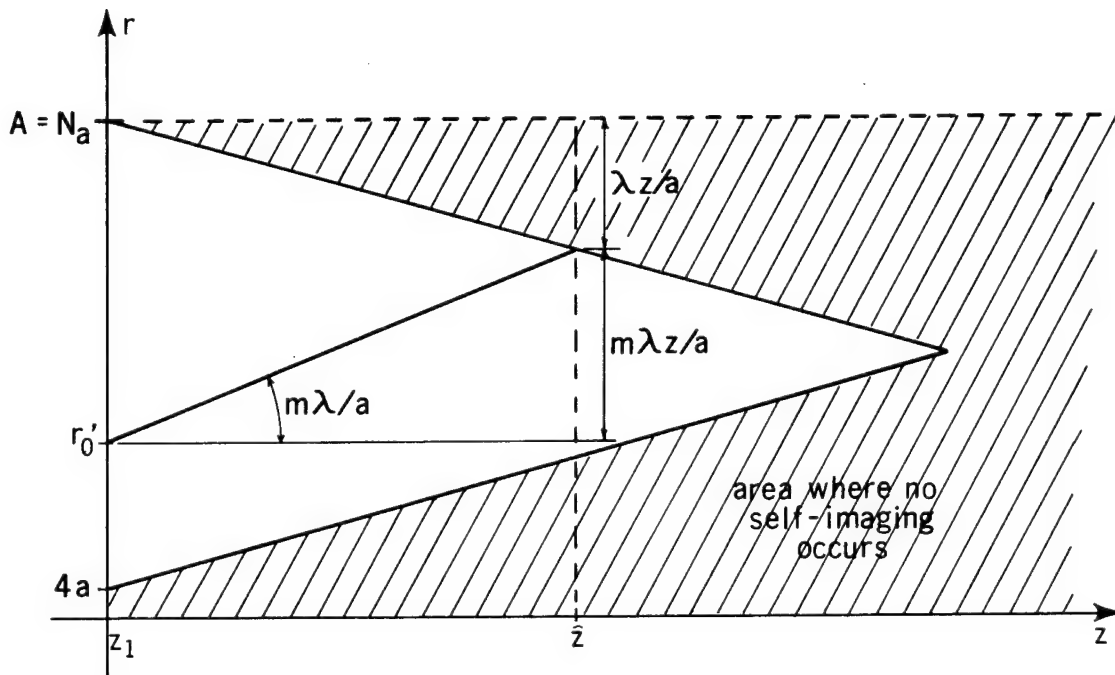


Figure 13. A plot of the stationarity point for that region of the grating that lies above the  $x$ -axis ( $r - r'$ ).

Applying the method of stationary phase to the first part gives us

$$u_1(r, z) \approx \sum_{(m)} c_m \sqrt{1 - (m\lambda z'/ra)} e^{-i\pi\lambda z'(m/a)^2} e^{2\pi imr/a},$$

where  $u_1(r, z)$  is the contribution due to the first part of the integral.

The point of stationarity for the second part of the integral is  $r_0' = -r - m\lambda z'/a$ . For  $m \geq 0$ , the stationary point lies outside of the region of integration  $(4a, A)$ , and therefore does not contribute to the integral. For  $m = -1$ , the stationarity lies inside the inner cone that we are excluding from our instrument in order that our approximation be valid. The remaining values of  $m$  ( $m < -1$ ) do not significantly contribute to the integral since this contribution is multiplied by the associated Fourier coefficients which are decreasing by  $1/m$ , or by  $(1/m)^2$  in intensity. Thus the contribution of this second part to the integral is negligible in comparison with the first part, and therefore our field  $u(r, z)$  is given by the computation for  $u_1(r, z)$

$$\begin{aligned} u(r, z) &\approx u_1(r, z) \\ &\approx \sum_{(m)} c_m \sqrt{1 - (m\lambda z'/ra)} e^{-i\pi\lambda z'(m/a)^2} e^{2\pi imr/a}. \end{aligned}$$

In the plane just preceding the object ( $z = 0^-$ ), the field is

$$u(r, 0^-) \sim \sum_{(m)} c_m \sqrt{1 + (m\lambda z_1/ra)} e^{i\pi\lambda z_1(m/a)^2} e^{2\pi imr/a},$$

and just behind the object we have

$$u(r, \varphi, 0^+) = u(r, 0^-) u_0(r, \varphi),$$

where  $u_0(r, \varphi)$  is the complex amplitude of our object that we want to test. In the region beyond the lens the propagating wave field is

computed again by use of the Huygen-Fresnel-Kirchhoff formulation,

$$u(r, \varphi, z) \sim \frac{1}{\lambda z} \int_{f_g(z)}^{f_u(z)} \int_0^{2\pi} u(r, \varphi, 0^+) \exp\{i\pi[r^2 + r'^2 - 2rr'\cos(\varphi - \varphi')]/\lambda z\} r' dr' d\varphi',$$

where we limit the integration to the self-image field,  $f_u(z) = A - \lambda z/a$ , and  $f_g(z) = 4a + \lambda z/a$ . We expand our test object  $u_0(r, \varphi)$  in a Fourier exponential series

$$u_0(r, \varphi) = \sum_{(p)} u_p(r) e^{ip\varphi},$$

since any object is periodic in  $\varphi$ . Placing this into our integral and integrating over  $\varphi'$ , we have

$$u(r, \varphi, z) \sim \frac{2\pi}{\lambda z} \sum_{(m)} \sum_{(p)} C_m e^{i\pi(m/a)^2 \lambda z_1} e^{ip(\varphi - \pi/2)} \int_{f_g(z)}^{f_u(z)} r' \sqrt{1 + m\lambda z_1/r'a} J_p(2\pi r r'/\lambda z) u_p(r') \exp\{i\pi[(r^2 + r'^2)/\lambda z + (2mr'/a)]\}$$

In order to solve this by the method of stationary phase we approximate the Bessel function as before and again find that we must ignore the inner cone. Since this new inner cone lies within the inner cone of the grating G1, no further restrictions are required in the theory of the instrument. Hence,

$$2\pi r' \sqrt{1 + m\lambda z_1/r'a} J_p(2\pi r r'/\lambda z) \sim \sqrt{\lambda z/r} \sqrt{r' + m\lambda z_1/a} \cos[2\pi r r'/\lambda z - \pi/4 - p\pi/2],$$

where  $r > \lambda z/a$  and  $r' \geq 4a$  as before.

Let the cosine term be represented by its exponential equivalence,



and our field equation becomes

$$u(r, \varphi, z) \sim \sqrt{1/\lambda z r} \sum_{(m)} \sum_{(p)} C_m e^{i\pi(m/a)^2 \lambda z_1} e^{ip(\varphi - \pi/2)} \int_{f_\ell(z)}^{f_u(z)} \frac{dr'}{\sqrt{r' + m\lambda z_1/a}} \{ \exp i\pi[(r' - r)^2/\lambda z + 1/4 + p/2 + 2mr'/a] + \exp i\pi[(r' + r)^2/\lambda z - 1/4 - p/2 + 2mr'/a] \} dr'$$

The second part is approximately zero as before, and the first part gives us

$$u(r, \varphi, z) \sim \sum_{(m)} \sum_{(p)} C_m e^{-i\pi(m/a)^2 \lambda (z - z_1)} \sqrt{1 - m\lambda(z - z_1)/ra} u_p(r - m\lambda z/a) e^{ip\varphi} e^{2\pi i m r/a}.$$

Note that our test object is duplicated and shifted by multiples of  $\lambda z/a$ . The field just prior to the second grating is obtained by setting  $z = z_2$ . The above equation becomes

$$u(r, \varphi, z_2^-) \sim \sum_{(m)} C_m e^{-i\pi(m/a)^2 \lambda (z_2 - z_1)} \sqrt{1 - m\lambda(z_2 - z_1)/ra} u_0(r - m\lambda z_2/a, \varphi) e^{2\pi i m r/a}$$

where we have used  $u_0(r, \varphi) = \sum_{(p)} u_p(r) e^{ip\varphi}$ .

The field just behind the second grating is

$$u(r, \varphi, z_2^+) = u(r, \varphi, z_2^-) G(r) \approx \sum_{(m)} \sum_{(n)} C_m C_n \sqrt{1 - m\lambda(z_2 - z_1)/ra} e^{-i\pi\lambda(m/a)^2(z_2 - z_1)} u_0(r - m\lambda z_2/a, \varphi) e^{2\pi i(m+n)r/a}. \quad (10)$$

For maximum contrast, we choose  $z_2 - z_1 = Ma^2/\lambda$ , where  $M$  is an integer.

Furthermore, since we want to see *differences* (not sums) in object

detail, we choose that  $M$  should be an odd integer. We have  $\exp i\pi\lambda(m/a)^2(z_2 - z_1) = \exp i\pi m$ , which gives us the necessary negative sign for odd integers. The full significance of this is deferred until the spatial filtering section. With this distance our equation becomes

$$u(r, \varphi, z_2^+) \sim \sum_{(m)} \sum_{(n)} C_m C_n e^{i\pi m} e^{2\pi i(m+n)r/a} \sqrt{1 + mMa/r} u_0(r - m\lambda z_2/a, \varphi).$$

This equation contains both exponential Fourier series of  $G_1$  and  $G_2$ , and shows that the complex amplitude of the field is shifted radially by multiples of  $\lambda z_2/a$ . The amount of shear depends upon the distance that the object is placed from the second grating as well as the angle of the diffracted orders. The square root term accounts for the increase or decrease in the size of the object due to either.

To simplify our mathematical manipulations we would like to work in the area where  $\sqrt{1 \pm Ma/r} \sim 1 \pm Ma/2r \approx 1$ . This means that  $Ma/2r \ll 1$  or  $r \gg Ma/2$ . Recall from eq. (10) that this term is  $\sqrt{1 - \lambda(z_2 - z_1)/ra}$ . Therefore,  $r \gg \lambda(z_2 - z_1)/2a$ . This states that  $r$  must be greater than a cone which lies within the inner cone that we are already ignoring for aforementioned reasons. Thus the square root term is close to 1 for the region outside the inner cone. Thus our equation simplifies to

$$v(r, \varphi) \equiv u(r, \varphi, z_2^+) \sim \sum_{(m)} \sum_{(n)} C_m C_n e^{i\pi m} e^{2\pi i(m+n)r/a} u_0(r - m\Delta, \varphi), \quad (11)$$

where  $\Delta = \lambda z_2/a$  is the shear introduced, and  $v(r, \varphi)$  is a new symbol to indicate the observed field.

The only significant terms of this equation are for  $m = -1, 0, +1$ . Our Fourier coefficients decrease by a factor  $1/m$ . And the next significant coefficient  $C_3$  ( $C_2 \approx 0$ ) is one-third that of  $C_1$ . Since our Fourier coefficients are in pairs, we can compare  $C_3 C_0$ , which is the next largest term that we can ignore, with  $C_1^2$ , which is the smallest term that we will keep, and see that the term that we will throw away is less than one-half that of the smallest term we keep. Furthermore this  $n = 0, m = 3$  term contains fairly high spatial frequencies as evidenced by the term  $\exp 2\pi i 3r/a$ . These high frequencies will be further reduced in contrast by whatever observational method is used: eye, camera, or film. A detailed justification of this statement is involved since we would have to consider the spatial frequency spectrum of the intensity (after a modulus square operation). Under these assumptions our equation reduces to

$$\begin{aligned} v(r, \varphi) \sim & C_0^2 u_0(r, \varphi) - C_1^2 \{u_0(r+\Delta, \varphi) + u_0(r-\Delta, \varphi)\} \\ & + C_0 C_1 \cos(2\pi r/a) u_0(r, \varphi) \\ & - u_0(r+\Delta, \varphi) \{C_1^2 e^{-4\pi i r/a} + C_0 C_1 e^{-2\pi i r/a}\} \\ & - u_0(r-\Delta, \varphi) \{C_1^2 e^{4\pi i r/a} + C_0 C_1 e^{2\pi i r/a}\} \end{aligned}$$

As we have just stated, the terms with the exponential quantities contain very high frequencies and the contrast of these terms will be attenuated or even eliminated by the observational method as with a grating with a period too fine for the eye to resolve. Therefore,

$$v(r, \varphi) \sim C_0^2 u_0(r, \varphi) - C_1^2 u_0(r+\Delta, \varphi) + u_0(r-\Delta, \varphi) .$$

If  $(C_1/C_0)^2 = 1/2$ , then we have

$$v(r, \varphi) \sim C_0^2 \{u_0(r, \varphi) - 1/2[u_0(r+\Delta, \varphi) + u_0(r-\Delta, \varphi)]\},$$

and this equation is approximately the second radial derivative when the shear is smaller than the object details of interest. Hence

$$v(r,\varphi) \sim \partial^2 u_0(r,\varphi)/\partial r^2.$$

To obtain  $(C_1/C_0)^2 = \text{sinc}^2 \alpha = 1/2$  we choose  $\alpha = 0.44$  or a mark-to-space ratio of 1.3. In conclusion, we see that the output of the Talbot interferometer with circular gratings is triple shearing interferences. These triple shearing interferences become the second derivative when the shear is made smaller than the object details. The shear in turn is proportional to the distance that the object under test is placed from the second grating.

#### Shifted Circular Gratings

In this technique the second grating which lies in one of the self-image planes is shifted laterally a distance  $s$  from the self-image. Thus the rings of equal diameter for  $G_2$  and the self-image overlap on the perpendicular bisector of the line joining their centers. A phase object inserted between the gratings a distance  $z$  from  $G_2$  causes the rays passing through it to bend by an angle  $\alpha$  (see Figure 14(a)). Thus the rings of the self-image are distorted and the overlapping rings will deviate from the perpendicular bisector as in Figure 14(b). We will generalize Lau's Dupligranmm-method<sup>18</sup> from Fresnel Zone Plate rings to equidistant rings. The deviation will be shown to measure the aberration

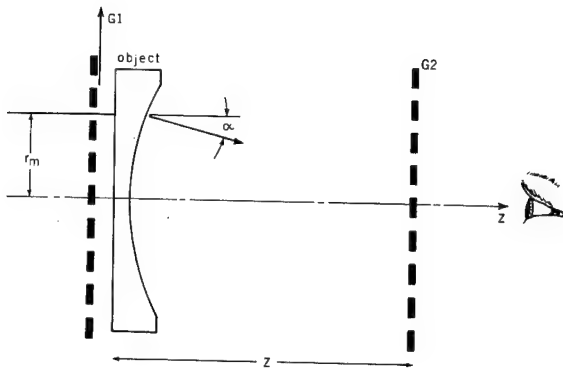


Figure 14(a). A ray diagram illustrating how an object bends the rays in a circular Talbot interferometer.

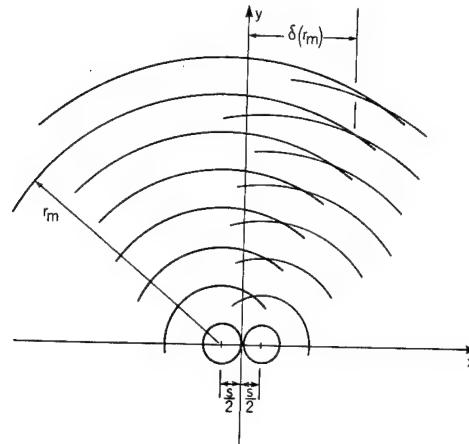


Figure 14(b). The two circular gratings are shifted with respect to each other causing moiré fringes. When one circular grating is deformed then the distance from the y-axis of the intersections is a measure of this distortion.

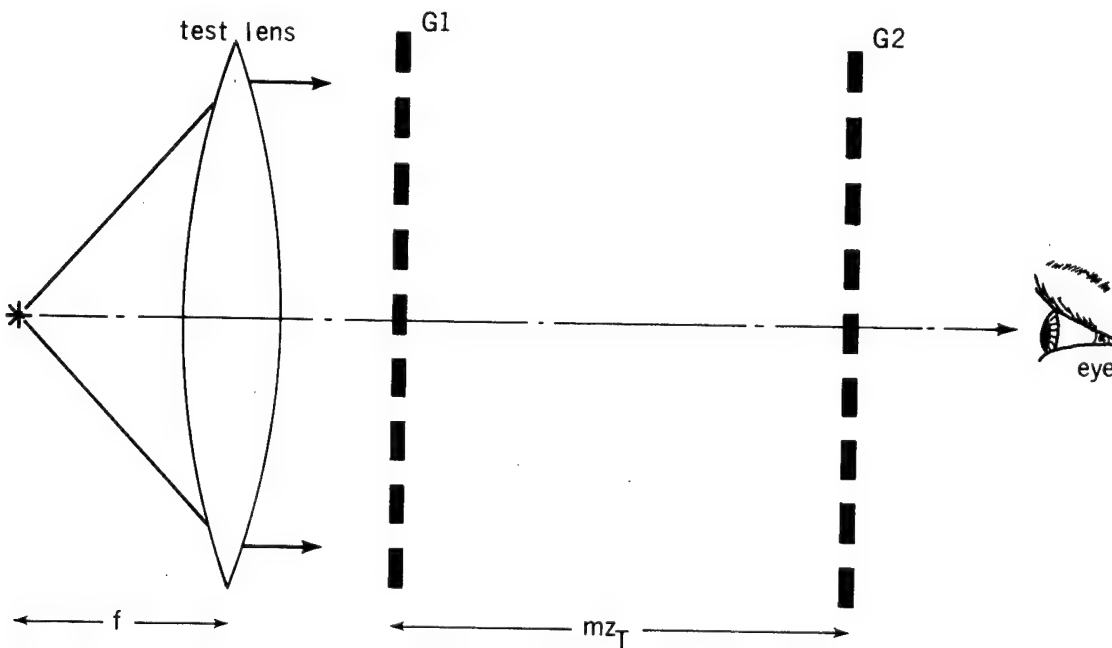


Figure 15. Using the lens under test in collimation increases the sensitivity of the test since the unwanted focusing term is biased out in collimating the source.

of a test lens, where  $\alpha = \alpha(r)$  describes the angular aberrations of the lens under test.

The opaque circular rings of G2 lie on radii  $r_m = ma$  ( $a$  is the grating period). The distorted rings of the self-image lie on radii  $r_m' = r_m - \alpha z$ . We choose our coordinate axis in the plane of G2 such that the x-axis joins the two centers of the two concentric circular ring structures and the y-axis lies on the perpendicular bisector as shown in Figure 14(b). The equation for the circles of our two ring structures are:

$$(x + s/2)^2 + y^2 = r_m^2; \quad (x - s/2)^2 + y^2 = r_m'^2.$$

The simultaneous solution of these two equations gives us the coordinates of the overlapping rings. Solving for  $\delta(r_m)$ , which is the x-coordinate of the moiré fringe closest to the y-axis, we have

$$\delta(r_m) = [\alpha(r_m)z/s] [r_m - \alpha(r_m)z/2].$$

We can always choose the lateral shift  $\alpha(r_m)z \ll 2r_m$  so that the deviation is simply related to the deviations,

$$\delta(r_m) \approx z r_m \alpha(r_m)/s.$$

As an example we pick a lens where  $\alpha_{\text{lens}} = \alpha_1 r + \alpha_3 r^3 + \dots$ . The term  $\alpha_1 r$  describes the focal power while  $\alpha_3 r^3 + \dots$  are the spherical aberration terms of interest. We can eliminate the  $\alpha_1 r$  term by using the test lens in collimation as shown in Figure 15. In this configuration we have  $\alpha_{\text{lens}} - \alpha_1 r = \alpha(r_m)$ . Therefore

$$\delta(r_m) = [\alpha(r_m)z/s] [r_m - \alpha(r_m)z/2].$$

For small distances  $r_m$ ,  $\alpha(r_m) \approx 0$  since the lens has no aberrations on axis. For larger distances  $r_m$  we choose  $\alpha(r_m)z \ll 2r_m$  so that

$$\delta(r_m) \approx (zr_m/s) \alpha(r_m).$$

The distance  $z$  is equal to the separation of the gratings. We see that the deviations from the  $y$ -axis  $\alpha(r_m)$  are simply related to the angular aberrations of the lens.

## Filtering

The setup for spatial filtering is shown in Figure 16. It requires the addition of a telecentric system placed behind G2 to make it possible to separate out the various diffracted orders, by placing a binary mask in the filter plane. The analysis and setup are analogous to the lateral shearing interferometer. The results are identical if we replace the variable  $x$  by  $r$ . The usual bandwidth restrictions for spatial filtering apply. Thus the bandwidth  $\Delta\rho$  of our object  $u_0(r, \varphi)$  must be less than  $1/a$ . Physically this means that the grating period must be less than the tiniest object details that we wish to resolve.

### a. Zeroth-order Filtering

By zeroth-order filtering we mean that only those rays that are approximately parallel to the optical axis beyond G2 are allowed to reach the observation screen. This is accomplished with a telecentric system that focuses these rays to a point on the optical axis. This is illustrated in Figure 17. A binary filter with an aperture large enough to allow these rays to pass, but small enough to reject the other orders, is placed in this plane. Thus only terms with  $m + n = 0$  in eq. (10)

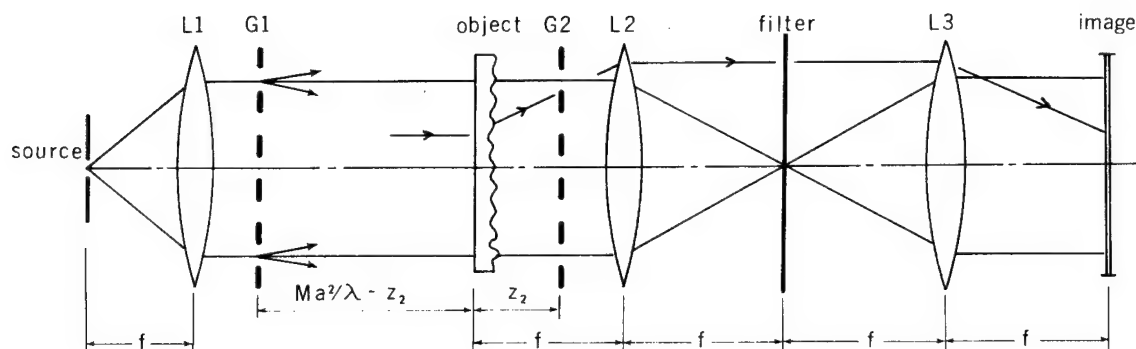


Figure 16. The Talbot interferometer modified to do spatial filtering. The telecentric system provides a filter plane for the insertion of the binary filter and the image plane is conjugate to the object.

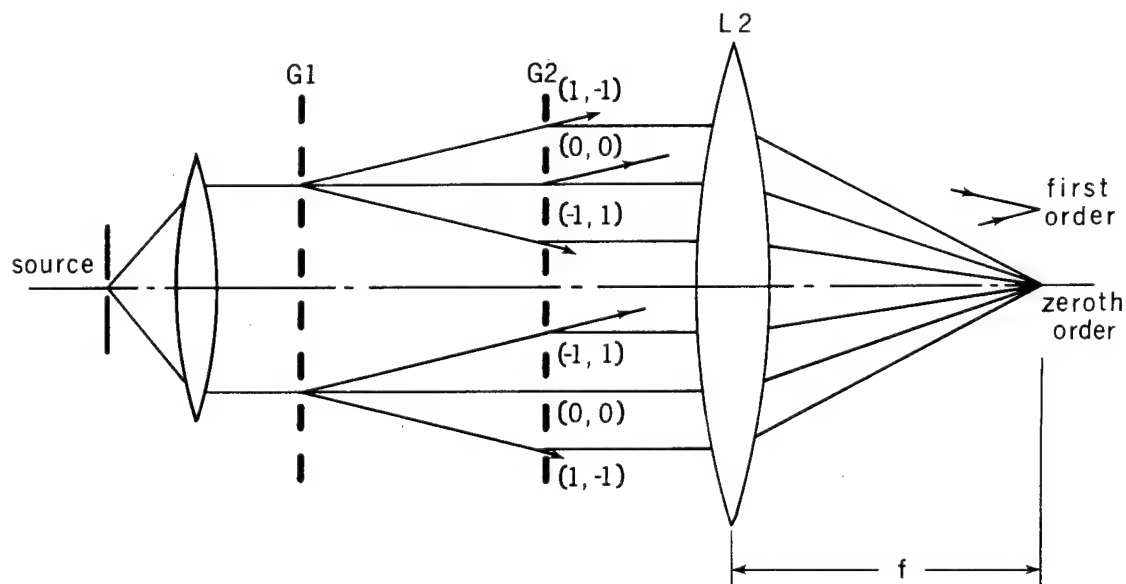


Figure 17. A diagram showing how the zeroth diffracted order is filtered.



will appear in the final output of the instrument. In order that filtering be accomplished, the zeroth order must not overlap terms with different  $(m + n)$  orders. Thus the bandwidth  $\Delta\rho$  of our object  $u_0(r, \varphi)$  must be less than the inverse of the period of our grating ( $\Delta\rho < 1/a$ ). Physically, this means that the grating period must be smaller than the tiniest object details that we wish to resolve. If we place an opaque mask with a disc opening of radius  $\lambda f/2a$  into the back focal plane of L2, then what we observe at the screen is

$$v(r, \varphi) \sim \sum_{(m)} C_m^2 e^{i\pi m} u_0(r - m\Delta, \varphi).$$

Only terms with  $m = -1, 0, +1$  of this equation are significant, since  $C_2 \approx 0$  and  $C_3^2 \sim C_1^2/9$ . Therefore, we have

$$v(r, \varphi) \sim C_0^2 u_0(r, \varphi) - (C_1/C_0)^2 [u_0(r+\Delta, \varphi) + u_0(r-\Delta, \varphi)] .$$

If we choose a mark-to-space ratio of 1.3, then  $(C_1/C_0)^2 = 1/2$ , and the above equation becomes

$$v(r, \varphi) \sim u_0(r, \varphi) - (1/2)[u_0(r+\Delta, \varphi) + u_0(r-\Delta, \varphi)].$$

If the shift  $\Delta$  is much less than the tiniest object details we wish to observe, then this equation approximates the second derivative,  $v(r, \varphi) \sim \partial^2 u_0(r, \varphi) / \partial r^2$ . This result is similar to our previous unfiltered result. There we did low-pass filtering with the frequency limitations of the observational method. When the gratings can be resolved by the eye or other recording media, then one sees the grating structure superimposed on the object. For this case, zeroth order filtering would be desirable.

## b. First-order Filtering

First-order filtering is just as easily accomplished, but the setup must be modified slightly in order to achieve the first radial derivative. Figure 18 demonstrates that both first-order diffraction rays intermingle in the back focal plane of the lens, making it impossible to separate out either the  $m + n = +1$  or  $-1$  term. A simple remedy to restore order is to block one half of the grating. In this way rays from the lower half do not intermingle with the upper rays in the diffraction pattern.

Since the  $m + n = +1$  or  $-1$  term lies in a semicircle, an opaque mask with a transparent semi-annulus will transmit either one of the first orders (see Fig. 19). This modified setup means that one half of our circular grating is blocked.

Fortunately, our theoretical analysis is only modified by a constant factor  $1/2$  as discussed in Appendix 3. Thus the output of this modified setup is  $1/2$  that of eq. (9), i.e.,

$$v(r, \varphi) \sim \frac{1}{2} \sum_{(m)} \sum_{(n)} C_m C_n e^{i\pi m} e^{2\pi i(m+n)r/a} u_0(r - m\Delta, \varphi).$$

With the insertion of the semi-annular binary mask, only the  $m + n = +1$  (or  $m + n = -1$ , if we rotate the annulus by  $\pi$  radians) will pass through to the screen. With a Ronchi ruling all even Fourier coefficients are zero. Therefore, the field at the screen is

$$v(r, \varphi) \sim \frac{1}{2} C_0 C_1 [u_0(r, \varphi) - u_0(r - \Delta, \varphi)] e^{2\pi i r/a}.$$

If we drop the uninteresting factor  $\exp 2\pi i r/a$  from further consideration, and introduce a shear that is smaller than the tiniest

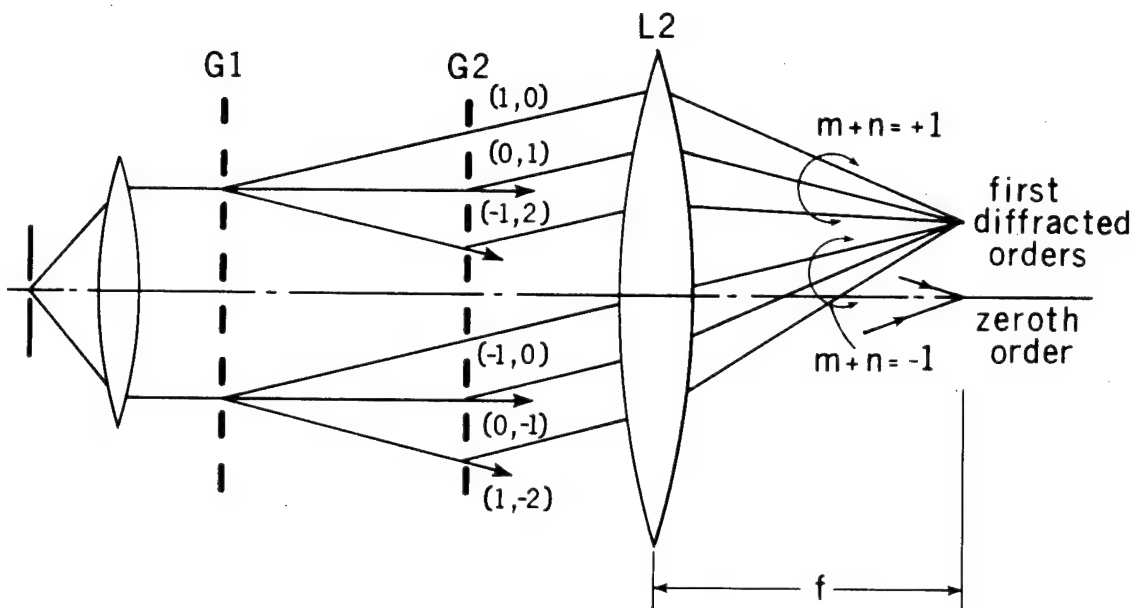


Figure 18. A diagram showing the intermingling of the negative and positive first diffracted orders, thereby making it impossible to do first order filtering.

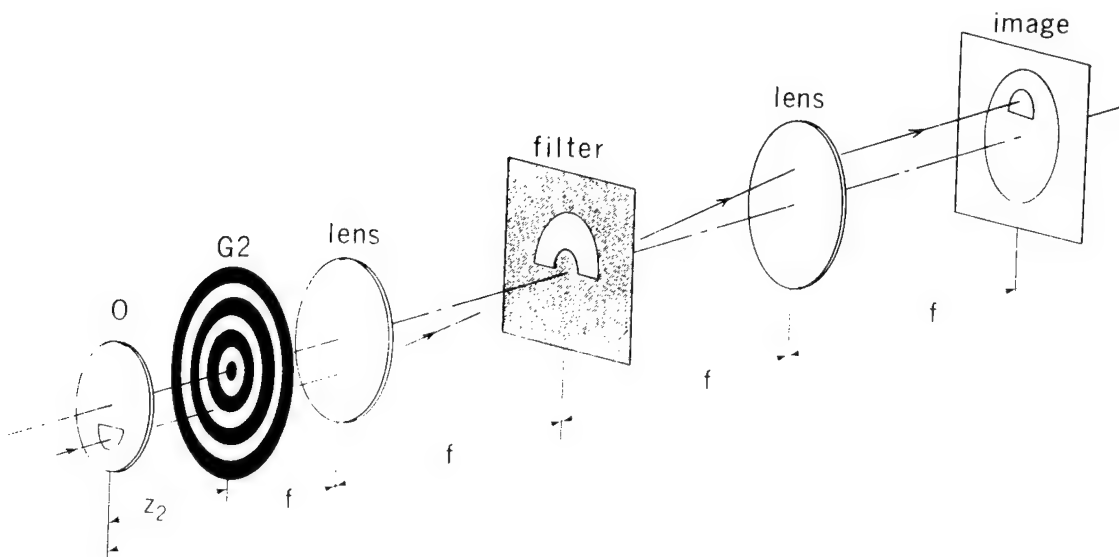


Figure 19. The tail end of the interferometric setup showing the semiannular spatial filter used with first order filtering.

object details of interest, then our equation reduces to the first radial derivative,  $v(r,\varphi) \sim \partial u(r,\varphi)/\partial r$ .

## Experiments

Our circular gratings were photographic reductions of the circular pattern that is included in the Edmund Scientific moiré kit. Two identical gratings were made. Our gratings were examined under a microscope and determined to have a mark-to-space ratio of about 1. Spatial filters were made from photographs of drawings that were reduced to the required size. Both xenon-arc and helium-neon laser were used as sources. Color fringes of high contrast were observed with the xenon arc. We present only our black and white work.

The interferometer was set up on a laboratory bench according to the schematic of Figure 9. A 5 mW helium-neon laser beam was expanded to 50 mm by a 250 mm effective focal length objective and filtered with a 6-micron pinhole. Our first circular grating G1 was placed within the beam and another identical grating G2 was centered in one of the negative self-image planes of G1. The negative self-image plane in which G2 is inserted is chosen so that the test object which is between the gratings can be placed sufficiently far away from G2 to yield the desired shear. A uniform dark field is observed at the screen. Inserting a test object produces moiré fringes through a distortion of the first grating's negative self-image at G2. For photographic purposes, a lens was placed behind G2 with the film plane conjugate to the object.

#### a. No Filtering

The fringe pattern for a bifocal lens is shown in Paper 2, Fig. 2. We used Kodak's high-contrast copy film. The fringes are contours of constant phase derivative. Note that the smaller lens contains more fringes than the larger one due to its higher focal power. The object is aligned so that the optical axis for the large lens is collinear with the optical axis of the system as we see from the circular fringes. The smaller lens has horseshoe-type fringes since it is off-axis and we are looking at its off-axis aberrations.

Moiré fringes in the shape of hyperbolas are observed when two circular gratings are shifted laterally with respect to each other, and look very much like spikes for small shifts. If our test object is a candle flame, the spikes will be deformed by the change in refraction index of air due to heat. In Paper 2, Fig. 3 is a photograph of this experiment where the candle is approximately 13 cm from G2.

#### b. Shifted Gratings

As stated above, shifted circular gratings produce moiré fringes in the shape of hyperbolas. There is also a moiré fringe due to the overlapping of rings of equal diameter that fall on the perpendicular bisector of the line joining the centers of the shifted gratings. We can display this fringe alone by using a small shift  $s$  between the grating centers.

It was shown earlier that with the addition of a phase object the deviation  $\delta$  from the perpendicular bisector is simply related to the

angle through which the ray is bent. For the case of a lens in collimation,  $\delta$  was simply related to the aberrations of the lens. Figure 20 shows a lens of 380 mm focal length in the collimation setup. The shift  $s = 0.07$  mm and  $z = 57$  cm. The deviations  $\delta$  are a measure of this lens's aberration.

### c. Filtering

Filtering is accomplished by means of binary masks placed in the Fourier plane of the transform lens L2 that separates one diffracted order from another. The location of the filter plane depends on the focal length of L2 and sometimes also on the object if it happens to be a lens. Should the test object be a bifocal lens with focal lengths  $f_1$  and  $f_2$ , for example, then two Fourier planes exist and filtering cannot be done in either plane without eliminating information located in the other. Under certain conditions there exists an intermediate plane in which the orders are separated, and the filter can be inserted there. The condition under which this region exists is given in Appendix 4 as  $\lambda/a > \gamma h_1(f_1^{-1} - f_2^{-1})M$ , where  $h_1$  is the height of that part of the object with focal length  $f_1$ ,  $\gamma$  is a number less than 1 and depends upon the angle at which the diffracted orders meet, and  $M$  is the magnification of the object at the screen. Note that the condition is independent of the focal length of the transforming lens.

Our demonstration of triple and double-shearing interferences for zeroth and first-order filtering respectively uses a ring cut from brass tubing with an outside diameter of 19.05 mm and an inside diameter of 15.37 mm and soldered to a post. If the shear  $\Delta$  exceeds the thickness,

then individual rings will be observed. In this way it is sufficient to count the number of rings to determine whether double or triple shearing interferences are obtained by simple filtering. The ring was inserted a distance 973 mm from G2. That gave a shear ( $\Delta = \lambda z_2/a$ ) of 2.4 mm, thereby insuring that our images would be separated.

For zeroth-order filtering a binary mask with a transparent disc is placed in the filter plane. The diameter of the disc is such that the periphery of the disc falls midway between the zeroth and first diffraction orders. At the observation screen we observe

$$|v(r,\varphi)|^2 \sim C_0^4 |u_0(r,\varphi)|^2 + C_1^4 \{ |u_0(r+\Delta,\varphi)|^2 + |u_0(r-\Delta,\varphi)|^2 \}.$$

The intensity of the unshifted ring is associated with  $C_0^4$  while the intensity of the shifted rings are associated with  $C_1^4$ . Hence the shifted rings will be of lower contrast than the unshifted ring. A photograph of this is presented in Fig. 21(a). One half of the field is blocked for convenience when comparing this figure with the first-order filtering of Fig. 21(b).

For first-order filtering one half of the circular grating is blocked to separate positive and negative orders; a semiannular ring is placed in the filter plane, oriented to pass either  $n + m = +1$  or  $n + m = -1$  diffracted orders. In the photograph of Figure 21(b), we show the result of passing the positive order. Two rings of equal contrast are observed as predicted by the theory. One image is unshifted and the other is shifted away from the axis. Rotating the semiannulus by 180 degrees allows the negative diffracted order to pass. In this case, we would have an unshifted image and another image of equal intensity shifted toward the axis. Comparing this photograph with that of the

previous figure demonstrates that spatial filtering with simple binary masks can produce either double or triple shearing interferences.



Figure 20. The aberrations of the lens tested with shifted circular gratings are directly displayed as deviations from a straight line passing through the center. Virtually no aberrations are visible near the optical axis.





Figure 21(a). A ring object under test in the constant radial interferometer. A large shear is introduced by placing the object 93 cm from G2. Zeroth order filtering produces triple shearing interferences and only one half of the field is viewed.

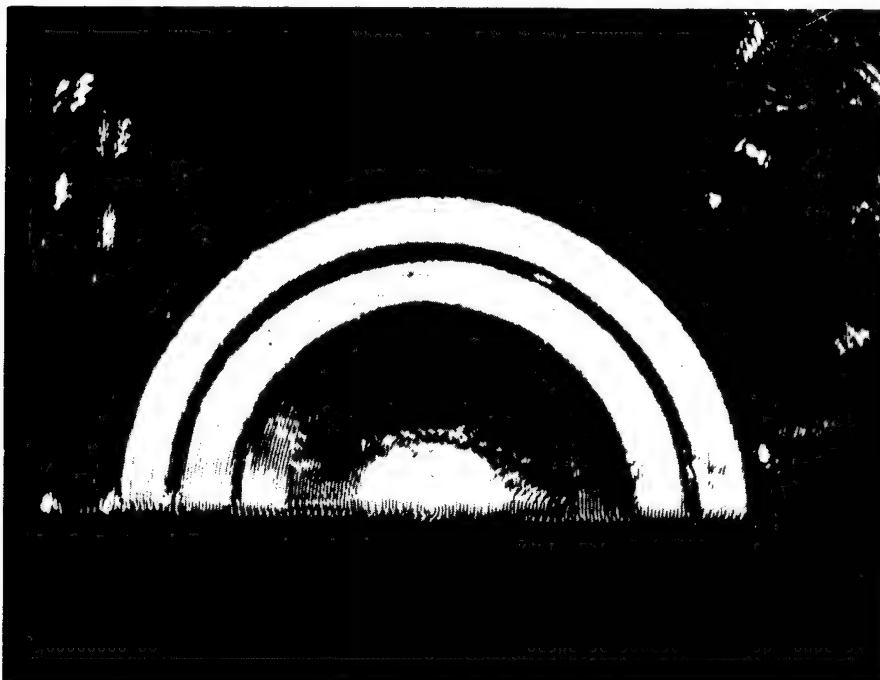


Figure 21(b). The same setup as (a) except that first order filtering is used.

### References for Chapter III

1. O. Bryngdahl, Progress in Optics IV, edited by E. Wolf, North-Holland, Amsterdam, 1965, pp. 39-83.
2. E. Waetzmann, Ann. Phy. 39, 1042 (1912).
3. O. Bryngdahl, J. Opt. Soc. Amer. 61, 169 (1971).
4. A. Lohmann and D. Silva, Opt. Comm. 2, 413 (1971).  
S. Yokozeki and T. Suzuki, Appl. Opt. 10, 1575 (1971).  
D. Silva, Appl. Opt. 10, 1980 (1971).  
A. Lohmann and D. Silva, Opt. Comm. 4, 326 (1972).
5. Y. Nishijima and G. Oster, J. Opt. Soc. Amer., 54, 1 (1964).
6. A. Lohmann and D. Silva, Opt. Comm. 2, loc. cit.
7. A. Lohmann, Proc. Conf. Opt. Instruments and Techniques, 1961, London, Chapman and Hall, 1962, p. 58.
8. R. F. Edgar, Optica Acta 16, 281 (1969).
9. J. Goodman, Introduction to Fourier Optics, McGraw-Hill, 1968, p. 48.
10. J. M. Burch, Progress in Optics, ed. Wolf, North-Holland, 1963.
11. G. L. Rogers, Proc. Phys. Soc., Lond 73, 142 (1959).
12. S. Yokozeki and T. Suzuki, loc. cit.
13. J. Arsac, Fourier Transforms and the Theory of Distributions, Prentice Hall, 1966, p. 315.
14. W. D. Montgomery, J. Opt. Soc. Amer. 57, 772 (1967).
15. J. Dyson, Proc. Roy. Soc. (London) A248, 93 (1958).
16. J. Goodman, op. cit., p. 60.
17. A. Papoulis, Systems and Transformations with Applications in Optics, McGraw-Hill, 234 (1968).
18. E. Lau, Optik 12, 23 (1955).
19. Product of Edmund Scientific, Barrington, N. J.

## CHAPTER IV

### THE TALBOT SPECTROMETRIC IMAGER

#### Introduction

Of the many instruments that measure the spectrum, Fourier spectroscopes have received considerable attention. This is due mainly to two advantages: the multiplex advantage and the optical acceptance advantage. The latter applies to the Michelson interferometer only and theoretical luminosity gains of 200 over the grating spectrometer have been reported.<sup>1</sup> The multiplex advantage refers to the simultaneous encoding of all wavelengths onto a single detector by assigning each resolution element its own carrier frequency. In this manner a time advantage of great importance is obtained which is used either to decrease the time of observation or to increase the signal-to-noise ratio by time averaging. An example of this time advantage is the planetary spectra of P. Connes and J. Connes obtained with a Michelson interferometer that could have been obtained with a good grating spectrometer in a total time of a few thousand years.<sup>2</sup>

In addition to the Michelson interferometer, various additional schemes for multiplexing a spectrum have been devised. The output of a dispersing spectroscopy such as a prism has been multiplexed in two ways. One method uses a rotating reticle on which a set of concentric annular rings are marked and places it in the exit plane of the spectroscopy.<sup>3</sup> Each annular ring has a different number of equal opaque and transparent sections and encodes a different spectral element. The total light is

gathered and recorded. The other method is to place a stationary mask in the exit plane of the dispersing spectroscopy<sup>4</sup>. The mask has a number of slits that are either opaque or transparent. The light is gathered and recorded, and then a new mask is inserted. The number of resolvable spectral elements equals the number of masks that are used. In order to retrieve the spectrum, the masks are designed so that the recorded intensities can be expressed as a product of a Hadamard matrix and the unknown spectral elements. Recovery is accomplished by a Hadamard transformation which is reportedly five times faster on the computer than the Fast Fourier transform. Of importance in this chapter is the scheme for multiplexing spectra with the Talbot effect.<sup>5</sup> The coding is a cosine transformation of the spectrum as a function of the separation of two gratings. Another cosine transformation recovers the spectrum.

Not only can the spectrum be multiplexed but images, too. An image scanning system that multiplexes a two dimensional scene with a single detector has been proposed.<sup>6</sup> The scene is imaged onto a two dimensional mask that either transmits or blocks light at various points on its surface. The light is gathered and the intensity is recorded. Then this mask is replaced by another mask with different opaque and transparent regions than the previous one, and the intensity is recorded again. If  $m \times n$  elements of the scene are to be encoded then  $m \times n$  masks are prepared and  $m \times n$  intensities recorded. The masks are based on the two dimensional Hadamard matrices and retrieval is accomplished with a Hadamard inverse transformation.

This image scanner was extended to encode the brightness distribution of a scene not only as a function of coordinates  $(\alpha, \beta)$  as above

but also as a function of  $\lambda$  from point to point.<sup>7</sup> This new instrument is called a spectrometric imager. Thus the decoded output of such a system could be a series of scenes in which the intensity at a given  $\lambda$  would be presented. The modification here is to follow the mask of the above image scanning system with a dispersing spectrometer like a prism and then a slotted mask with say  $p$  slits placed in the exit plane of it. The slits would be designed according to the Hadamard matrix again; the light gathered; and the intensity recorded. Here  $m \times n \times p$  elements are encoded which require  $m \times n \times p$  measurements.

The Talbot interferometer follows this kind of development. First there was the spectrometer and now in this chapter we examine the theory of using the effect to make an image scanner and a spectrometric imager. Our theory for the image scanner shows that the spatial distribution of a scene is encoded as a Fourier cosine transform if we restrict the acceptance angle of the instrument. The scene is recovered from the encoded data by a cosine transformation. The Talbot equivalent of a spectrometric imager is a bit more complicated, requiring four gratings if the total Fourier cosine space is to be accessible. The two grating instrument can only explore a conical surface in the Fourier space of  $S(\alpha, \beta, \lambda)$ . The extra set of gratings allows us to explore the whole volume. The theory for the Talbot image scanner and the Talbot spectrometric imager is presented in this chapter. The image scanner is a special case of the spectrometric imager.

## Theory

The basic theory for an image scanner and a spectrometric imager (See Fig. 22) consists of two gratings and resembles the shearing interferometers of Chapter III. It differs in the way we observe the light intensity. The light behind the second grating is collected onto a single detector, and its intensity as a function of grating separation is measured. The second grating has a lateral motion that allows electronic filtering of the encoded data. The combination of lens L1 and a scene in its front focal plane models a distant target such as the sky. Self-images of G1 are formed by the diffracted light waves that originated in the scene, and the light intensity falling on the detector is modulated by the laterally moving G2 with velocity  $v_x$ . We rotate grating G1 and G2 by angle  $\varphi$ , keeping their rulings parallel. In actual practice the scene would be rotated by a dove prism instead of rotating the gratings. The gratings have a transmission function  $g(x) = 1 + \cos(2\pi x/d)$ . Other gratings with more complicated transmission functions like the Ronchi ruling can be used, but they require considerably more data processing.

The scene is spatially and temporally incoherent so that the total intensity at the detector is the sum of the intensities contributed by each point in the scene. Therefore the response of the spectrum to a single point in the front focal plane of L1, called the "point spread response", characterizes the instrument. The total response to any scene is then a weighted sum of point spread responses, where the weight given is equal to the intensity for each point in the scene. The computation of the point spread response of our instrument follows.

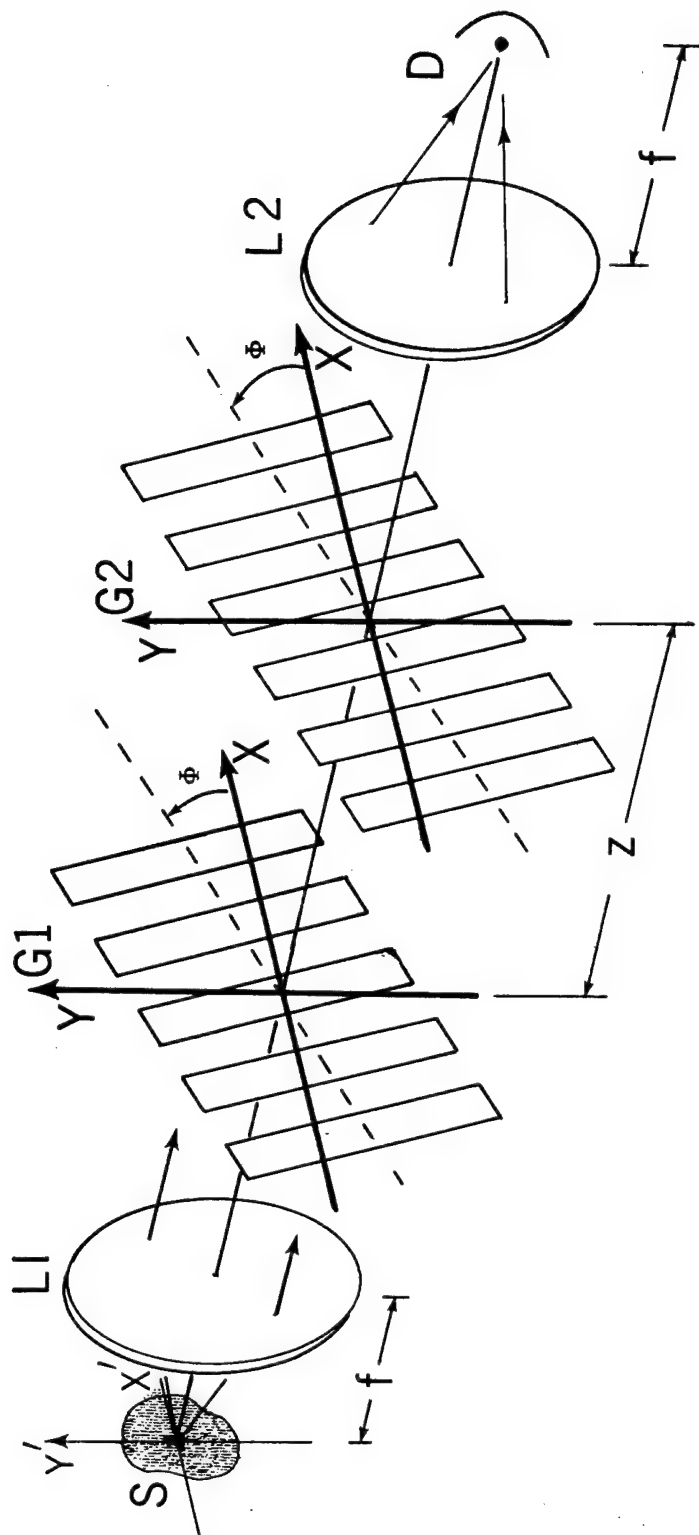


Figure 22. The diagram of the basic Talbot spectrometric imager. Grating  $G2$  moves laterally and longitudinally. Both gratings are rotated.

## Point Spread Response

Let a monochromatic point source of wavelength  $\lambda$  be located at  $(x', y')$  in the front focal plane of L1. Therefore a plane wave with direction cosines  $\alpha \approx -x'/f$ ,  $\beta \approx -y'/f$  and  $\gamma = \sqrt{1 - \alpha^2 - \beta^2}$  will impinge upon G1. Just behind G1 for  $\varphi = 0$  we have

$$u(x, y, 0^+) = \exp\{ik(\alpha x + \beta y)\} [1 + \cos(2\pi x/d)]; \quad k = 2\pi/\lambda.$$

Using a reasoning like Edgar's,<sup>8</sup> the grating diffracts the light so that three plane waves propagate beyond the grating and the field becomes

$$\begin{aligned} u(x, y, z) = & \exp\{ik(\alpha x + \beta y + \gamma z)\} + \\ & \frac{1}{2} \exp\{ik[(\alpha - \lambda/d)x + \beta y + z\sqrt{1 - (\alpha - \lambda/d)^2 - \beta^2}]\} + \\ & \frac{1}{2} \exp\{ik[(\alpha + \lambda/d)x + \beta y + z\sqrt{1 - (\alpha + \lambda/d)^2 - \beta^2}]\}. \end{aligned}$$

Great simplification results when the square root terms are expanded in a power series and only the first three terms are kept. Since the instrument will be operated only in the region  $(\alpha, \beta)$  where the first two terms are significant, only three terms are kept, where the third term will define the restricted region. Therefore,

$$\begin{aligned} \sqrt{1 - (\alpha \pm \lambda/d)^2 - \beta^2} \approx & 1 - \frac{1}{2}(\alpha \pm \lambda/d)^2 - \frac{1}{2}\beta^2 - \\ & \frac{1}{8}[(\alpha \pm \lambda/d)^2 + \beta^2]^2. \end{aligned}$$

Substituting this into our field equation and collecting like terms yield

$$\begin{aligned} u(x, y, z) \approx & \exp\{ik(\alpha x + \beta y + \gamma z)\} \{1 + \exp\{-(i\pi z\lambda/d^2) \\ & (1 - 3\alpha^2/2 - \beta^2/2 - \lambda^2/4d^2)\}\} \\ & \cos\{(2\pi/d) [x - z\alpha(1 + \alpha^2/2 + \beta^2/2 + \lambda^2/2d^2)]\}. \end{aligned}$$



By restricting the size of the source region the propagating field is

$$u(x,y,z) \approx 1 + e^{-i\pi z\lambda/d^2} \cos[2\pi(x - z\alpha)/d], \quad (1)$$

where the overall phase factor is dropped since it is intensity that is detected, and the approximation is valid if  $\pi z\lambda(3\alpha^2 + \beta^2 - \lambda^2/2d^2) \leq \pi/4$  and  $\pi z\alpha(\alpha^2 + \beta^2 + \lambda^2/d^2)/d \leq \pi/4$ . The former condition implies that the useful region  $(\alpha, \beta)$  lies within an ellipse whose major axis coincides with the  $\beta$  axis and is  $\sqrt{3}$  times as large as the minor axis. Since the gratings will be rotated, the region of restriction lies within a circle whose radius is given by the minor axis,  $r = d^2/\lambda z$ . The second condition is less restrictive.

The field behind the second grating is given by the product of the propagating wavefield, eq. (1), and the grating transmission function for G2, which is moving laterally with velocity  $v_x$ . Therefore

$$u(x,y,z^+) \approx \{1 + e^{-i\pi z\lambda/d^2} \cos[2\pi(x - z\alpha)/d]\} \\ \{1 + \cos[2\pi(x - v_x t)/d]\},$$

where  $z^+$  indicates the plane just behind the second grating. The light in this plane is gathered and recorded by a detector whose signal is proportional to the total intensity. Therefore the detected intensity is

$$I_D(z, \alpha) \approx \iint_{\Sigma} |u(x,y,z^+)|^2 dx dy$$

where the interval of integration is over the illuminated region  $\Sigma$ , and the size of the receiver covers all significant diffraction orders.

There are nine terms in this integration. Those terms like

$$\iint_{\Sigma} \cos[2\pi(x - v_x t)/d] dx dy \approx 0. \quad \text{Terms independent of } x \text{ and } y \text{ are not}$$

zero and they give the point spread response of the system as

$$I_D(z, \alpha) \approx 9/4 + 2 \cos(\pi z \lambda / d^2) \cos[2\pi(v_x t - z\alpha)/d] + \frac{1}{8} \cos[4\pi(v_x t - z\alpha)/d], \quad (2)$$

where  $\iint_{\Sigma} dx dy$  is chosen to be 1.

#### Demodulation of the Response

The point spread response of equ. (2) contains a dc term and two time modulated terms. Each modulated term has its own temporal carrier,  $v_x/d$  and  $2v_x/d$ , and they can be filtered either by a computational step or electronically. Therefore the two terms  $\cos(\pi z \lambda / d^2) \cos(2\pi z \alpha / d)$  and  $\cos(4\pi z \lambda / d)$  can be separately treated as point spread responses of a new system that includes a filtering step. The former term contains both  $\lambda$  and  $\alpha$  information whereas the latter has only  $\alpha$ . We select the  $\alpha$  only term for our Talbot image scanner and the other term for the Talbot spectrometric imager. Before considering these two instruments a review of the Talbot spectrometer would be appropriate. The spectrometer selects the term in  $\lambda$ .

#### The Talbot Spectrometer Review

The Talbot spectrometer<sup>5</sup> uses the  $\cos(\pi z \lambda / d^2) \cos(2\pi z \alpha / d)$  term. By restricting the source with a narrow slit so that  $\cos(2\pi z \alpha / d) > 0.7$ , this part of the term can be ignored. Our restriction means that the angular width of the slit is  $\alpha < d/8z$ . The detected intensity is

$$I_D(z) \sim \int S(\lambda) \cos(\pi z \lambda / d^2) d\lambda = \text{Re } \tilde{S}(\rho),$$

where  $\rho = z/2d^2$ ,  $\text{Re}$  means the real part of what follows, and  $\tilde{S}(\rho)$  is the Fourier transform of  $S(\lambda)$ . The spectrum can be recovered by another cosine transformation.

$$\int I_D(\rho) \cos(2\pi\rho\lambda) d\rho = \frac{1}{2} [S(\lambda) + S(-\lambda)].$$

Since we encode only the real part of the Fourier transform the recovered spectrum is even. However  $S(\lambda) = 0$  for  $\lambda < 0$ , and there is no ambiguity in the result.

The resolution of the spectrum is easily calculated by letting  $S(\lambda) = \delta(\lambda - \lambda_0 + \Delta\lambda/2) + \delta(\lambda - \lambda_0 - \Delta\lambda/2)$ . The recorded intensity is

$$\begin{aligned} I_D(z) &\sim \cos[2\pi\rho(\lambda_0 - \Delta\lambda/2)] + \cos[2\pi\rho(\lambda_0 + \Delta\lambda/2)] \\ &= 2 \cos(2\pi\rho\Delta\lambda) \cos(4\pi\rho\lambda_0), \end{aligned}$$

where  $\cos(4\pi\rho\lambda_0)$  is the carrier and  $\cos(2\pi\rho\Delta\lambda)$  is the envelope of the signal. A contrast reduction of 0.7 in  $I_D(z)$  can be detected by the eye and this occurs when  $2\pi\rho\Delta\lambda = \pi/4$ . Solving for  $\Delta\lambda$  we have  $\Delta\lambda = d^2/4z$ . The minimum detectible separation  $\delta\lambda$  occurs for the largest  $z$ . From chapter II the largest  $z$  is  $z_{\text{max}} = Nd^2/2\lambda$ , where  $N$  is the number of grating periods in the illuminated field. Therefore the resolution  $\delta\lambda/\lambda = 1/2N$ . For a sodium doublet  $\lambda_0 = 5893 \text{ \AA}$  and  $\Delta\lambda = 6 \text{ \AA}$  and therefore a grating with at least 500 lines can resolve the doublet. With photoelectric measurement of  $I(S)$  and hence  $\tilde{S}(\rho)$  the resolution will be better since the drop of the envelope will be detectible long before it goes down to 0.7 of its maximum.

## The Talbot Fourier Analyzer

This instrument uses the  $\cos(4\pi z\alpha/d)$  term so that a mask  $M(x'/f, y'/f)$  placed in the front focal plane of lens L1 has a recorded intensity

$$I_D(z) = \iint M(x'/f, y'/f) \cos(4\pi z x'/fd) dx' dy',$$

where the interval of integration is  $(-\infty, +\infty)$  and  $\alpha \approx -x'/f$ ,  $\beta \approx -y'/f$ . If a real function  $g(x'/f)$  is to be analyzed, then we make a function mask such that  $M(x'/f, y'/f) = 1$  for  $0 \leq x'/f \leq Q$ ,  $0 \leq y'/f \leq g(x'/f)$ , and zero otherwise, where  $Q$  includes the entire range of  $g(x'/f)$ . The size of the mask is limited to the region where our simplified point spread response is valid. Consequently,

$$\begin{aligned} I_D(z) &\sim \iint M(x'/f, y'/f) \cos(4\pi z x'/fd) dx' dy' \\ &= \int_0^Q \int_0^{g(x'/f)} dy' \cos(4\pi z x'/fd) dx' \\ &= \int_0^Q g(x'/f) \cos(4\pi z x'/fd) dx' = \text{Re } \tilde{f}(v), \end{aligned}$$

where  $v = 2z/fd$ .

Since only positive values of  $g(x'/f)$  can be simulated with our mask, functions with negative values cannot be directly encoded. A positive constant value is added to the function so that it is everywhere positive. Knowing the result in the transform domain of adding a constant to a function, this bias can be subtracted from the final output.

## The Talbot Image Scanner

### Theory

Let  $S(\alpha, \beta)$  be the brightness of a scene as a function of its angular coordinates  $(\alpha, \beta)$  and filter out the  $\cos(4\pi z\alpha/d)$  term of the point spread response. The recorded intensity will be

$$I_D(z) = \iint S(\alpha, \beta) \cos(4\pi z\alpha/d) d\alpha d\beta = \text{Re } \tilde{S}(v, 0) \quad (3)$$

where

$$\tilde{S}(v, \mu) = \iint S(\alpha, \beta) \exp\{2\pi i(v\alpha + \mu\beta)\} d\alpha d\beta$$

is the two dimensional Fourier transform of  $S(\alpha, \beta)$ ,  $v = z/2d$  radians<sup>-1</sup>.

The recorded signal is a special case of the two dimensional Fourier cosine transformation and explores a single straight line in this space. The highest recorded frequency is given by the greatest separation between the gratings which cannot exceed  $z_{\max} = Nd^2/2\lambda$ , where  $N$  is the number of grating periods. Another straight line can be explored in the transform space by tilting both  $G1$  and  $G2$  by  $\varphi$ . Because of this tilt equ. (3) takes on new coordinates  $\alpha', \beta', v', \mu'$  where  $\alpha' = \alpha \cos \varphi + \beta \sin \varphi$ ,  $\beta' = -\alpha \sin \varphi + \beta \cos \varphi$ ,  $v' = v \cos \varphi + \mu \sin \varphi$  and  $\mu' = 0$ . Equation (3) becomes

$$I_D(z, \varphi) = \iint S(\alpha', \beta') \cos(2\pi v' \alpha') d\alpha' d\beta' = \text{Re } \tilde{S}(v', 0),$$

where  $v'$  is a straight line in the transform space  $(v, \mu)$  tilted by an angle  $\varphi$ . This is sketched in Fig. 23.

Thus the total transform space is accessible to the image scanner for encoding. The grating separation  $z$  determines the magnitude of the

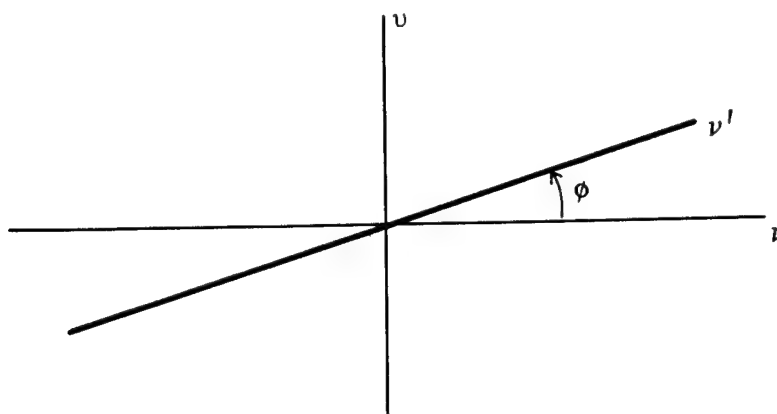


Figure 23. The transform space for tilted gratings. The recorded signal gives us the value of the cosine transformation on the  $\nu'$  axis that tilts with the gratings. Therefore the entire transform space can be sampled.

frequency in the transform plane that we are encoding the tilt of the gratings gives us its orientation so that the coordinates of  $\tilde{S}(\nu, \mu)$  are given by  $\nu = \nu' \cos \varphi$  and  $\mu = \nu' \sin \varphi$ . For the straight line sampling the gratings are rotated by  $\Delta\varphi$  and then the gratings are separated from zero to  $z_{\max}$ . The gratings are rotated by another  $\Delta\varphi$  and then separated again. This is repeated and in this manner the transform domain is sampled along straight lines that look like a collection of spikes.

Another way to sample the transform space is by incrementing the separation of the gratings by some fixed distance  $\Delta z$  and rotating them through one revolution. Then they are separated by another  $\Delta z$  and once more rotated. The sequence is continued until  $z_{\max}$  is reached. In this way the transform space is sampled in regions that form a set of equally spaced concentric circles.

A third way to sample the transform space is to separate the gratings continuously while rotating them so that the transform is sampled on a spiral. The shape of the spiral depends upon the relative motions between rotation and separation. A spiral with many revolutions occurs

if we rotate many times as we separate the gratings. This situation is approximately the same as the concentric circle case. A sequence of spirals that do not complete one revolution can be made by separating the gratings through the maximum extent for a small rotation that is but a fraction of one revolution. The next spiral is generated through separating the gratings again, and so forth. A sequence of spirals that look like spikes is obtained. Sampling in the Fourier domain means that our recovered image will be replicated. If the sampling is sufficiently dense then the total transform is known through interpolation in a way analogous to the dimensional sampling theorem in cartesian coordinates. In this way the image can be recovered. Work by Barakat<sup>9</sup> can be used for the circular sampling case and that by Bracewell<sup>10</sup> for the straight line sampling. Unfortunately the formulation does not lend itself to the Fast Fourier transform for which the sampling points should be on a rectangular array.

A less efficient way of scanning the transform domain is to program  $z$  and  $\varphi$  motions so that the scan travels along lines that are parallel to the  $v$  or  $\mu$  coordinate. This is accomplished by holding a constant value of say  $v_0$  or  $\mu_0$  depending upon the scan desired, so that  $v_0 = z(t) \cos \varphi(t)$  and  $\mu_0 = z(t) \sin \varphi(t)$ , where  $z(t) = z_0 + v_z t$  and  $\varphi(t) = \varphi_0 + \omega t$ ,  $v_z$  is the longitudinal velocity of G2,  $\omega$  is the angular velocity of the gratings and  $z_0, \varphi_0$  is the initial polar coordinate from which the scan begins. In this way the Fourier domain is scanned in a rectangular array and the Fast Fourier transform can be used to recover the image.

## Special Cases

In this section we discuss special scenes which can be handled simply without the need for sampling the transform domain. Consider an object that contains a number of straight lines as shown in Fig. 24.

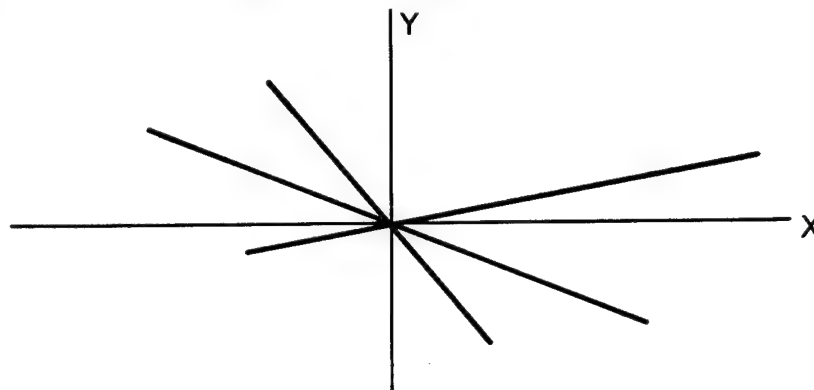


Figure 24. Spike scene. This scene can be easily deduced by the instrument, as explained in the text.

The Talbot image scanner can be operated in the following mode to detect the orientation of each spike. Position G2 in one of the self-image planes of G1. G2 need not be moved laterally but can instead be tilted slightly with respect to G1 so that moiré fringes will be observed if there is a self-image of G1 at G2. If this shift exceeds  $d/4$  then the sum of the self-images produce a relatively constant illumination.

Therefore no self-images are formed. This situation occurs when the line source is not parallel to the rulings. By observing the contrast of the moiré fringes as the gratings are rotated the orientation of each line source can be determined. From Appendix 1, the source requirement is  $\alpha < d/4z$ . If the gratings are separated by  $z_{\max} = Nd^2/2\lambda$  then the smallest deviation  $\delta\alpha$  will be  $\delta\alpha < \lambda/2Nd$ . To convert this to accuracy in rotation  $\delta\varphi$ , let  $L$  be the length of the source; then  $\delta\varphi \approx \delta\alpha/L = \lambda/2NdL$ , for small angle approximation.



Another special object would be a uniformly bright scene such as a mountain range at a far distance or a cloud mass of smog. We use the Fourier analyzer mode of the image scanner, and what we decode later on gives us the profile of the mountain range. If it is not uniformly illuminated, then what is recovered is the effective profile. This silhouette example is mathematically equivalent to the mask case discussed previously in the Fourier analyzer section.

For a scene  $S(\alpha, \beta) = S_1(\alpha) S_2(\beta)$  where the function is separable as for example across one dimensional gratings, only two measurements are required. The first measurement is made with  $\varphi = 0$  and the gratings are separated. Then the gratings are tilted to  $\varphi = \pi/2$  and the measurement repeated. We have for  $\varphi = 0$

$$\int S_2(\beta) d\beta \int S_1(\alpha) \cos(2\pi\nu\alpha) d\alpha = C_2 \operatorname{Re} \tilde{S}_1(\nu)$$

and for  $\varphi = \pi/2$

$$\int S_1(\alpha) d\alpha \int S_2(\beta) \cos(2\pi\nu\beta) d\beta = C_1 \operatorname{Re} \tilde{S}_2(\mu),$$

where  $C_1 = \operatorname{Re} \tilde{S}_1(0)$  and  $C_2 = \operatorname{Re} \tilde{S}_2(0)$ . Hence  $C_2 \operatorname{Re} \tilde{S}_1(0) = C_2 C_1$  and we can use this to get  $\operatorname{Re} \tilde{S}_1(\nu)/C_1$  and  $\operatorname{Re} \tilde{S}_2(\nu)/C_2$ . The two dimensional cosine transform is  $\operatorname{Re} \tilde{S}(\nu, \mu) = \operatorname{Re} \tilde{S}_1(\nu) \operatorname{Re} \tilde{S}_2(\mu)$ . Taking the inverse of this recovers the scene.

## The Talbot Spectrometric Imager

The Talbot spectrometric imager uses the  $\cos(\pi z \lambda / d^2) \cos(2\pi z \alpha / d)$  term that is filtered from the point spread response. Therefore for a one dimensional scene whose brightness is given by  $S(\alpha, \lambda)$  the detected intensity is

$$I_D(z) \sim \iint S(\alpha, \lambda) \cos(\pi z \lambda / d^2) \cos(2\pi z \alpha / d) d\alpha d\lambda.$$

In order to have the same units for the brightness variable we substitute  $\alpha \sim x/f$  in our equation. Expanding the trigonometric function yields

$$\begin{aligned} I_D(z) &\sim \iint S(x, \lambda) \{ \cos[2\pi(\rho\lambda + vx)] + \cos[2\pi(\rho\lambda - vx)] \} dx d\lambda \\ &= \text{Re } \tilde{S}(\rho, v) + \text{Re } \tilde{S}(\rho, -v) \end{aligned} \quad (4)$$

where  $\tilde{S}(\rho, v)$  is the two dimensional Fourier transform of  $S(x, y)$ ,  $\rho = z/2d^2$ ,  $v = z/fd$ . Since  $v = 2\rho d/f$ , the complete two dimensional cosine transform is not encoded as a function of  $z$  but rather only on a straight line that makes an angle  $\theta = \arctan(f/2d)$  with the  $v$  axis, as shown in Figure 25. In order to sample the whole transform space, the ratio  $f/2d$  must be varied. This can be accomplished by having a zoom lens arrange-

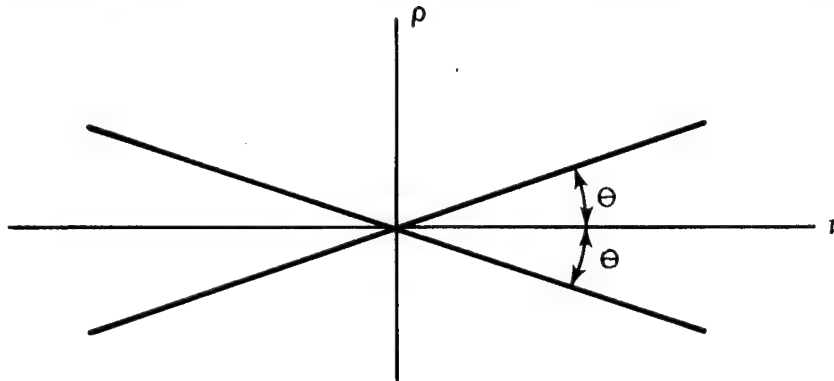


Figure 25. Sampling in the cosine transform space  $S(\alpha, \lambda)$ . The sampling is along the double lines which form an angle  $\theta = \pm \arctan(f/2d)$ .

ment or by having gratings with variable pitch. This latter arrangement will be mentioned later.

These arguments are easily extended to the most general scene  $S(x,y,\lambda)$ . For this scene we rotate the gratings as we did for the image scanner. Therefore variables in the new coordinate system become  $\alpha' = \alpha \cos \varphi + \beta \sin \varphi$ ,  $\beta' = \beta \cos \varphi - \alpha \sin \varphi$ ,  $v' = v \cos \varphi + \mu \sin \varphi$ , and  $\mu' = 0$ ; eq. (4) becomes

$$\begin{aligned} I_D(z) &\sim \iint S(x,y,\lambda) \cos\{2\pi[\rho\lambda \pm v'(x \cos \varphi + y \sin \varphi)]\} dx dy d\lambda \\ &= \operatorname{Re} \tilde{S}(v', 0, \rho) + \operatorname{Re} \tilde{S}(-v', 0, \rho), \end{aligned}$$

where  $v'$ ,  $\rho$  are interdependent,  $v = v' \cos \varphi$ , and  $\mu = \mu' \sin \varphi$ .

Because of the interdependence our scan explores straight lines in the three dimensional transform domain. These lines go through the origin. By varying  $\varphi$  other such lines can be explored. The accessible lines together form a two sided cone with its center at the origin. The angle of the cone is given by  $\arctan(2d/f)$ . In order to scan the whole volume the cone angle must be varied. This is accomplished by changing  $f$  as with a zoom lens or by using variable pitch gratings.

A variable pitch grating can be synthesized with two Ronchi rulings in contact with each other so that moiré fringes are formed. The period  $p$  of the moiré fringes is given by  $p = d/2 \sin(\psi/2)$ , where  $\psi$  is the angle at which the rulings meet and  $d$  is the period of the Ronchi rulings. Using the moiré fringes for  $G1$  and  $G2$  of our instrument we can vary the period by changing the angle  $\psi$ . In this way the total volume can be measured. This solution means a loss of light through the instrument because four gratings are used instead of two. Therefore only one-

sixteenth of the light intensity at the entrance of the instrument reaches the detector instead of one-fourth with two gratings. This loss of light makes this a dubious solution. One alternative is to use one amplitude grating and one phase grating to obtain the moiré fringes. In this way the light throughput of this instrument is unaltered.

A great number of scanning schemes can be imagined in three dimensions. One would be a series of spikes pointing in all directions. Another would be a three dimensional spiral like the winding of a ball of string. The exact scanning scheme has not been worked out for the Talbot spectrometric imager.

#### References for Chapter IV

1. G. Vanasse and H. Sakai, Progress in Optics Vol. VI, ed. E. Wolf, North-Holland, 307 (1967).
2. P. Jacquinot, Appl. Opt. 8, 497 (1969).
3. J. Grainger, J. Ring and J. Steel, J. De Phys. Colloq. C2, 2 (1967).
4. R. Ibbett, D. Aspinall and J. Grainger, Appl. Opt. 7, 1089 (1968).
5. A. Lohmann, Proc. Conf. Opt. Instruments and Techniques, 1961, London, Chapman and Hall, 1962, p. 58.
6. J. Decker, Appl. Opt. 9, 1392 (1970).
7. M. Harwit, Appl. Opt. 10, 1415 (1971).
8. R. F. Edgar, Optica Acta 16, 281 (1969).
9. R. Barakat, J. Opt. Soc. Amer. 54, 920 (1964).
10. R. Bracewell, Austr. J. Phys. 9, 198 (1956).

## CHAPTER V

### CONCLUSIONS

#### Summary of Results

A number of instruments have been proposed in this report together with their theoretical analysis. Experimental evidence for the two shearing interferometers and the autocollimator has been presented. These results show that the Talbot effect can be successfully employed in the design of new optical instruments. In particular we mention the adaptation of our constant radial shearing interferometer by a large eyeglass manufacturer for the testing of their new multifocal lenses.

At the outset we pointed out the advantages of the Talbot effect in the design of new instruments. These advantages were borne out during the course of the work. Their low cost and their insensitivity to poor quality gratings is particularly gratifying. Our first experiment used gratings that were severely scratched without materially altering the performance of the instrument. The Ronchi rulings could be purchased for as little as \$3.00 per square inch (250 lines/inch) for sizes up to 2" x 2"<sup>1</sup>, and \$9.00 per sq in. (300 lin/in) for sizes up to 80" x 80"<sup>2</sup>. What continually amazed visitors about our demonstrations was the ease with which the setup could be adjusted. The entire interferometer could be assembled and adjusted within fifteen minutes. This is due to two factors: (1) The scale of the experiment is in units of the self-image interval which was about 3 cm in our experiments. This is a convenient distance for an experimentalist to handle since it does not require micropositioning nor an enormously large laboratory.

(2) The self-image distance is dependent upon the grating period. If the gratings are inadvertently tilted, then the effective grating period is reduced by only a cosine factor. Thus small error angles of as much as five degrees were tolerable.

The Talbot shearing interferometers measure both the radial and lateral phase derivative of the wavefront under test by using either a circular grating or a Ronchi ruling respectively. With simple binary filters either triple or double shearing interferences could be obtained. These interferences become the second and first derivatives respectively if the shear introduced is less than the width of the tiniest details in the object. The amount of shear introduced depends upon the distance that the object is placed from the second grating as well as the diffraction angle. This affords a great range in sensitivity. Maximum contrast in the interferogram is obtained by placing the second grating in the self-image of the first. Small deviations from this position only affect the contrast by a cosine factor. Therefore positioning of the gratings was not critical, making this instrument very simple to set up. Used like a Schlieren setup, the interferometer can study the flow of hot gases. Beautiful color effects may be introduced to give additional information. The autocollimator is a special case of the Talbot interferometer. It tests the curvature of the wave at the first grating which can be related to the amount of defocussing of the collimating objective. With photoelectric measurement the sensitivity of the instrument can be increased by about two orders of magnitude.

The theory of the image scanner has been presented, and special objects investigated. The output of the instrument gives a single

point in the Fourier cosine transform space of the scene. By rotating the instrument and separating the two gratings this point can be shifted and the domain scanned. Several scanning schemes are discussed. The Fourier analyzer is a special case of this instrument. The instrument is not rotated and the scene is replaced by a function mask in the front focal plane of the collimator. The preparation of the function mask was described. By separating the gratings the cosine transformation of the function is measured.

A theoretical study of the spectrometric imager is presented. The output is a Fourier cosine transform of the scene as a function of its angular coordinates and wavelength. The output is a single point in the three dimensional Fourier cosine transform space for each angular orientation of the instrument and the grating separation. With two gratings only, a surface in the three dimensional transform space can be scanned. To scan the complete volume, the system must be modified by including a zoom lens or by using variable pitch gratings. The variable pitch grating can be synthesized by using the moiré effect between two Ronchi rulings.

#### Suggestions for Further Study

It is the nature of research that one is never completely done with his task. Another question lurks in the shadows ready to replace a question recently disposed. In the following paragraphs are discussions in the nature of unfinished business and some side adventures.

The maximum sensitivity of the Talbot instruments is limited by the maximum distance over which the Talbot images occur. This distance

is given in Chapter II as  $z_{MAX} = Bd/2\lambda$ , where  $B$  is the width of the grating,  $d$  is the grating period and  $\lambda$  is the wavelength of the light. A Talbot image is formed by the interference of the diffracted orders with the zeroth order. These interferences occur until the diffracted orders walk off the zeroth order. With the addition of two mirrors placed alongside the zeroth order, the diffracted orders are reflected back into the zeroth order thereby increasing  $z_{MAX}$  by the length of the mirror. The mirror requirements should be relatively low since they are used at a grazing incidence of the order of the diffracted angle (about  $10^{-3}$  radians for our experiments). Therefore experiments should be conducted to test this idea. It would also be useful to examine whether a number of smaller mirrors could replace a single large mirror to extend  $z_{MAX}$ .

Another interesting experiment suggested by A. Lohmann is to use a prism prior to the first grating of the lateral shearing interferometer. White light is used as a source, and the prism diffracts the light into its various colors. Since each wavelength enters the first grating at a different angle, the self-images for each color will be shifted. This modified scheme has the advantage of tainting the positive from the negative derivative differently since the setup is no longer symmetric.

The Fourier analyzer, image scanner, and spectrometric imager should be constructed and checked experimentally for feasibility. It would be best to build them in this order since experimental experience from one can be used in the construction of the next. Theoretical studies of the efficiency for various scanning schemes on the latter two instruments should be done so that an optimum data collection scheme can



be programmed. My guess is that the spiral scan is the most efficient way of operating the instruments; however, recovery of the scene from this type of scan would have to be developed. Schemes for presenting the scene as a function of its three parameters, two position coordinates was wavelength, should be studied. A solution would be to use a two dimensional imaging device such as a TV screen and use color to present the third parameter.

In conclusion we can say that our goal has been partially accomplished. We set out to measure the distribution of radiation  $S(\alpha, \beta, \lambda)$  as a function of its angular coordinates and wavelength. Simple experiments were attempted at first dealing with  $S(\alpha)$ . From these studies we learned the critical parameters of the instrument that we choose. In particular we found that collimation and good quality substrates for our gratings were important. These discoveries pointed the way to the invention of a new autocollimator and two new shearing interferometers. Our final step was to complete the theory for an instrument that would measure the total distribution  $S(\alpha, \beta, \lambda)$ .

#### References for Chapter V

1. Edmund Scientific Co., Barrington, New Jersey
2. Max Levy Co., Inc., Philadelphia, Pa.

## AN INTERFEROMETER BASED ON THE TALBOT EFFECT

A. W. LOHMANN and D. E. SILVA

*Department of Applied Physics and Information Science,  
University of California, San Diego, La Jolla, California 92037, USA*

Received 28 December 1970

The moiré effect is very sensitive in detecting small differences between two similar gratings. These differences might be caused by an object with phase gradient placed between the two gratings. The performance of such an instrument can be understood in terms of the "Talbot effect" (also called "Fourier imaging" or "self-imaging"). Slight modifications provide shearing interferences and the second derivative of the object.

The moiré effect reveals very small imperfections of two gratings placed on top of each other. Lord Rayleigh used this effect for testing diffraction gratings. The same basic idea has been used for many other purposes. For example, in electron microscopy the imperfections in two pieces of crystal lattice can be made visible in this way [1]. Essentially the same moiré effect is utilized for studying the shape of a diffusely reflecting surface, when the shadow of a grating falls onto that surface. The grating shadow is observed through the same grating [2]. Also the shape of a refracting object can be investigated by means of the moiré effect [3]. The refracting object is placed before or behind a first grating (fig. 1). The shadow of the first grating will be deformed due to the refractive gradient. The moiré fringes observed behind the second grating placed at a distance  $z$  from the object are lines of equal deviation [eq. (1)].

$$\epsilon_x(x, y) = md/z; \quad m = 0, \pm 1, \pm 2 \dots (1)$$

We intend to extend this method of observing refractive gradients by means of moiré. As described so far this method is based entirely on rays. This point of view is not satisfactory since it is known that wave optical color effects occur when white light passes through two gratings at a finite distance. This happens with uncollimated [4] and with collimated light [5]. Such color effects may well prove to be useful. A more important objection against the ray-optical point of view is the inability to explain the fundamental limitation of this method. Based on eq. (1), one might suspect that an arbitrarily small deflection angle can be detected if only the distance  $z$  of the two gratings is sufficiently large. Since such unlimited detectability is never attainable

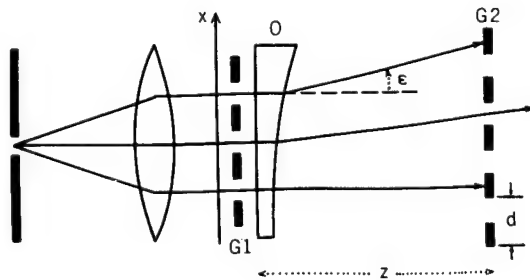


Fig. 1. The Talbot interferometer. G1, G2 gratings with period  $d$ ; ray deflection angle  $\epsilon$  in object O.

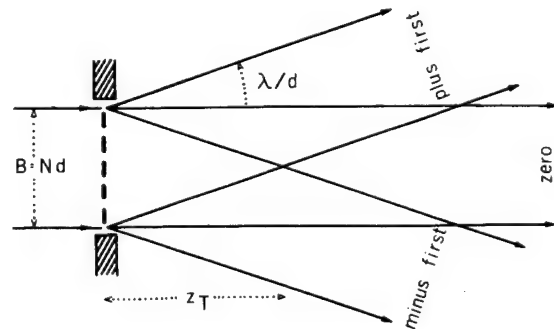
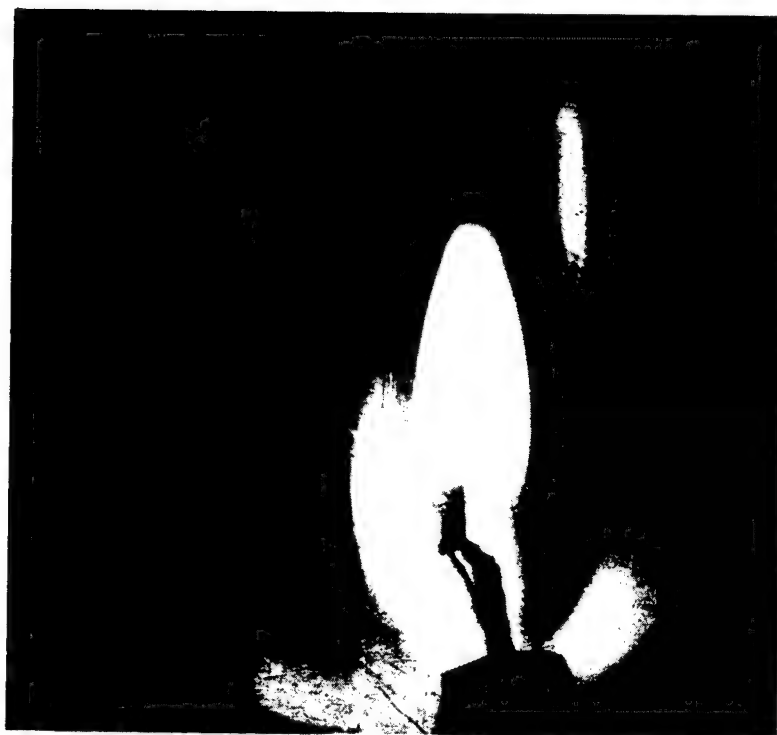


Fig. 2. Overlapping diffraction orders behind a grating of finite width  $B = Nd$ .



(a)



(b)

Fig. 3. Talbot interferences with a candle flame as object between the two gratings. a. Gratings parallel. b. One grating slightly rotated.

one might try to patch on the following wave-optical argument.

The light passing through a grating slit of width  $d/2$  does not behave like a ray anymore after it has travelled over a distance  $z_R$  where the diffraction spread  $z_R\lambda/(d/2)$  equals the slit width  $d/2$  [eq. (2)].

$$z_R\lambda/(d/2) = d/2 ; \quad z_R = d^2/4\lambda . \quad (2)$$

Based on this criterion one might expect  $\epsilon_R$  to be the smallest detectable deflection [eq. (3)].

$$\epsilon_R = d/2z_R = 2\lambda/d . \quad (3)$$

With  $\lambda = 0.5 \times 10^{-3}$  mm and  $d = 10^{-1}$  this leads to  $\epsilon_R = 10^{-2}$ , which is only moderately good.

Fortunately the method is capable of detecting angles much smaller than  $\epsilon_R$  [eq. (3)]. This is due to the Talbot effect [6], which is also known as "Fourier imaging" [7] and "self-imaging" [8]. Talbot discovered about 135 years ago that images can be formed without any lenses or mirrors if the object is a grating which is illuminated in collimated monochromatic light. These "Talbot images" occur at distances  $2d^2/\lambda$ ,  $4d^2/\lambda$ , etc. behind the grating. When a second grating at a slight angular rotation to G1 is placed into the plane of a Talbot image, moiré fringes of high contrast are observed. These moiré fringes will be deformed if a refractive phase object is placed for example close to the first grating. As before these moiré fringes indicate lines of equal deflection by the object [eq. (1)].

The largest possible distance  $z_T$  (or maybe  $2z_T$ ) depends on the finite width  $B = Nd$  of the first grating. At  $z_T$  the first grating diffraction orders have moved to both sides by half of the grating width  $B$  [fig. 2; eq. (4)].

$$z_T\lambda/d = B/2 = Nd/2 ; \quad z_T = Nd^2/2\lambda . \quad (4)$$

When the two gratings are separated by  $z_T$  the smallest detectable deflection  $\epsilon_T$  is now smaller by a factor  $2N$ , where  $N$  is the number of periods in the first grating [eq. (5)].

$$\epsilon_T = d/2z_T = \lambda/Nd = \lambda/B = \epsilon_R/2N . \quad (5)$$

We have performed some experiments with this "Talbot interferometer" as shown in fig. 1. In fig. 3a the object is a flame, and again in

fig. 3b, but now with the second grating slightly rotated around the optical axis. In some additional experiments we have placed a telecentric lens system behind the Talbot interferometer. When introducing a spatial filter into this telecentric system and rejecting everything but the zeroth diffraction order from the two-grating system one observes in essence the second derivative  $\partial^2 u/\partial x^2$  of the object  $u(x, y)$ . When shifting the spatial filter to one of the first grating diffraction orders the image represents shearing interferences  $u(x + \lambda z/d, y) - u(x, y)$ . In a white light one obtains beautiful color fringes which are unlike ordinary interference fringes. For example for a specific grating distance the image contains many blue-orange fringes. These color fringes are of such high contrast that E. Lau found a similar setup useful in designing tablecloths [9]. Our method is also applicable for the detection of small differences between two quite irregular but similar objects. One begins by recording photographically the fringes from the first object. After development the photograph is placed where the fringes had been observed. The first object is now replaced by the second object, which might actually be the first object but somewhat deformed. The moiré fringes between subsequently produced Talbot interference fringes will reveal small differences between the two objects. The quantitative evaluation is similar to that for Lau's dupligran method [10] and for life-fringe holographic interferometry.

## REFERENCES

- [1] J. W. Menter, *Advan. Phys.* 7 (1958) 299.
- [2] H. Takasaki, *Appl. Opt.* 9 (1970) 1467.
- [3] Y. Nishijima and G. Oster, *J. Opt. Soc. Am.* 54 (1964) 1.
- [4] E. Lau, *Ann. Physik* (6), 2 (1948) 417.
- [5] A. Lohmann, *Proc. ICO Conf. Opt. Instr.*, ed. K. J. Habbell (London, 1961) p. 58.
- [6] F. Talbot, *Phil. Mag.* 9 (1836) 401.
- [7] J. M. Cowley and A. F. Moodie, *Proc. Phys. Soc. (London)* B70 (1957) 486, 497, 505; B76 (1960) 378.
- [8] W. D. Montgomery, *J. Opt. Soc. Am.* 58 (1968) 1112.
- [9] E. Lau, *Wiss. Ann.* 1 (1952) 43.
- [10] E. Lau, *Optik* 12 (1955) 23.

## A TALBOT INTERFEROMETER WITH CIRCULAR GRATINGS

A. W. LOHMANN and D. E. SILVA

*Department of Applied Physics and Information Science, University of California, San Diego,  
La Jolla, California 92037, USA*

Received 9 December 1971

The linear gratings in our Talbot interferometer are replaced by circular gratings. This new radial shearing interferometer is sensitive to the radial gradient of the object.

Talbot [1] discovered in 1836 that images of a grating can be formed without any lens or mirror. When illuminated by a monochromatic plane wave the grating will be imaged at distances  $2d^2/\lambda$ ,  $4d^2/\lambda$ , etc. ( $d$  = grating constant). Recently this Talbot effect has been used for interferometry [2]. A second identical grating is placed into one of the "Talbot-planes" of the first grating. The phase object under investigation is situated between the two gratings. The image consists essentially of two shifted object wavefronts or of the first derivative  $\partial u(x,y)/\partial x$  of the object  $u(x,y)$ .

For some objects the radial derivative  $\partial u(r,\varphi)/\partial r$  is more indicative than the linear derivative  $\partial u/\partial x$ . We obtain this radial gradient by replacing the linear gratings by radial gratings as shown in fig. 1. Our radial gratings are from a moiré kit\* with a radius step of 0.25 mm after

photographic reduction. The interference image of a bifocal glass is shown in fig. 2. The interference fringes degenerate into spikes (actually stretched hyperbolas) when the two circular gratings are not laterally aligned. These spikes assume characteristic shapes when a phase object such as a candle is introduced (fig. 3).

There are some remaining questions, which we intend to answer in a more elaborate paper in "Applied Optics". For example, when this circular Talbot interferometer is to be used for quantitative investigations one has to study how well the circular grating really produces "self-images" [3]. In connection with a spatial filter in plane F of fig. 1 this interferometer can also produce the second derivative  $\partial^2 u/\partial r^2$ . Or it

\* Product of Edmund Scientific, Barrington, N.J.

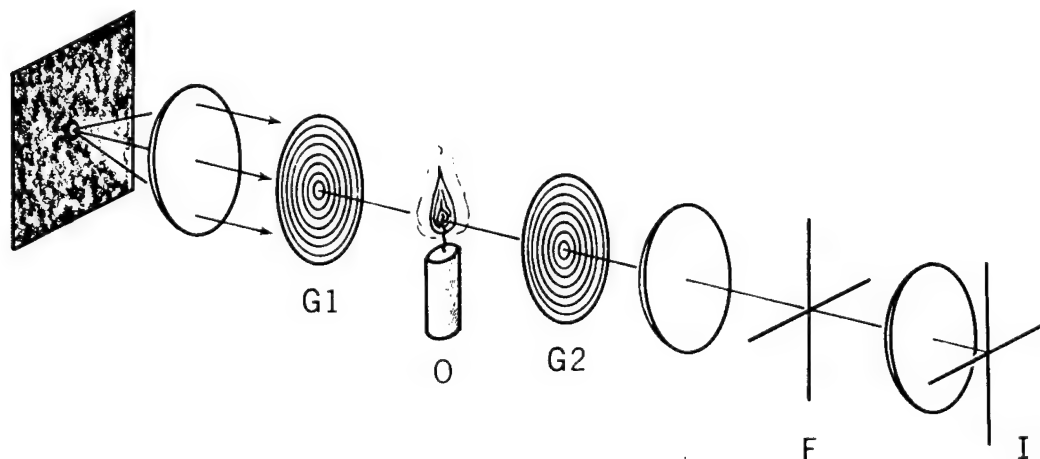


Fig. 1. Talbot interferometer with radial gratings. Object O, gratings G1 and G2, filter plane F, image plane I.

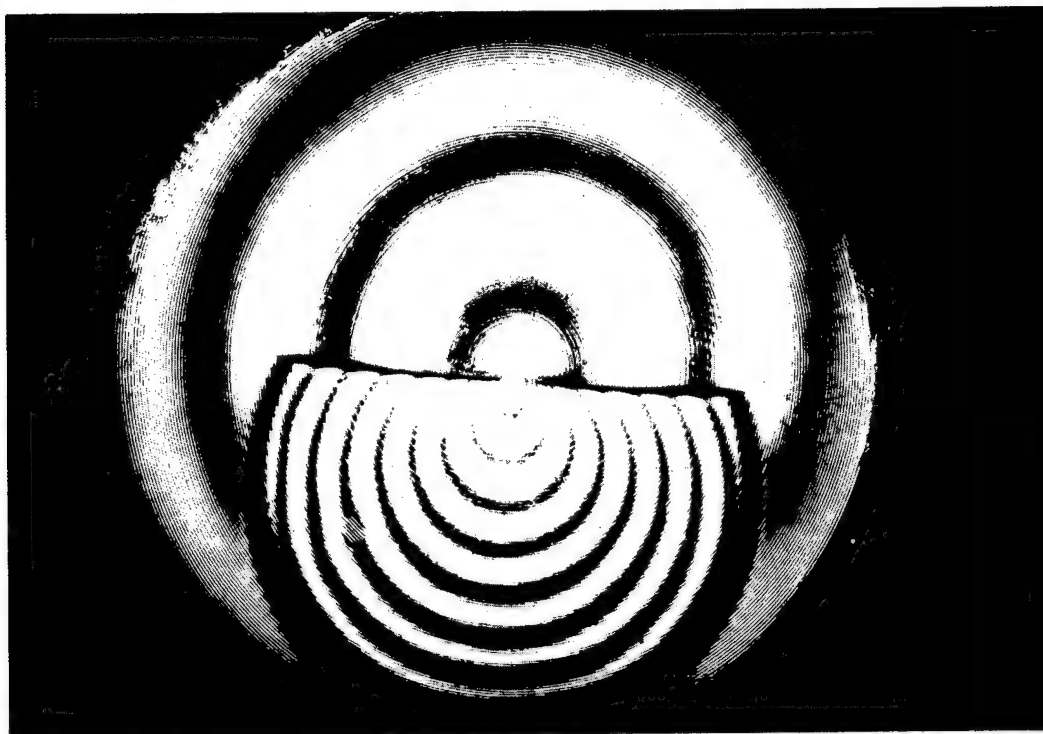


Fig. 2. Interference image of a bifocal eyeglass. The gratings G1 and G2 are centered.

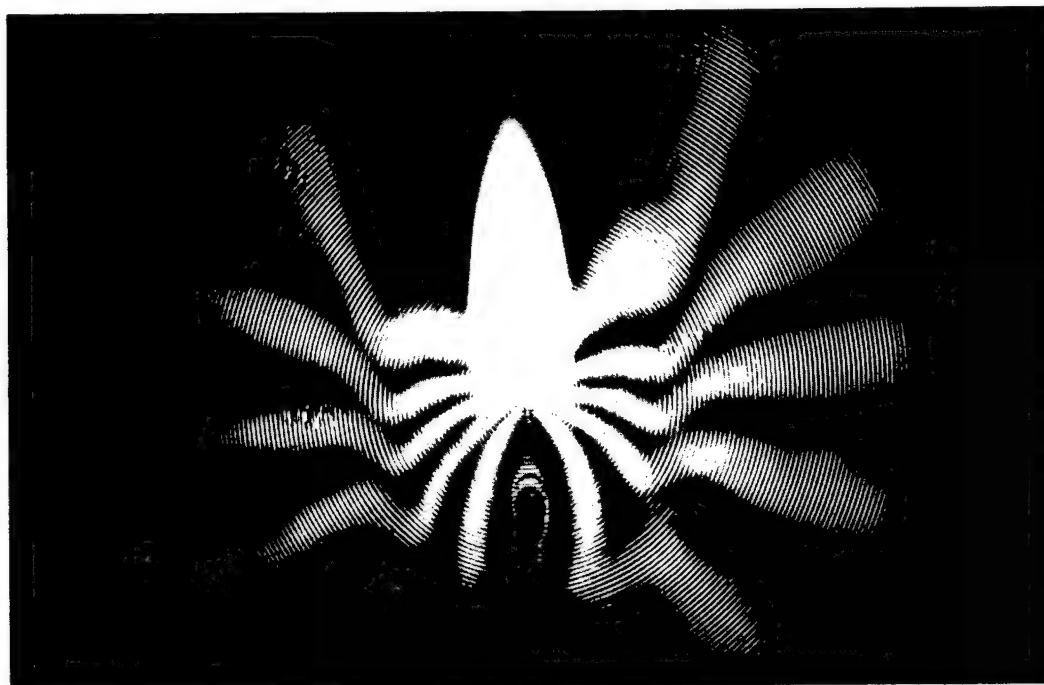


Fig. 3. Interference image of a candle. The two gratings are not centered.

can be used as a shearing interferometer with constant (but adjustable) radial displacement [4].

#### REFERENCES

We thank L. Stotts, who helped on some of the experiments and we acknowledge support from AFCRL Contract F-19628-69-C-0268.

- [1] F. Talbot, *Phil. Mag.* 9 (1836) 401.
- [2] A. W. Lohmann and D. E. Silva, *Opt. Commun.* 2 (1971) 413;  
S. Yokozeki and T. Suzuki, *Appl. Opt.* 10 (1971) 1575;  
S. Yokozeki and T. Suzuki, *Appl. Opt.* 10 (1971) 1690;  
D. E. Silva, *Appl. Opt.* 10 (1971) 1980.
- [3] W. D. Montgomery, *J. Opt. Soc. Am.* 58 (1968) 1112.
- [4] O. Bryngdahl, *J. Opt. Soc. Am.* 61 (1971) 169.

### PAPER 3

## A Simple Interferometric Method of Beam Collimation

D. E. Silva

Department of Applied Physics and Information Science,  
UCSD, La Jolla, California 92037.

Received 12 April 1971.

There are two common methods of determining the degree of collimation: autocollimation and shearing interferometry. The simplest method is the autocollimation technique, but it only indicates collimation by comparing the size of the source with its image. On the other hand the spacing of the fringes in shearing interferometry is a direct measure of the degree of collimation.<sup>1</sup> Recently, Langenbeck derived a method that used

two tiny corner-cube reflectors to sample the beam. In this fashion he was able to translate the measurement from fringe spacing to fringe rotation, with the result of increased sensitivity.<sup>2</sup> The method presented here is an application of the Talbot interferometer<sup>3</sup> and has the same limitations as the other interferometric techniques. The main advantages of this technique are the inexpensive components (two Ronchi rulings) and the relative insensitivity to component alignment.

As Talbot observed in 1837, an image of a grating appears at integral multiples of the distance  $2d^2/\lambda$  (where  $d$  is the grating period) when the grating is illuminated by a plane monochromatic wave. A Ronchi ruling would therefore be imaged at  $2d^2/\lambda$ ,  $4d^2/\lambda$ , etc. If we place another identical Ronchi ruling in one of these self-image planes (see Fig. 1) moiré fringes will be formed, as observed by J. Burch.<sup>4</sup> The fringe spacing  $P$  can be calculated by using the vector diagrams described by Rogers<sup>5</sup> to be

$$P = d/2 \sin(\theta/2), \quad (1)$$

where  $\theta$  is the angle with which the two gratings meet. As the grating G2 is rotated around the optical axis, the fringe spacing increases until we have uniform brightness (or darkness) when grating bars of G1 and G2 are parallel to each other.

The plane wave that illuminates G1 of the interferometer is obtained by placing a point source at the focus of a lens as shown in Fig. 1. When this lens is defocused, the plane monochromatic wave becomes spherical. Cowley and Moodie<sup>6</sup> have shown that the positions of the self-image planes of a grating illuminated by a spherical wave are given by

$$1/Z_J + 1/Z_W = 1/2JZ_T, \quad (2)$$

where  $J$  is a positive integer,  $1/Z_W$  is the curvature of the incident wave at G1,  $Z_J$  is the location of the self-image as measured from G1, and  $Z_T$  is the distance  $2d^2/\lambda$ . The self-image will be magnified by a factor

$$M = 1 + Z_J/Z_W. \quad (3)$$

This image, when superimposed with the second grating, again produces moiré fringes. Now the grating G2 is rotated around the optical axis until the grating bars of G1 and G2 are parallel to each other. In this case, the Rogers vector diagram gives a fringe spacing  $P = d_1 d_2 / |d_1 - d_2|$ , where  $d_1$  is the period of the self-image,  $d_2$  the period of the second grating, and  $d_1 = Md$ . The fringe spacing in terms of the grating period  $d$  is therefore  $P = Md/|M - 1|$ . Thus the fringe spacing is a quantitative measure of the degree of collimation, since  $|M - 1|$  is proportional to the curvature  $1/Z_W$ .

Now we want to discuss the accuracy obtainable, that is, the smallest detectable deviation from perfect collimation. If the collimation is perfect, the magnification  $M$  of the Talbot image is 1, and hence the moiré period  $P$  is infinite. Thus our task is to find how small the period  $P$  must become in order to be detectable. Experience has shown that the presence of a moiré effect is clearly visible if at least one-half of the moiré period  $P$  falls within the limited field of observation with width  $B$ . Thus one fringe will be detected whenever the number of lines between grating G2 and the image of G1 differ by one-half. With divergent illumination we count  $N$  lines of G2 in the observation field of width  $B$  and  $N - \frac{1}{2}$  lines of the image of G1. Thus the magnification  $M$  required for fringe detection is bounded by

$$M \geq N/(N - \frac{1}{2}) \approx 1 + 1/2N, \quad (4)$$

and in convergent illumination,

$$M \leq N/(N + \frac{1}{2}) \approx 1 - 1/2N. \quad (5)$$

By combining Eqs. (2) and (3) we have

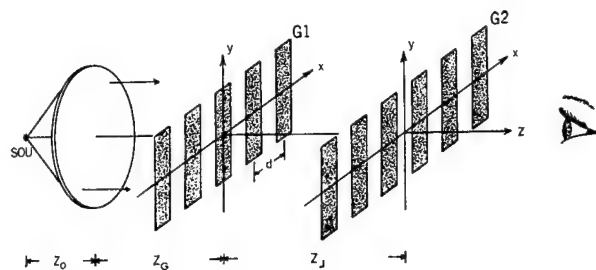


Fig. 1. Talbot interferometer setup for observing fringes due to defocusing of collimator objective ( $Z_0 \neq f$ ). Fringes are observed on G2.

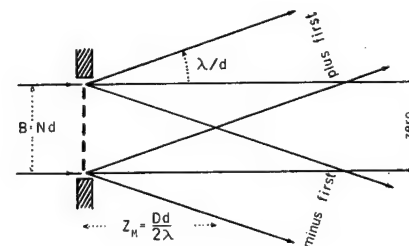


Fig. 2. The self-imaging effect occurs within overlapping orders. Test done at distance where the two first-order diffraction spots begin to separate.

$$M = (1 - 2JZ_T/Z_W)^{-1} \approx 1 + 2JZ_T/Z_W. \quad (6)$$

If  $M$  falls outside the bounds of Eqs. (4) and (5), no fringes will appear, limiting the sensitivity of this test. Solving Eq. (6) with the bounds of Eqs. (4) and (5), we find that the minimum detectable field curvature  $1/Z_W$  is  $|1/Z_W| \geq (4NJZ_T)^{-1}$ , where the absolute signs obviate the necessity of assigning a sign convention for field curvature. By substituting Eq. (2) into the above equation we obtain, for  $N \gg 1$ ,

$$|1/Z_W| \gtrsim (2NZ_J)^{-1}. \quad (7)$$

From Eq. (7) it follows that a large value of  $Z_J$  is desired in order to detect small collimation defects  $1/Z_W$ . The farthest distance to which we can go is limited by the walkoff of the first order grating diffraction. As indicated in Fig. 2, the longest distance at which there is still a connected interference field of width  $D$  is at  $Z_J = Dd/2\lambda$ . Perhaps one could perform collimation tests up to about twice this distance, but we will restrict ourselves to  $Z_J \leq Dd/2\lambda$ . Inserting this limit into Eq. (7), together with  $N = D/d$ , we get

$$|1/Z_W| \geq 2\lambda/D^2. \quad (8)$$

The curvature of the wave incident on G1 is related to the defocusing of the collimating objective by

$$|1/Z_W| = |f - Z_0|/(Z_0|f - Z_0| + Z_0f) \approx |f - Z_0|/Z_0f \quad (9)$$

where  $Z_0$  is the distance of the collimating objective from the point source,  $Z_G$  is the distance from objective to G1, and  $f$  is focal length of the objective lens. The approximation is permissible since the distance  $Z_G \ll Z_0f/|f - Z_0|$  in the test. Call  $\delta = |f - Z_0|$  the focusing error, and substitute Eq. (8) into Eq. (9). We have

$$\delta \geq 2\lambda(f/D)^2, \quad (10)$$



where we have used the fact  $Z_0 \approx f$ . Thus the focusing error is simply related to the wavelength, and the square of the focal length to beam diameter ratio.

The focusing error can be reduced by simply rotating one grating with respect to the other, thereby producing moiré fringes in the field of observation. In this fashion we change our detection scheme from the condition of uniform brightness to a system of rotating fringes. It is known that fringe detection is more accurate than use of the uniform brightness condition. We rotate both gratings in opposite directions by angles  $\theta/2$  with the  $y$  axis. If both gratings have the same period, moiré fringes will appear in the field of observation parallel to the  $x$  axis with spacings given by Eq. (1). When the periods are unequal, the fringe spacing is given by

$$P = d_1 d_2 / (d_1^2 + d_2^2 - 2d_1 d_2 \cos \theta)^{1/2} \approx d_1 d_2 / |d_1 - d_2|,$$

where the approximation is for small angular rotations of  $\theta$ , and  $d_1, d_2$  are the grating periods of G1 image and G2, respectively. It can be shown by using the vector arguments of Rogers that these fringes of unequal grating periods are rotated through an angle  $\phi$  with respect to the  $x$  axis, and the direction of this rotation depends on whether the illumination is converging or diverging. Thus the experimenter knows in which direction to move the objective lens. This rotation is related to the magnification  $M$  by  $M = (\cot \theta/2 + \tan \phi) / (\cot \theta/2 - \tan \phi)$ . Substituting this equation into Eq. (3) we obtain

$$1/Z_w = (1/Z_J)[2 \tan \phi / (\cot \theta/2 - \tan \phi)]. \quad (11)$$

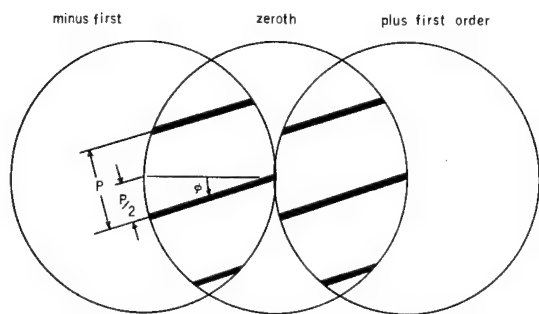


Fig. 3. Moiré fringes which are rotated through angle  $\phi$  because of defocusing of collimator objective.

Our ability to measure  $\phi$  limits the sensitivity of this test. If we say the minimum detectable fringe angle  $\phi$  is about one-half of a fringe (see Fig. 3), then Eq. (11) reduces to  $|1/Z_w| \geq 2\lambda/D^2$ .

This lower bound is identical to that of the uniform brightness condition [Eq. (8)]. In the laboratory one-quarter of a fringe was easily discernible, producing results which were a factor of 2 better than predicted. If we want to achieve even higher accuracy, we may use photodetectors instead of the eye. Assuming 1% brightness accuracy, we can detect fringes one hundred times larger than the field of view. Hence the photoelectrical approach would improve the detectability of collimation errors by a factor of about 50 over that which was predicted.

The visual experiments have confirmed our theoretical performance predictions. An objective lens of 20 cm focal length was used to produce a 5-cm beam. The light from a helium-neon laser was focused with a 3.9-mm focal length lens onto a 6- $\mu$  pinhole. The position accuracy was 0.001 cm, whereas the calculated accuracy was 0.002 cm. This improvement was due to the fact that one-quarter fringe was used with the angular measurement technique.

Last, one can improve the accuracy of the test by increasing the distance  $Z_J$ . This distance was limited by the walkoff as shown in Fig. 2. By the addition of one or two mirrors placed where the borderline rays of the zero-order diffraction propagate (Fig. 3), the diffracted first-order beam can be reflected back into the zero-order beam to create the shearing interferences. This should increase  $Z_J$  and the accuracy of the test manifold. However, this has not been verified experimentally.

The author is indebted to Adolf Lohmann for his support and interest in this work and for his helpful suggestions in the preparation of this Letter. This work was performed under Air Force contract AF-F19628-69-C-0268.

## References

1. M. V. R. K. Murty, *Appl. Opt.* **3**, 531 (1964).
2. P. Langenbeck, *Appl. Opt.* **9**, 2590 (1970).
3. A. W. Lohmann, in *Proceedings of the Conference on Optical Instruments and Techniques* (1961) (Chapman and Hall, London, 1962), 58; H. Klages, *J. Phys.* **28**, C2-40 (1967); A. W. Lohmann and D. E. Silva, *Opt. Commun.* **2**, 413 (1971).
4. Burch, *Progr. Opt.* **2**, 75 (1963).
5. G. L. Rogers, *Proc. Phys. Soc. (London)* **73**, 142 (1959).
6. J. M. Cowley and A. F. Moodie, *Proc. Phys. Soc.* **B70**, 486 (1957).

## Appendix 1

### Source Size

A point source will give self-images of the grating in a region where the diffracting orders interfere. As the size of the source increases, the distance over which self-imaging occurs decreases until images are no longer observed. The spatial coherence (size of the source) is derived with the aid of Figure 27.

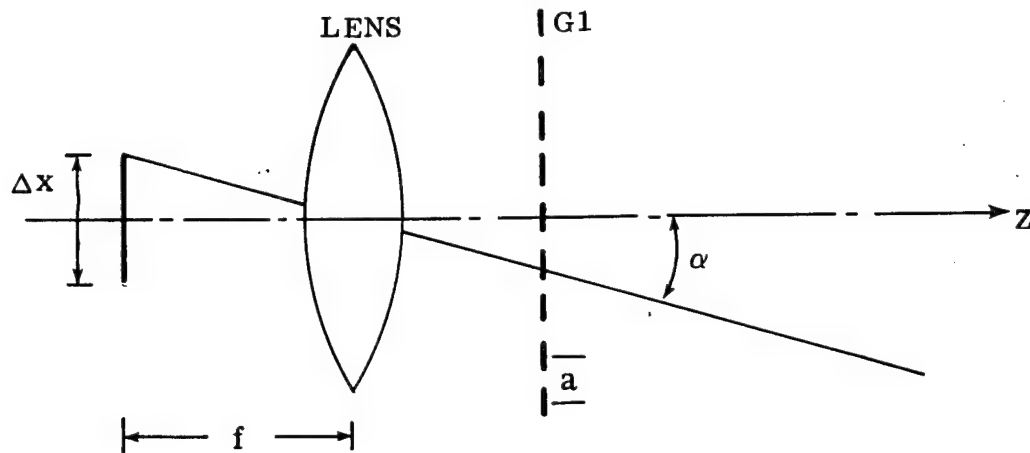


Figure 26. Diagram showing the angular size of the source. Source points off-axis produce shifted Talbot images. Summing the contributions from all points on the extended source yields a self-image of  $G1$  only if we do not allow the image to shift by more than say a quarter of a period,  $a$ .

An off-axis point source will produce self-images that are centered along the principal ray, that forms an angle  $\alpha$  with the optical axis, and at distances that are a multiple of  $2a^2/\lambda$ , where  $a$  is the grating period and  $\lambda$  is the wavelength of the light source. The shift  $s$  in the image is given by  $\alpha z$ . We have  $s = \alpha z = 2Ma^2/\lambda$ , where  $M$  is an integer. Each off-axis point in an extended source contributes a

shifted image to the observer. If the self-image of the grating is to be observed, the contributing image from the furthest off-axis point must not be shifted by more than a quarter of a period, i.e.  $s = 2\alpha Ma^2/\lambda < a/4$ , or  $\alpha < \lambda/8Ma$ .

The source size is related to  $\alpha$  by  $\alpha = \Delta x/2f$ , where  $\Delta x$  is the size of the source and  $f$  is the focal length of the collimating lens. Therefore for a self-image to occur at some multiple  $M$  of the self-image distance  $2a^2/\lambda$ , the size of the source must be limited by  $\Delta x < \lambda f/4Ma$ .

## Appendix 2

### Approximations Leading to the Second Derivative

Our expression for spatially filtered fringes contains a summation of derivatives that resulted from a Taylor series expansion. In this appendix we show that the lowest order term dominates the series, i.e.

$$\sum_{p=2}^{\infty} u_0^{(p)}(x,y) \Delta^p/p! \approx u_0^{(2)}(x,y) \Delta^2/2$$

if

$$|u_0^{(p)}(x,y)| \Delta^p/p! \leq \eta [u_0^{(2)}(x,y)]_{\max}$$

where  $u_0^{(p)}(x,y) = \partial^p u_0(x,y)/\partial x^p$ ,  $[u_0^{(2)}(x,y)]_{\max}$  is the maximum value that the function  $u_0^{(2)}(x,y)$  obtains,  $\Delta = z_2\lambda/d$  is the lateral shift and  $\eta$  is a factor which controls the degree to which the approximation is valid and is set to 1/10 for the remaining paragraphs. Rearranging this equation we get

$$[u_0^{(2)}(x,y)]_{\max} \geq |u_0^{(p)}(x,y)| \Delta^{p-2} 20/p!. \quad (1)$$

By the theorem of Bernstein, the derivatives of a bandlimited function  $u_0(x,y)$  are bounded by the maximum value that the function attains, i.e.

$$|u_0^{(p)}(x,y)| \leq (\pi\Delta\nu)^p [u_0(x,y)]_{\max},$$

where  $\Delta\nu$  is the bandwidth of the function  $u_0(x,y)$  in the Fourier domain and  $[u_0(x,y)]_{\max}$  is the maximum value of this function. This theorem implies that

$$|u_0^{(p)}(x,y)| \leq (\pi\Delta\nu)^{p-2} [u_0^{(2)}(x,y)]_{\max}$$

or

$$[u_0^{(2)}(x,y)]_{\max} \geq |u_0^{(p)}(x,y)| (\pi\Delta\nu)^{2-p}.$$

Eq. (1) is the condition for  $[u_0^{(2)}(x,y)]_{\max}$  under which our approximation for the second derivative is valid. This maximum is bounded by the lateral shift  $\Delta$  which is under the control of the experimenter. The bound of eq. (1) must be tighter (i.e. lower) than the above equation. Therefore  $\Delta^{p-2} 20/p! \leq (\pi\Delta\nu)^{2-p}$ , or  $\Delta \leq (p!/20)^{1/(p-2)} / \pi\Delta\nu$ .

The factorial dominates the root process as can be shown by using Stirling's approximation for factorial

$$(p!/20)^{\frac{1}{p-2}} \sim (\sqrt{2\pi}/20)^{\frac{1}{p-2}} (p/e) \text{ for large } p.$$

Therefore the smallest  $p$  ( $p = 4$ ) is the tightest bound for  $\Delta$ .

$$\Delta \leq (\sqrt{2\pi}/20) (4/e) / \pi\Delta\nu \approx \delta x / 6$$

where  $\delta x = 1/\Delta\nu$ . This equation states that the shear must be less than about one-sixth of the width of the object details in order that the second derivative dominate the Taylor series. This estimate is a worst case consideration. It is common practice in differential shearing

interferometry to use a shift of a half resolution unit  $\delta x/2$  instead of  $\delta x/6$  without noticeable detrimental effects. The reason for using somewhat larger shifts is improved detectability of soft slopes in the object.

### Appendix 3

#### Theoretical Consideration for First Order Filtering

By blocking one-half of our grating with an opaque screen our grating transmission function  $G(r)$  is modified as follows:

$$G(r) = \begin{cases} \sum_{(m)} C_m e^{2\pi i m r/a}, & 4a < r \leq A, \quad 0 < \varphi \leq \pi \\ 0 & \text{otherwise.} \end{cases}$$

This in turn necessitates a reappraisal of our theoretical calculations. Fortunately as we shall soon see our modified setup differs from the theory by only a multiplicative constant that accounts for the reduced intensity.

With our new limits the field beyond  $G_1$  is given by

$$u(r, \varphi, z) \sim \frac{1}{\lambda z^2} \int_0^\infty \int_0^\pi u(r', z_1^+) \exp\{i\pi[r^2 + r'^2 - 2rr' \cos(\varphi - \varphi')]/\lambda z\} r' dr' d\varphi',$$

where we recognize that

$$\int_0^\pi e^{-ix \cos \theta} d\theta = \frac{1}{2} \int_0^{2\pi} e^{-ix \cos \theta} d\theta.$$

Therefore the only difference in the computation of this equation from

that of the unblocked grating equation is the factor 2. Thus we copy the results obtained previously and divide by 2 to obtain

$$u(r, z) \sim \frac{1}{2} \sum_{(m)} C_m \sqrt{1 + (m\lambda z_1/ra)} e^{i\pi\lambda z_1 (m/a)^2} e^{2\pi i m r/a}.$$

The remaining integrations are the same, so that behind the final grating we have

$$u(r, \varphi, z_2^+) \sim \frac{1}{2} \sum_{(m)} \sum_{(n)} C_m C_n e^{i\pi m} e^{2\pi i (m+n)r/a} \sqrt{1 + mMa/r} u_0(r - m\lambda z_2/a, \varphi).$$

This result differs from our theoretical result for full circular gratings by only a constant factor. Thus blocking one-half of the circular grating only reduces the overall intensity while allowing us to separate out the first diffracted orders.

#### Appendix 4

##### Tolerances for Spatial Filtering a

##### Test Object with Multiple Focal Lengths

Consider a test object with focal lengths  $f_1$  and  $f_2$  corresponding to test object areas  $O_1$  and  $O_2$  respectively. The diameter of  $O_1$  is  $h_1$  and of  $O_2$  is  $h_2$ . The effective focal lengths are given by

$$f' = f_1 f_L / (f_1 + f_L - D), \quad f'' = f_2 f_L / (f_2 + f_L - D),$$

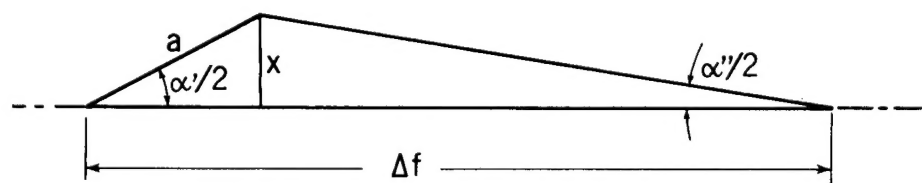
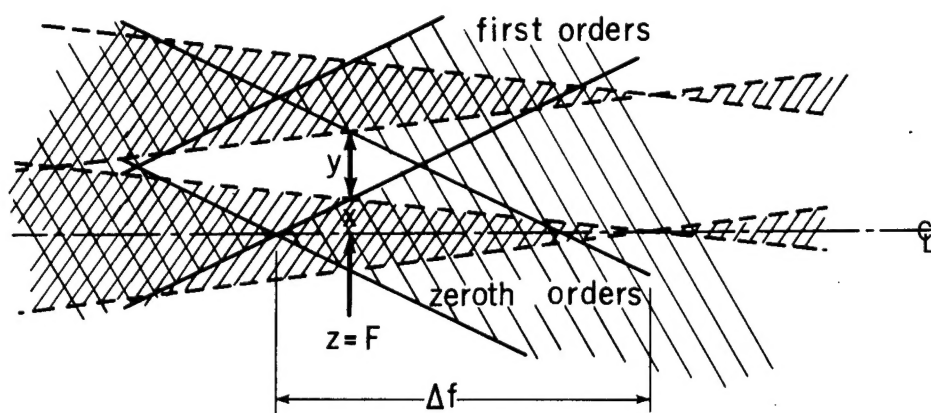
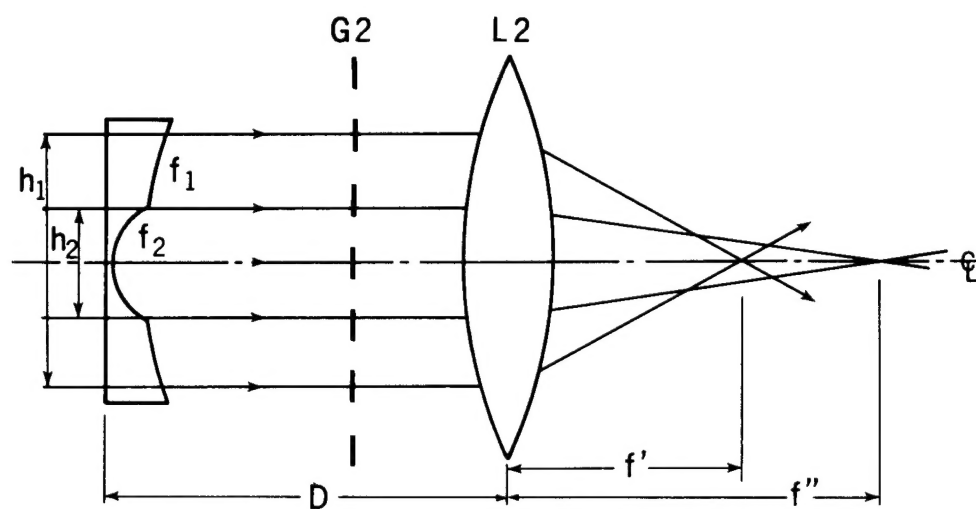
where  $f_L$  is the focal length of lens L2 and  $D$  is the distance that L2 is from the test object.

The diffracted orders therefore fall at distances  $f'$  and  $f''$  from

Figure 27(a). The tail end of the Talbot interferometric setup showing how a bifocal lens causes the zeroth diffracted order to meet in two different planes  $f'$  and  $f''$ .

Figure 27(b). An enlargement of the filtering region that lies between  $f'$  and  $f''$  in (a). The plane  $z = F$  is the optimum location for separating out either the zeroth or first diffracted orders.  $y + 2x$  is the distance between the zeroth and first orders.

Figure 27(c). An expansion of the triangular region in (b) which aids in the computation of  $x$ .





the principal plane of the combined system  $O$  and  $L_2$ . The angles at which the diffracted orders meet are  $\alpha'$  and  $\alpha''$ . These quantities are marked in Figure 27(a). An expanded view of the area in which the diffracted orders meet is drawn in Figure 27(b). We see that filtering can be accomplished in plane  $F$  as long as the diffracted orders do not overlap. This is equivalent to saying that the distance marked  $y$  must be greater than zero. In Figure 27(b) we have drawn the figure as though the first diffracted order for  $O_1$  lay at the same distance from the optical axis as  $O_2$  (i.e.,  $\lambda f'/a \approx \lambda f''/a$ ). This assumption is a conservative one, since the distance  $y$  is slightly larger if we do not make this assumption. To summarize, filtering is possible at plane  $z = F$  if  $y = (\lambda f'/a) - 2x > 0$ , or  $\lambda/a > 2x/f'$ .

The distance  $x$  is computed from a trigonometric consideration of the oblique triangle containing  $x$  and a side of length  $\Delta f$ . This triangle is enlarged in Figure 27(c). From the law of sines we have  $a/\Delta f = \sin(\alpha''/2)/\sin(\alpha'/2 + \alpha''/2)$ , and the right triangle gives us  $x = a \sin(\alpha'/2)$ , where  $\sin(\alpha'/2) \approx \tan(\alpha'/2) = h_1/2f'$  and  $\sin(\alpha''/2) \approx \tan(\alpha''/2) = h_2/2f''$ . Therefore  $x \approx \Delta f h_1 h_2 / 2(h_1 f'' + h_2 f')$ . Our bound on the diffraction angle is therefore  $\lambda/a > \Delta f h_1 h_2 / (f')^2 (h_1 + h_2)$ , where we have assumed that  $f' \approx f''$ . Some simplification will result if we let

$$\Delta f/f' \approx \frac{1}{f'} - \frac{1}{f''} = \frac{D - f_L}{f_L} \left( \frac{1}{f_2} - \frac{1}{f_1} \right) = \left( \frac{1}{f_2} - \frac{1}{f_1} \right) / M,$$

where  $M$  is the lateral magnification. Hence

$$\lambda/a > \left( \frac{1}{f_2} - \frac{1}{f_1} \right) / M \left( \frac{1}{h_1} + \frac{1}{h_2} \right)$$

and we conclude that the focal length of lens  $L_2$  is immaterial for these considerations.

Unclassified

Security Classification

DOCUMENT CONTROL DATA - R & D		
(Security classification of title, body of abstract and indexing annotation must be entered when the overall report is classified)		
1. ORIGINATING ACTIVITY (Corporate author)		2a. REPORT SECURITY CLASSIFICATION
University of California, San Diego Dept. of Applied Physics & Information Science La Jolla, California 92037		Unclassified
3. REPORT TITLE		2b. GROUP
THE MEASUREMENT OF SPATIAL AND TEMPORAL DISTRIBUTION OF RADIATION, USING A TALBOT SPECTROMETER		
4. DESCRIPTIVE NOTES (Type of report and inclusive dates)		
Scientific. Final. July 1, 1971-June 30, 1972 Approved 24 July 72		
5. AUTHOR(S) (First name, middle initial, last name)		
Adolf W. Lohmann Donald E. Silva		
6. REPORT DATE	7a. TOTAL NO. OF PAGES	7b. NO. OF REFS
June 30, 1972	109	74
8a. CONTRACT OR GRANT NO.		9a. ORIGINATOR'S REPORT NUMBER(S)
F 19628-69-C-0268 ARPA Order No.		
b. PROJECT, TASK, AND WORK UNIT NO.		
8692 n/a n/a 1366		
c. DOD ELEMENT		9b. OTHER REPORT NO(S) (Any other numbers that may be assigned this report)
62301D		AFCRL-72-0376
d. DOD SUBELEMENT n/a		
10. DISTRIBUTION STATEMENT		
A - Approved for public release; distribution unlimited.		
11. SUPPLEMENTARY NOTES		12. SPONSORING MILITARY ACTIVITY
This research was supported by the Defense Advanced Research Projects Agency		Air Force Cambridge Research Laboratories (OP) L.G. Hanscom Field Bedford, Massachusetts 01730
13. ABSTRACT		
<p>Our goal was to measure the distribution of radiation S as a function of its angular coordinates <math>\alpha</math>, <math>\beta</math> and its wavelength <math>\lambda</math>. We first measured <math>S(\alpha)</math>, i.e. the distribution of radiation as a function of one angular coordinate. From this we learned how critical the various parameters of our instrument, such as collimation and the gratings' substrate flatness, were to its successful operation. These investigations led to the design of new interferometric test instruments which include an autocollimator, and a lateral and radial shearing interferometer. Finally a theoretical study of an instrument to measure <math>S(\alpha, \beta, \lambda)</math> was accomplished.</p>		

DD FORM 1473  
1 NOV 65

Unclassified

Security Classification

Unclassified

Security Classification

14. KEY WORDS	LINK A		LINK B		LINK C	
	ROLE	WT	ROLE	WT	ROLE	WT
interferometer, circular grating, self-imaging, diffraction, spatial filtering, signal processing.						

Unclassified

Security Classification